ELECTROMAGNETIC ACOUSTIC RESONANCE AND NONCONTACTING MATERIALS CHARACTERIZATION

HIROTSUGU OGI

Graduate School of Engineering Science
Department of Systems and Human Science
Division of Mechanical Science
OSAKA UNIVERSITY

ACKNOWLEDGMENT

I am indebted to Professor M. Hirao, Graduate School of Engineering Science, Osaka University, for his guidance, encouragement, and many advises throughout this study. I would like to thank Professors T. Yoshikawa and K. Ogura, Graduate School of Engineering Science, Osaka University, for reviewing this thesis and gave me valuable comments. I owe special thanks to Dr. H. Fukuoka, President of Nara National College of Technology, for giving me a chance to begin this study and for his continuous encouragement to me. I wish to thank Dr. T. Yamasaki and Mr. K. Yaegawa for their encouragement and assistance throughout this study.

The establishment of the superheterodyne-EMAR system was supported by Mr. T. Miya, President of Sonix. K.K., Dr. G. L. Petersen, President of RITEC Inc., and Dr. C. M. Fourtunko, National Institute of Standards and Technology. The fabrication of the printing sheet coils of the EMATs was performed with the help of Mr. T. Ohtani, Ebara Research Co., LTD. I am pleased to let them know the finish of this thesis and to express my gratitude to them. I am also grateful to Professor H. Mori, Research Center for Ultra-High Voltage Electron Microscopy, Osaka University, who kindly helped me obtain the TEM images described in Chapter VII, to K. Sugino, Nippon Steel Corp., who gave me the JIS-60 rail samples used in Chapter IV, and to Professor Y. Ueda, Welding Research Institute of Osaka University, who kindly offered the use of a 300-ton capacity testing machine in Chapter IV. I should like to acknowledge my indebtedness to the courtesy of the Committee of Sensors for Microstructures, Iron and Steel Institute of Japan, for providing the steel samples used in Chapter VI.

Particular thanks go to Mr. T. Honda, Denso Corp., and Mr. K. Minoura, Toray Industry Inc., for their valuable assistance when they were the graduated students in Osaka University.

TABLE OF CONTENTS

CHAPTER I

INTRODUCTION

1.1 Necessity of noncontacting characterization of materials

Propagation behavior of ultrasonic waves in solids has been intensively investigated as a powerful tool for the nondestructive characterization (NDC) of materials. One of essential advantages of ultrasonics is the capability of proving inside of solid materials, making a contrast with other techniques like the optical methods, the X-ray diffraction, and the magnetic testing methods, which scan only the surface or near-surface region. At present, there are two main fields relying on the NDC techniques with ultrasonics.

First is the industry-oriented nondestructive evaluation for detecting cracks, stresses, and microstructural changes in structural solid materials. While our today's society depends on recent advances of technology, we also face the serious problem of aging infrastructures. Nondestructive assessment to estimate the deterioration degree and the remaining life is getting more and more important. The most urgent need is to detect the signals reflected by the flaws in the material and obtain the quantitative information for applying the fracture mechanics. Ultrasonics have already been used for this purpose; the practice is nowadays advancing from manual to automatic for the quick and signal-recorded inspection. Second target is the microstructure change due to thermal aging, fatigue, creep, irradiation of radial rays, corrosion and so on, which would finally lead to the macroscopic cracks. Required is the detection of some indicative precursors far before the final event and the continuous monitoring of their subsequent growth. This is equally important because those processes govern the remaining life and we should determines the replacement schedule of parts. For this, ultrasonics are expected as the NDC tool. Since a large amount of materials is used in a structure, the NDC method should be simple with minimum consumption of time and labor. Especially, the NDC for nuclear power plants needs remote controlling and should be performed with a noncontact sensing being free from coupling media and surface preparations.

The second field is physical acoustics to study solid physics in metals, composite materials, ceramics, and other solid materials. Ultrasonics can potentially provide the information in solids through either or a combination of the phase velocity, attenuation, the backscattering noise, and the nonlinear parameter. Among them, the phase velocity and attenuation have been studied theoretically and are well established as a useful

means of the NDC. A number of their potentials will be described in this thesis; this is a topics of review articles (Truel et al., 1969; Beyer and Letcher, 1969; Pao et al., 1984; Ritchie and Fantozzi, 1992; Levy, 1992). However, there has been a fundamental problem that the existing methods for sensing the velocity and attenuation cannot provide enough accuracy for the detection of a minute evidence in a material, which causes slight changes of the wave velocity and attenuation. One typical case is the velocity change, as small as 10^{-3} m/s, associated with the applied stress in a metal, which is known as the acoustoelastic effect described in Chapter IV. Another case is the attenuation evolution observed during a metal fatigue as will be discussed in Chapter VII.

Such a difficulty comes from the contact sensing. General procedure of ultrasonic measurements involves a coupling media between a transducer and a material being examined. In such a configuration, ultrasonics propagate not only in the sample material, but also in the coupling media and the transducer, causing the reflection and transmission at the boundaries between the transducer and the coupling material and between the coupling material and the sample. The transducer receives the back echo from the bottom surface of the sample as well as the disturbing echoes originating from the interferences. They often overlap each other and tend to degrade the accuracy of the velocity measurement, which should ideally be made with the back echo from the sample. The contact transduction poses much more serious problems in the attenuation measurement. Attenuation means energy losses, which arises when the ultrasonic propagates in a material. The energy losses due to propagation in the transducer and the coupling media are not negligible and often exceeds the attenuation in the sample. Furthermore, the exact measurement of attenuation requires the reflection and the transmission coefficients at the boundaries, which are unavailable in general because they are easily changed by the coupling pressure and the temperature, making it impossible to get the absolute value of attenuation.

1.2 Noncontacting ultrasonic spectroscopy: EMAR

The common key factor required in both fields to carry out high-grade NDC is a "noncontacting" measurement. This thesis is devoted to studying the noncontacting characterization (NCC) of materials by means of the *electromagnetic acoustic resonance* (EMAR). The EMAR is an ultrasonic spectroscopy, where an *electromagnetic acoustic transducer* (EMAT) is used as the transmitter and the receiver of elastic waves.

An EMAT functions for the energy transduction between the electromagnetic fields and the elastic wave in a conductive material, being free from any mechanical coupling means. Therefore, it has been expected to overcome the measurement difficulties associated with the contact transduction, because EMATs cause no interference

on the elastic wave reflection at the surface. Transduction without mechanical coupling allows noncontact operations at elevated temperatures, on moving objects, and in remote locations. Equally important advantage is that there are wave modes only excited with the specially designed EMAT, like the axial shear wave (Johnson et al., 1994; Ogi et al., 1997). But, besides the positive aspects, the weak coupling efficiency with an EMAT have deteriorated its usefulness for many applications.

Spectrometric approach using the ultrasonic resonances has been an established methodology to study a variety of physical phenomena through the resonant frequency and the sharpness of the spectrum (Q^{-1} value). A continuous wave or long rf burst wave is introduced in a sample material and then the frequency is swept to find resonant frequencies, which depends on the elastic properties, the wave mode, and the sample geometry. At a resonance, all echoes coherently overlap each other and make an antinode of the resonance around the probing region, producing a much larger amplitude than that would be caused by a single echo, and then leading to a larger signal-to-noise ratio. This is an advantage in the resonant technique. The contacting measurement continues to pose a problem in this method, too. The ultrasonic wave penetrates in the three components of the sample material, the coupling material, and the transducer, causing the multiple resonant mode involving the three components. This shifts the resonant frequency from that only in the sample and a tedious correction scheme, even though far from being perfect, is required (Mozurkewich, 1989; Hirao et al., 1992).

The combination of an EMAT and the ultrasonic resonance successfully overcomes the disadvantage of an EMAT with the advantage of the resonant method, and vice versa. The weak coupling efficiency of an EMAT is no more a problem by acquiring heavily and coherently overlapping signals at a resonant state. And, at the same time, the couplant free measurement with the EMAT completely avoids the occurrence of the multiple resonant mode. A powerful tool for the NCC of materials has originated from this combination, that is called EMAR.

1.3 Historical sketch of EMAR

The idea of using an EMAT for the ultrasonic resonant method is not new. Filimonov et al. (1971) and Nikiforenko et al. (1971) presented first the technique to measure the ultrasonic velocity in thin metal sheets. They detected the shear wave resonant spectrum. But, considering that no following-up paper has been published for twenty years since then, their work didn't seem to gain much attention for a further development, until Kawashima (1990) applied this technique to detect the rolling texture and evaluate the formability (or *r*-value) in thin steel sheets. His work became a turning point for developing a new research area of the EMAR (Johnson et al., 1992 and 1994; Clark et al., 1992; Fukuoka et al., 1993). The EMAR is presently in its third generation after the Russian researchers' (first generation) and Kawashima's (second generation).

With the recent advances of the electronics and signal processing, the EMAR has showed great potentials for the velocity and attenuation measurements and is currently developing for many industrial and scientific-oriented measurements. The difficulty of a precise velocity measurement is overcomed by incorporating high sensitive EMATs and employing the superheterodyne processing for the receiving signal (Hirao et al., 1993a and 1993b). Furthermore, it is found that the EMAR gives an absolute value of attenuation supported by the noncontacting nature and the weak coupling efficiency of an EMAT (Ogi et al., 1995a and 1995b). This is one of the novel aspect of the EMAR, because the absolute measurement of attenuation was a dream in this community and was never carried out with other techniques due to excess energy losses associated with the contact transduction. Even using an EMAT in a pulse-echo method, the signal is too weak for the attention to be determined satisfactorily.

1.4 Outline of contents

My original contributions to the EMAR method for the NCC of metals are (i) the incorporation of EMATs in the superheterodyne signal processing system, (ii) the model analysis to clarify the transduction mechanism in ferromagnetic metals, (iii) the realization of highly accurate measurements of the phase velocity and attenuation, and (iv) their applications to acoustoelastic stress measurements, grain size determination of polycrystalline metals, and the detection of the fatigue damage evolution.

Chapter II summarizes the basic principle and the instrumentation of the EMAR. Typical bulk-wave EMATs and the acoustic resonance provide the general feature and the usefulness of the EMAR. The high-power gated amplifier and the analog-superheterodyne signal processing system are established to acquire high signal-to-noise ratio and shorten the measuring time. An EMAT driven with gated coherent bursts receives heavily overlapping echoes, which are fed to the super-heterodyne system, resulting in the amplitude spectrum. The Lorentzian function is fitted to the amplitude-frequency data around the spectrum peak, whose center axis gives the resonant frequency with an extremely high reproducibility.

For the optimum EMAT designing, it is necessary to understand the coupling mechanism of the EMAT phenomena. This has been a long running topic in the areas of the ultrasonics and electromagnetic physics and still has not been solved thoroughly. Chapter III addresses the investigation on the coupling mechanism between the electromagnetic fields and the bulk waves (longitudinal and shear elastic waves). The field dependence of the bulk-wave amplitudes is measured from the peak height of the EMAR spectrum. A two-dimensional model is employed to explain the observed results, including the three mechanisms taking part in the transduction; the Lorentz force mechanism, the magnetization mechanism, and the magnetostrictive mechanism. The model analysis and the measurement lead to the conclusion that the magnetostric-

tive mechanism is the dominant source, especially of the shear wave, in a ferromagnetic metal. The unsolved behavior of an EMAT that the coupling efficiency of the logitudinal wave is much smaller in ferromagnetic metals has been well explained by the present model.

Taking full advantage of the contactless spectroscopy method, two basic aspects of EMAR are used for practical applications. One is the amplitude spectrum, which gives the information on elastic wave speed through the resonant frequency. Typical NDC using the wave velocity is the determination of the second-order elastic constants or the sample dimensions, where the required accuracy is in the order of 1 m/s at most. The nonlinear elastic theory with the third-order elastic constants explained the acoustoelastic effect, which describes a linear dependence of the wave velocity on the stress in a material (Pao et al., 1984). This made it possible to evaluate the interior stress with ultrasonics, but a high accuracy is required because the velocity change due to the stress is fairly small ($\sim 10^{-3}$ m/s·MPa^{-1} for steels, for example). The use of the superheterodyne signal processing in the EMAR establishes the accurate measurement of the resonant frequency in the fraction of 10Hz order, which is enough for the stress measurement based on the acoustoelastic effect. Chapter IV presents four cases of practical application of the stress measurement.

The other aspect is the relaxation time reducible from the received ringdown signal at a resonance, whose importance has not been recognized in the acoustic field to date. In Chapter V, it is proved that the time coefficient of the resonant relaxation consists of attenuation in the sample and the diffraction loss which is attributed to the beam spreading of the ultrasonic wave. Couplant free transduction with the EMAT eliminates other extra energy losses due to the contact transduction. Only the diffraction loss, therefore, have to be corrected for to get the absolute value. A numerical iteration scheme is presented to remove the diffraction loss, resulting in the absolute attenuation.

Attenuation in a material is caused by the scattering from objects having different elastic properties from the surrounding matrix, and by the absorption which eventually transforms the elastic wave energy to the thermal energy. Grains in a polycrystalline metal can be the scattering sources (Bahatia, 1959), and a typical source of absorption is the dislocation vibration in room temperature and at the megaheltz frequency range (Granato and Lücke, 1956; Seeger, 1956). Chapters VI and VII are the typical applications of the NCC on the basis of the attenuation measurement.

Chapter VI addresses the scattering effect for estimating grain sizes in steels. The fourth power term of the frequency dependence of attenuation involves the pertinent information of the grain size. With a reference specimen whose average grain size is known, the grain sizes are calculated, which agree with those obtained from the micrographs on the exposed cross section in the band of 6μm.

In Chapter VII, a new EMAT configuration is presented to generate and receive

the axial shear resonance, which is capable of detecting the material inhomogeneity in the radial direction in a cylindrical pipe or rod sample. The EMAT is set to monitor the velocity and attenuation of the axial shear wave throughout the rotating fatigue life of steel pipe exposed to the bending stress. The evolution of attenuation and the velocity shift are interpreted through the absorption due to the dislocation damping with the help of observations of microstructures. An attenuation peak which always appears at 80-90 percent of the whole life is explained by the reformulation of the dislocations to the cell structure.

Chapter VIII presents summary and conclusion in this thesis, the remaining problems in the EMAR technique, and the future work to be examined.

CHAPTER II

PRINCIPLE OF ELECTROMAGNETIC ACOUSTIC RESONANCE

2.1 Introduction

An electromagnetic acoustic transducer (EMAT) (Gaerttner et al., 1969; Moran and Panos, 1976; Thompson, 1990; Maxfield and Fortunko, 1983; Kawashima, 1985) has been known as a noncontact ultrasonic transducer for a long time, and also it has been well recognized that the coupling efficiency is considerably smaller than that of the conventional piezoelectric transducers. This shortcoming didn't allow EMATs to replace the conventional piezoelectric transducers in spite of the great advantages of the noncontact probing.

Spectroscopic approach using the ultrasonic resonant technique has been used to investigate a variety of physical phenomena, especially in small samples. The highly and coherently overlapping echoes produce much larger receiving signal than the pulse-echo technique. Bolef and Millers (1971) surveyed the continuous-wave (cw) and pulsed-cw techniques. In this method, however, intimate contact between the specimen and the transducer(s) continues to pose a problem of separating the specimen's response from the as-measured spectra of the composite resonator. To reduce the influence, noncontacting or weakly coupling transducers are recommended. Hsieh and Khuri-Yakub (1993) used the one-point contact technique by replacing the receiving transducer with an optical interferometer and measured the elastic wave speeds in 1-mm-diam ceramic ball. Ledbetter et al. (1995) minimized this influence by simply applying the two point contacts of the piezoelectric transducers at the specimen's diagonally opposite corners.

The EMATs have the advantage of noncontact coupling and the disadvantage of weak coupling efficiency. The ultrasonic resonant technique has the advantage of involving a large number of coherent echoes, but it has the problem associated with the contact coupling. They have been the established methods by themselves, but used in limited applications. The combination of them successfully overcomes the disadvantage of the EMAT with advantage of resonance method and vice versa, presenting a new method of the noncontacting characterization (NCC) of conducting materials. This is the *electromagnetic acoustic resonance* (EMAR), in which the coupling efficiency of the EMAT is well enhanced by getting a large number of signals at a resonant state, and the noncontacting aspect of the EMAT completely avoids the mechanical cou-

pling between the transducer and the sample.

This Chapter introduces a general configuration of the EMAR by taking the case of the bulk-wave EMAT and the ultrasonic resonance in a plate. Comparison with the conventional contacting method illustrates the usefulness of the EMAR as a NCC tool. The high-power gated amplifier and the analog-superheterodyne phase detecting system are used throughout this research. The signal flow in the EMAT-superheterodyne system is explained for the thickness resonant case.

2.2 EMATs

An EMAT consists of the permanent magnets (or the electromagnet) to serve the bias field in a measuring object, and the coil elements to induce the dynamic field and the eddy currents in the surface region. Their configurations depend on the wave mode to be generated. Three body forces are considered to contribute to the transduction, that is, the Lorentz force, the magnetization force, and the magnetostrictive force (Wilbrand, 1987; Thompson, 1990). The Lorentz force exists in all metals, but the later two appear only in ferromagnetic metals. Their detail analysis will be discussed in Chapter III. In the present Chapter, two typical EMATs for bulk waves are introduced.

Figure 2.1(a) presents an appearance of the bulk-wave EMAT and a sketch of the operation in a nonmagnetic metal. The bulk-wave EMAT has a pair of permanent magnets, which have the opposite magnetization directions normal to the sample surfaces, and a flat elongated spiral coil. When the coil is placed near the metal surface and is driven by an rf current, eddy currents are induced in the near surface region. These currents interact with the static magnetic field applied by the magnets and generate the Lorentz forces upon electrons carrying the eddy currents. Through the collision with ions and other transformation mechanisms (Quinn, 1967; Dobbs, 1976), the Lorentz forces are transmitted to the lattice. Previous work (Gaerttner et al., 1969; Thompson, 1973) found that the Lorentz force can be treated as a direct body force in the solid and acts as a sources for ultrasonic vibration. It is important to note that the source originates in the metal, not in the transducer, and therefore no transmission is needed. For this EMAT, the vertical component to the surface of the static field is large in the region under the coil element, where the Lorentz force operates parallel to the surface (f_y) and results in the polarized shear wave propagating in the thickness direction. Under the center and edge portions of the coil elements, the horizontal component of the static field is large so that it generates the vertical Lorentz force for launching the longitudinal wave.

Figure 2.1(b) shows an appearance and the operation of the dual-mode EMAT, which consists of a cylindrical permanent magnet and a spiral flat coil. The static field from the magnet has the radial and the normal components, which interact with the eddy currents and induce the Lorentz forces along the normal and radial directions,

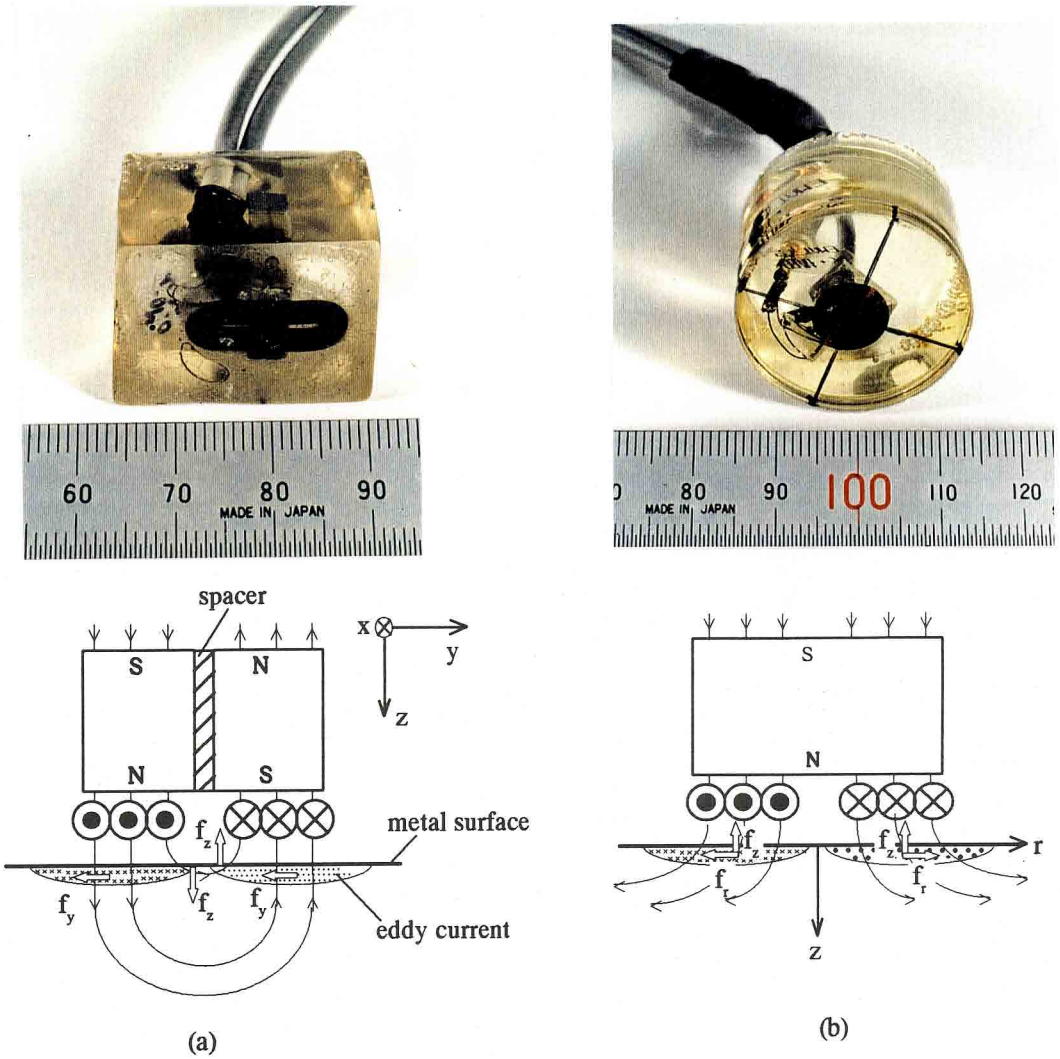

Figure 2.1 Photographs and schematic of (a) a bulk-wave EMAT and (b) a dual-mode EMAT, showing the Lorentz force mechanism in a nonmagnetic metal.

respectively (f_z and f_r). These forces generate the longitudinal wave and the radially-polarized shear wave propagating in the thickness direction at the same time. If the metal has an orthorhombic anisotropy due to the rolling texture, the shear wave polarization separates into the two principal directions, producing the split resonant spectrum observed by Nikiforenko et al. (1971).

2.3 Ultrasonic resonance

Consider the measuring situation that a transducer is located on the surface of a plate of thickness d and excites an ultrasonic wave of only one cycle propagating in the thickness direction, whose wavelength and period are λ and T, respectively. The pulse wave is subjected to the repeated reflections at both free surfaces and is received by the

same transducer every time when it reaches the incident surface. In the case that $\lambda << d$, the received signals will be observed as shown in Fig.2.2(a). The horizontal axis in Fig.2.2 expresses the time measured just after the excitation, and the vertical axis is the wave amplitude; T_0 is the round-trip time through the thickness. The amplitude decreases as the propagation path increases and eventually vanishes, depending on attenuation in the material.

Next, suppose the use of the rf burst signal composed of five cycles instead of a single-cycle pulse. In this case, before the first back echo is completely received, the second echo reaches the incident surface; the end of the first echo and the head of the second echo are superimposed each other, causing the interference between them. The same occurs between the second and third echoes, the third and fourth echoes, and so on. The signal amplitudes are canceled or enhanced in the overlapping area, depending on the phase difference due to the difference of propagation pathes. In Figs. 2.2(b) and (c), the destructive and constructive interferences are illustrated.

Then, suppose changing the wavelength by changing frequency. Sweeping the carrier frequency of the input burst, all the echoes are overlapped in a phase with a simply added amplitude only when the round-trip time T_0 is an integer multiple of the period T:

$$T_0 = nT , \tag{2.1}$$

where n is an integer, giving the number of cycle in T_0. Figure 2.2 (c) shows the case of n=3. By expanding the five-cycle pulse to more than several hundred cycles, the first echo overlaps almost all other echoes coherently, and much larger signal amplitude are observed. This is the state of the ultrasonic resonance. It is easily found from Eq.(2.1) that the resonance occurs at every frequency satisfying

$$f_n = nc/(2d) , \tag{2.2}$$

where c is the phase velocity and f_n is the nth resonant frequency. The measurement of a resonant frequency therefore gives the velocity or the thickness, when either is known.

The example presented above pertains to the thickness resonant case. There are many ultrasonic resonances depending on the sample geometry and the wave mode, but their basic principle is the same as the thickness resonant case.

At a resonance, a large number of receiving signals are overlapped coherently, making the signal-to-noise ratio much higher than that produced by the single echo. However, the resonant method with a usual contacting transducer brings a serious problem: Figure 2.3 illustrates the general feature of the thickness resonance of n=1 caused by a contacting transducer and an EMAT. When the contacting transducer is in use, the ultrasonic wave propagates not only in the sample but also in the coupling material and the transducer itself. This leads to the composite resonant mode encom-

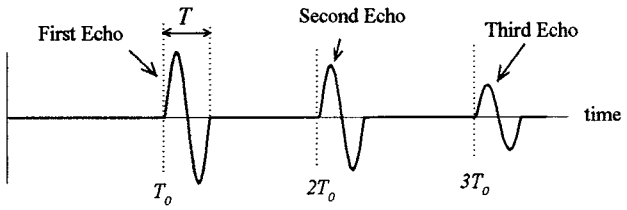

(a)

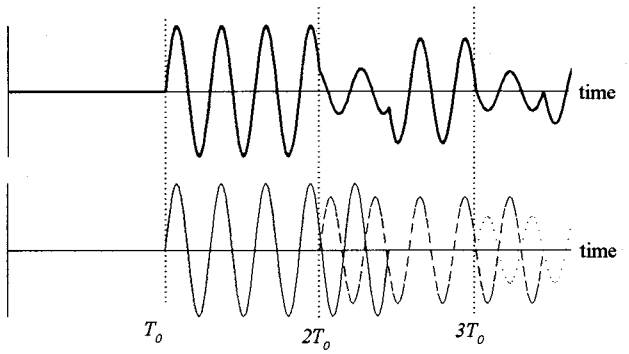

(b)

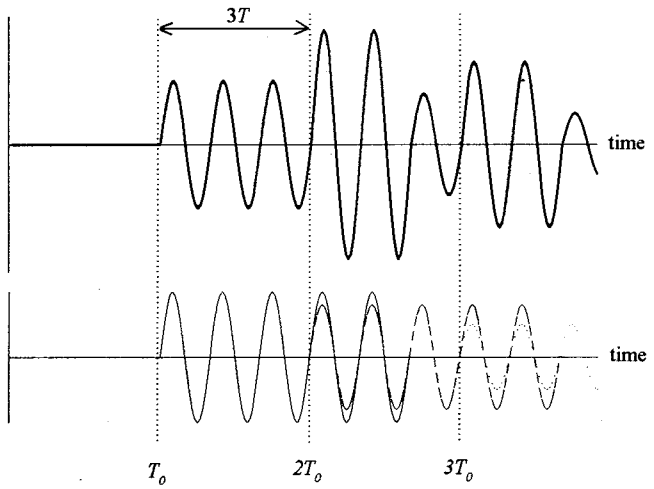

(c)

Figure 2.2 Explanation of the ultrasonic resonance in a plate. (a) Multiple echoes of single cycle, (b) destructive interference of echoes, and (c) constructive interference.

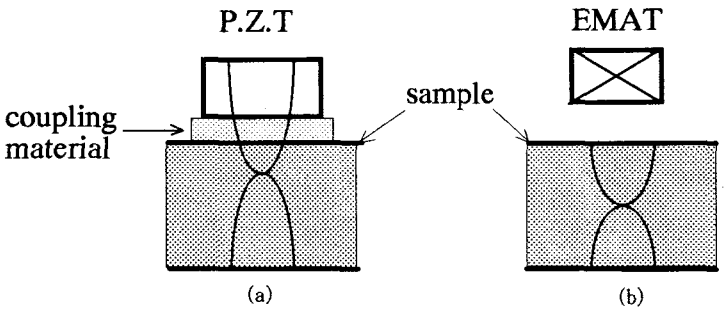

Figure 2.3 (a) Composite resonance with a contacting transducer and (b) isolated resonance using an EMAT (n=1).

passing the sample, the coupling material, and the transducer, and modified the resonant frequency from that determined by Eq.(2.2). The correction for the influence for an accurate resonant frequency is not straightforward because it needs the velocity and the density in all components which are unavailable in practice (Mozurkewich, 1989; Hirao et al., 1992). Especially, those of the coupling material highly depends on the coupling pressure and the temperature. The contacting method presents more troublesome difficulty for the attenuation measurement. The transducer and coupling material absorbs a large amount of energy from the ultrasonic vibration. Attenuation, which is small energy loss within the sample, brings the important information about the sample material, but it is often hidden by the large extra losses and could not be determined in a necessary precision. The EMAT, however, needs no coupling material and is free from such problems. The weak coupling of the EMAT takes little energy of the wave, making possible to measure the small amount of energy loss in the sample. Low transduction efficiency of EMATs has been considered to be a disadvantage. But, by changing the viewpoint, it brings a large benefit of isolating the sample's ultrasonic resonance from the transducer, leading to the absolute measurements of phase velocity and attenuation. The EMAT and the resonant technique is thus a good combination for the NCC of metals.

2.4 Spectroscopy with superheterodyne phase detection

The mechanical spectroscopy is an established methodology for determining the elastic wave velocity in small samples (McSkimin, 1964). The velocities are extracted using the maximum or minimum amplitude in frequency-domain response, and the sample geometry. The instrumentation presented here has developed by Petersen et al. (1993a, 1993b and 1994) originally for the nuclear magnetic resonance (NMR) applications. For the first time, this instrumentation is incorporated with the EMATs to

realize the EMAR technique (Hirao et al., 1993b). It is based on the sampled-cw technique introduced by Bolef and Miller (1971), but includes some latest advances in electronics and signal processing. The signal processing scheme of the spectrometer uses the superheterodyne techniques not only in the receiver section but also for producing the source signal of the driving signal. A high-power gated rf amplifier to drive the EMATs, quadrature phase-sensitive detectors, and gated analog integrators contribute to the improvement of the absolute accuracy with the EMAR measurements. The idea of using the analog integrator has been reported previously by Clark (1964) and is known as the Clark method. He extracted one frequency component at a time from the free-induction decay in NMR absorption while sweeping the magnetic field. Avogadro et al. (1979) has applied the Clark method to the study of NMR spectra in solids and showed that the method was particularly suitable even when some complications arise with very broad spectra. Recently, the analog spectroscopic methods such as the Clark method have been largely replaced by digital methods in the study of NMR, which use the fast Fourier transform (FFT) algorithm. The digital FFT signal processing, however, requires the shorter driving pulse or rf bursts, limiting the amount of energy. In the ultrasonic resonance, we need longer rf bursts to excite ultrasonic resonance, which forces us to employ the analog spectroscopic technique.

Figure 2.4 shows an appearance of the EMAT-superheterodyne spectroscopic system, and its simplified block diagram. The thickness resonance in a plate sample is again considered here as an illustrative example.

There are four multipliers in the detector which is numbered from No.1 to No.4, playing the central role in the heterodyne processing. The cw driving signal of frequency ω_F is produced by multiplying the signals from the synthesizer and the intermediate frequency (IF) oscillator. The former offers the signal with the frequency $(\omega_F+\omega_{IF})$, and the latter gives the signal with the frequency ω_{IF}, where ω_{IF} is a constant frequency of 25MHz. These signals are expressed by $A_S\cos[(\omega_F+\omega_{IF})t+\theta_S]$ and $A_{IF}\cos(\omega_{IF}t+\theta_{IF})$, respectively; A is the amplitude of the signal and θ is its arbitrary phase. The subscripts S and IF denote the quantities of the synthesizer and the IF oscillator. Multiplier No.1 produces the difference and sum of their frequencies:

$$A_S\cos[(\omega_F+\omega_{IF})t+\theta_S]\cdot A_{IF}\cos(\omega_{IF}t+\theta_{IF})= A_SA_{IF}\{\cos(\omega_Ft+\theta_S-\theta_{IF})+\cos[(\omega_F+2\omega_{IF})t+\theta_S+\theta_{IF}]\}/2 \quad . \qquad (2.3)$$

The sum frequency term, $(\omega_F+2\omega_{IF})$, is first removed by a low pass filter located at the output of the multiplier. The difference frequency term of ω_F is used to produce the high-power rf bursts through the gated amplifier, which is applied to drive the EMAT.

The EMAT excites the ultrasonic wave traveling in the thickness direction. Just after the excitation, the same EMAT detects the highly overlapping echoes. Each echo has the amplitude depending on attenuation in the sample, and the phase of $(\omega_Ft+\theta_S-\theta_{IF}+\phi_i)$, where i is the echo number and ϕ_i is its phase shift relative to the driving signal;

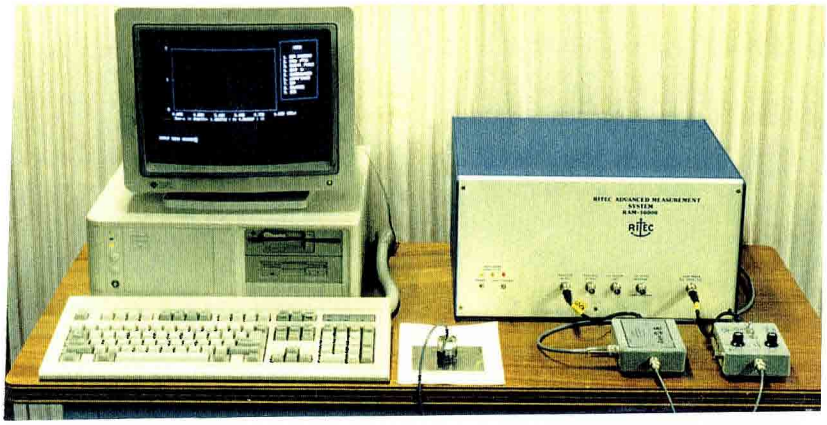

(a)

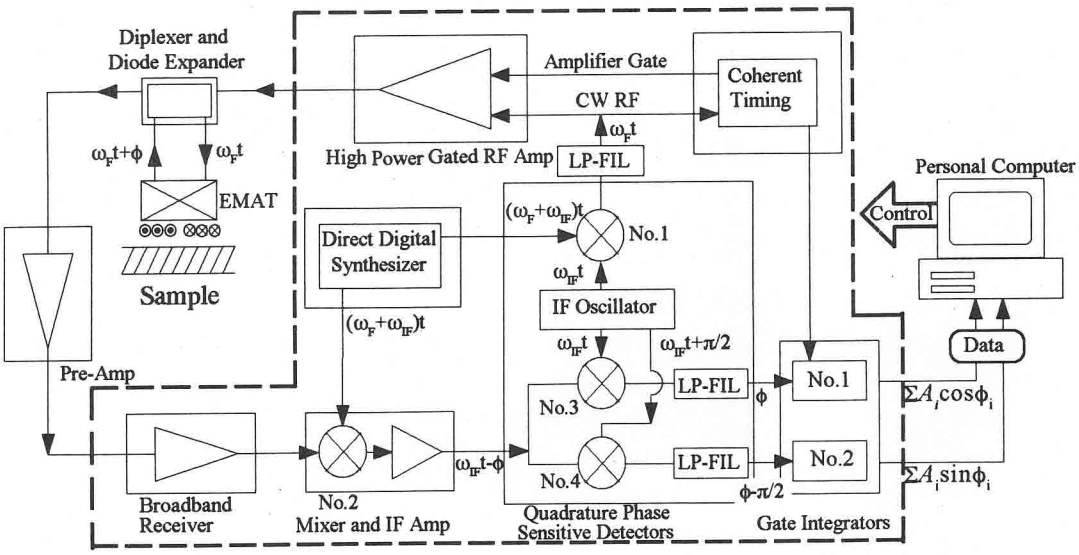

(b)

Figure 2.4 (a) Photograph of the EMAR system and (b) blockdiagram for detection of amplitude spectrum and attenuation coefficient by superheterodyne receiver. The diagram includes phases at each step. A_i is the amplitude of the ith reflected echo and ϕ_i its phase.

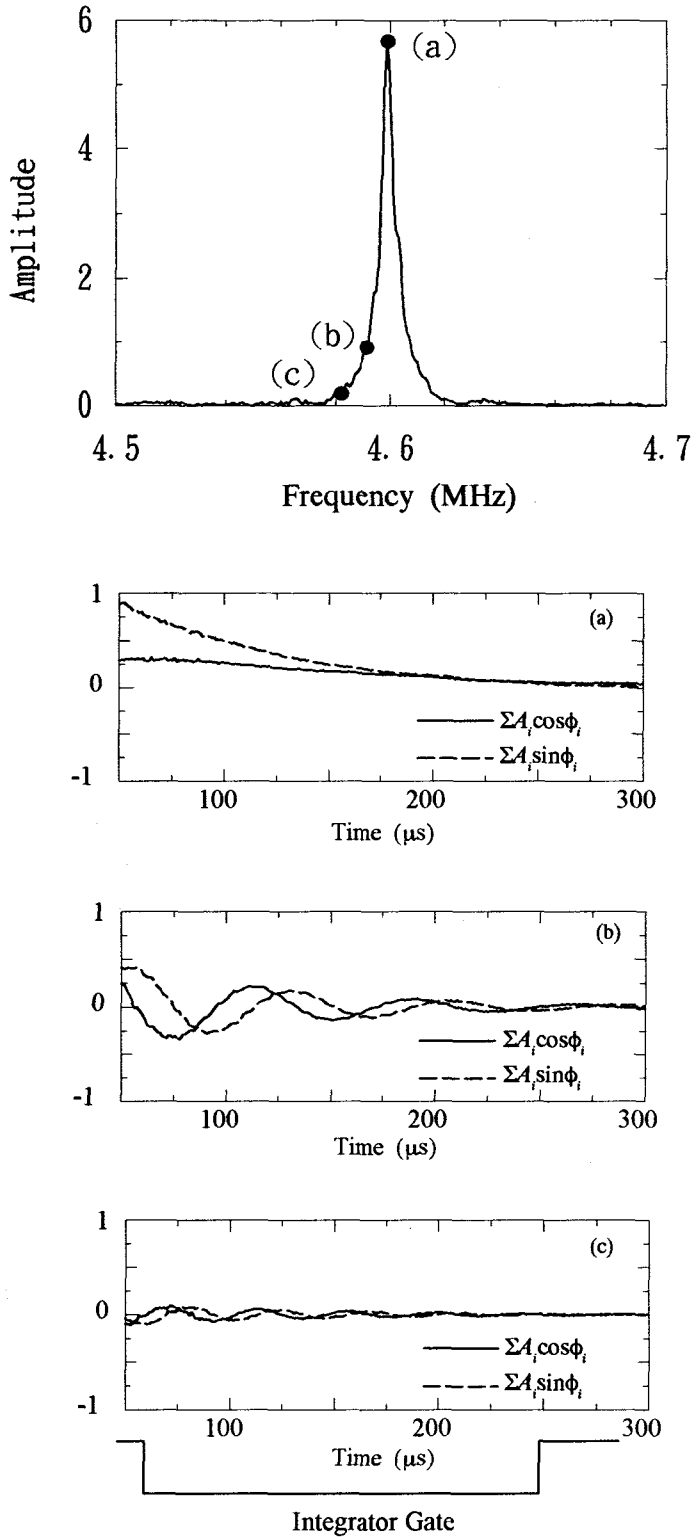

Figure 2.5 In-phase and out-of-phase outputs just before integration at (a) a resonant frequency, (b) an off-resonant frequency, and (c) a frequency far from the resonance.

$$\phi_i=\omega_F d(i\text{-}1)/c, \quad i=1,2,3,\ldots \quad . \tag{2.4}$$

The signals are amplified by the high-impedance preamplifier to 40dB and fed to multiplier No.2 after being received by the broadband receiver: The signal from the synthesizer is also sent to the multiplier No.2, and then the difference frequency terms are extracted by the IF-amplifier, which completely removes the higher frequency terms involving the frequencies of $(\omega_{IF}+2\omega_F)$. The remaining signal, containing the phase of $(\omega_{IF}+\theta_{IF}-\phi_i)$, is amplified and put in multipliers No.3 and No.4. In-phase and out-of-phase signals of the IF-oscillator are also fed to the multipliers No.3 and No.4, respectively. After multiplying, the high frequency terms are again rejected through the low-pass filters, and the remaining signals $\sum_i A_i \cos\phi_i$ and $\sum_i A_i \sin\phi_i$ are obtained. Both A_i and ϕ_i are functions of time. These outputs are integrated by analog gated integrators just after the end of the rf bursts until no more ringing is observed, and their outputs are stored in the personal computer. Single measurement at a frequency takes ~0.01 sec.

The *amplitude spectrum* as a function of the operating frequency ω_F is defined by the root of the sum of the squares of the integrator outputs. By sweeping the operating frequency and getting the amplitude spectrum at each frequency, the resonant spectrum is obtained as shown in Fig.2.5. In the figure, in-phase and out-of-phase outputs before the integration are also shown at three different frequencies. When the frequency is equal to the nth resonant frequency, ϕ_i becomes $n(i\text{-}1)\pi$; and $\cos\phi_i$ takes 1 or -1 and $\sin\phi_i$ takes 0, regardless of i. The output before the integrator, therefore, decays monotonously with time depending on the attenuation in the sample, and the amplitude spectrum becomes a large value (Fig.2.5 (a)). For the slightly off-resonant frequency, the signals ring down with still a large amplitude, but ϕ_i changes monotonically and the beats appear in the outputs of multiplier No.3 and No.4. Their integrated values are not large because the outputs take both positive and negative values along the time axis, which cancel each other within the integrator gates (Fig.2.5 (b)). For the frequencies far away from a resonance, the amplitude decays soon because of destructive interference among reflections (Fig.2.5 (c)). Two mechanisms, the cancellation within the integrator gate and the interference among overlapping echoes, work to realize a sharp resonant lineshape.

2.5 Determination of resonant frequency

Considering the case that the rf bursts of a length T_B drives an EMAT, which impinges the bulk wave into a plate of thickness d, the highly overlapping echoes E(t) is received at the incident surface and expressed by (Bolef and Miller, 1971)

$$E(t) = A_1 e^{j\omega t} \sum_i \left[H(t - iT_0) e^{-(i-1)(\alpha T_0 + j2kd)} \right], \quad i=1,2,3,\ldots \quad , \tag{2.5}$$

where j is $\sqrt{-1}$, A_1 is the amplitude of the first arriving echo, α the attenuation coefficient to time, and k the wave number expressed by $k=\omega/c$ with the angular frequency ω. H(t) is a function defined by

$$H(t) = \begin{cases} 0 & , \ t \le 0 \ \text{ or } \ t \ge T_B \\ 1 & , \ 0 < t < T_B \end{cases} . \tag{2.6}$$

When the rf burst is long enough, that is $T_B >> T_0$, the situation is approximated as a continuous wave case. Under the case, the factors $H(t-iT_0)$ are all simultaneously equal to unity, so that Eq.(2.5) reduces to

$$E(t) = \frac{A_1 e^{j\omega t}}{1 - e^{-(\alpha T_0 + j2kd)}} . \tag{2.7}$$

$|E(t)|$ is periodic in ω and has peaks at the frequencies which satisfy Eq.(2.2). By noting around one of the peaks, for example, the peak at $\omega=2\pi/T_0$, that is $kd \sim \pi$, and assuming a very low attenuation material ($\alpha T_0 << 1$), $|E(t)|$ is simplified using the Taylor series about $kd=\pi$ and $\alpha T_0=0$. The resultant expression becomes

$$|E(t)|^2 \sim \frac{A_1}{T_0^2} \cdot \frac{1}{\left(\alpha^2 + (\omega - 2\pi/T_0)^2\right)} , \tag{2.8}$$

which is familiar as the Lorentzian function. It is, therefore, effective to have a resonant frequency by fitting the Lorentzian function to the measured spectrum data around a peak and calculating its center axis.

2.6 Conclusion

In the EMAR method presented here, the personal computer controls all measurement setup, including the frequency range and sweeping rate, gain of the high power-amplifier and receiver, portion of the integrator gates and so on. The frequency can be stepped with 0.1 Hz precision and the band is arbitrarily chosen from the 0.5-20 MHz range. It takes 10 to 20 secondo to measure and display a spectrum and for the fitting calculation containing several hundred frequencies. The resonant frequency obtained from the Lorentzian-fitting method shows a favorable result in a repeatability typically in the 10-Hz order, or, 10^{-6} relative accuracy, depending on the surface condition and the sample material itself. The mechanisms which contributes to accomplish the EMAR measurement of high absolute accuracy are summarized as follows:

(i) Owing to the noncontacting EMAT, the measurement is insensible to the surface conditions, allowing liftoff and totally unprepared surfaces of test pieces (Hirao et al.,

1993a and 1993b). There is no chance that the coupling condition fluctuates and the data become erroneous. The noncontacting aspect is certainly desirable from the practical standpoint, but more important is the isolation of samples from the transducer. Contacting transducers inevitably distort the reflected signals to a degree. Influence of the contacting transducers and the bonding material is serious, when a high accuracy is required for the velocity or attenuation determination. Low transduction efficiency of EMATs is compensated in excess by getting coherently overlapping echoes at the same time at a resonance.

(ii) Excitation with long, coherent rf bursts serves to enhance the phase interference, destructive or constructive, among many overlapping echoes and then to produce a sharp resonant lineshape. Because of the EMAT's low efficiency, the impinged ultrasonic persists in the sample for a long time, experiencing the multiple reflections. This also serves to the sharp resonant lineshape.

(iii) Integrating over a long gate also contributes to making a sharp resonant spectrum. At a slightly off-resonant frequency, the sample rings down with still large amplitude because of little interference involved. The signal, however, tends to integrate to small value through canceling, since monotonously changing phase produces both positive and negative outputs in the gate.

(iv) Superheterodyne circuitry eliminates the difficult tuning process required to match the receiver's frequency response to that of the signals. The phases of the quadrature phase detector references can be finely adjusted to insure accurate operation over the complete range of frequencies because detection occurs at the fixed intermediate frequency (25MHz). Also, the frequency components other than the excitation frequency are rejected during the heterodyne processing. The present instrumentation should tolerate the noisy environment.

(v) Analog signal processing makes it possible to obtain the spectral response in a very short time, avoiding the analog-to-digital conversion of the whole received signals. But, the total system is computerized and operates flexibly, accommodating various application softwares.

CHAPTER III

COUPLING MECHANISM BETWEEN ELECTROMAGNETIC FIELD AND BULK WAVES

3.1 Introduction

An EMAT consists of a coil element to induce dynamic fields and then eddy currents in the material's surface, and a permanent magnet (or an electromagnet) to provide a bias field. The configuration depends on the mode of the elastic wave to be generated. For the optimum EMAT designing, it is important to understand the coupling mechanism of the EMAT phenomena. This has been a long running topic in the area of the ultrasonics and electromagnetic physics. Previous work (Thompson, 1978 and 1990; Il'in and Kharitonov, 1980; Wilbrand, 1983 and 1987) concluded that three mechanisms are responsible for the coupling between electromagnetic field and elastic deformation; they are (i) the Lorentz force mechanism due to the interaction between the induced eddy current and the bias flux density, (ii) the magnetization force mechanism due to the bias magnetization, and (iii) the magnetostriction mechanism due to the piezomagnetic effect in a ferromagnetic material. The Lorentz force arises in any conducting material, while the other two forces occur only in ferromagnetic materials. For nonmagnetic metals, the transduction is well understood as the Lorentz force mechanism (Gaerttner, 1969), but it is highly complex in case of a ferromagnetic material. Thompson (1978) had studied the field dependence of the guided-wave amplitude in ferromagnetic plates and derived a theoretical model to explain the results. Il'in and Kharitonov (1980) calculated the receiving efficiency for detecting Rayleigh waves by a meanderline coil in a ferromagnetic metal. Wilbrand (1983 and 1987) presented more detailed discussion on the bulk wave detection involving the three mechanisms. They concluded that when the static field is parallel to the sample surface, the magnetostrictive effect dominates, while for the normal field to the surface, the magnetostrictive effect contributes little and the other two mechanisms serve to the wave generation and reception. The theoretical model presented by Wilbrand (1987) is well acceptable, but his conclusion for the case of the normal bias field seems to be insufficient from an experimental viewpoint. He verified his calculation only with the measurement of the directivity pattern of the receiving efficiency of the SV wave. Such a measurement looks at an aspect of the phenomena and is insufficient for the full understanding. Furthermore, his model fails to explain the behavior of the bulk-wave EMAT for a ferro-

magnetic metal as will be shown in detail. Study on the field dependence of the bulk-wave amplitudes provides a pertinent access to clarify the coupling mechanism. The field dependences of the Lorentz force and the magnetization force will be proportional to the magnetization, and that of the magnetostrictive force will be governed by the magnetostriction curve. They show different dependences on the bias field. Such a measurement have to be performed for a thin plate to establish the high grade of field homogeneity in the sample. But, the usual pulse-echo technique is no longer available because of the overlapping of echoes, and then we have to use the EMAR measurement.

This Chapter presents the model analysis on the field dependence of the bulk-wave generation and reception by a spiral elongated coil. Following the existing work, a two-dimensional model is used to estimate the coupling efficiency of the bulk waves. It emphasizes the spatial change of the total field given by the vector sum of the bias field and the dynamic field in the calculation of the magnetostriction constants. This effect plays an essential role in the bulk wave generation, but it has not been taken account in the previous work. The calculation is compared with the measurement data on the field dependence of the bulk-wave amplitudes, which are detected by the EMAR technique as the peak heights of the resonant spectra. Both the experiments and calculations conclude that the magnetostrictive force exerts the dominant contribution to the bulk wave generation and reception, especially, for the shear wave case, regardless of the static field direction. This analysis gives an answer for unsolved behaviors associated with a bulk-wave EMAT and will help us to design new types of EMATs for potential applications in ferromagnetic metals.

3.2. Typical behavior of a bulk-wave EMAT

The bulk-wave EMAT illustrated in Fig.2.1(a) has a compact and robust structure, and is most often used in the practical applications by detecting bulk waves propagating normal to the surface. The permanent magnets produce the normal field to the surface under the coil elements and the tangential field at the center and the edges of the coil elements. It is an experimental fact that this EMAT generates both the shear and the longitudinal waves in a nonmagnetic metal, but it generates only the shear wave in a ferromagnetic metal; the longitudinal wave is too weak to be observed. Figure 3.1 shows the EMAR spectra measured with a bulk-wave EMAT for several metal plates. The results demonstrate that in the nonmagnetic metal, both the shear and longitudinal waves are detected, but for a ferromagnetic metal it detects only the shear wave when the sample is thick; for a thinner plate it detects the longitudinal wave as well.

In the wider region under the coil elements, the Lorentz forces occur parallel to the surface due to the interaction between the normal bias field from the magnets and the eddy currents parallel to the driving current, which become the sources for the

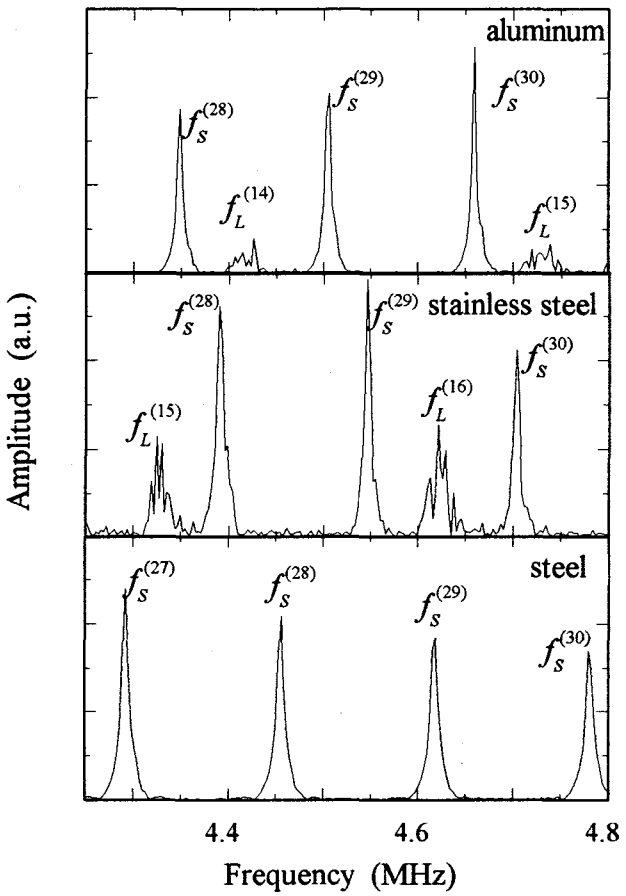

(a) EMAR spectra from plates of 10-mm thick

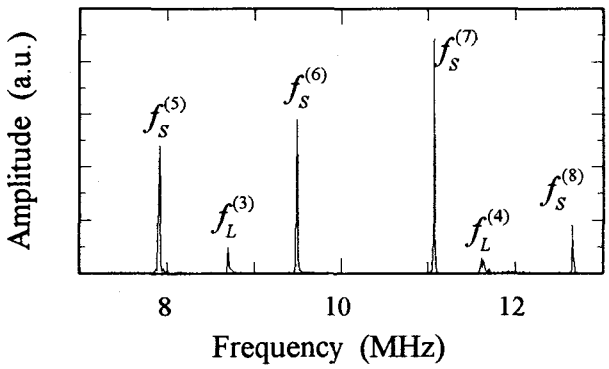

(b) EMAR spectrum from a 1-mm thick steel plate.

Figure 3.1 EMAR spectra detected by a bulk-wave EMAT using the plates of an aluminum, an austenitic stainless steel, and low carbon steels; (a) for 10-mm thick plates, and (b) for the 1-mm thick carbon steel plate. $f_S^{(n)}$ and $f_L^{(n)}$ denote the nth resonant frequencies of the shear and longitudinal waves, respectively. The normal component of the magnetic field is 0.3-0.5 tesla near the magnet poles, and the parallel component is 0.4-0.5 tesla.

shear waves. For the nonmagnetic metals, the Lorentz force also explains the longitudinal-wave generation as a result of the interaction between the tangential field and the eddy current, that is, from their vector product. From an FEM calculation (Ogi et al., 1996b), the tangential field caused by the magnets at the surface region of a ferromagnetic metal is larger than in a nonmagnetic metal. The existing work (Thompson, 1978; I'll and Kharitonov,1980) showed that in a ferromagnetic metal magnetized by the tangential field, the major part of the vertical Lorentz force is canceled by the magnetization force. Certainly, this fact could be an explanation of much smaller coupling efficiency in the longitudinal wave generation. But, it fails to explain why the efficiency is increased for the thinner plate. Furthermore, the existing work concludes that the magnetostriction force is considerable in the presence of the tangential field. If so, the magnetostriction effect would cause the vertical body force in the center region and could be a source to generate the longitudinal wave. However, the longitudinal wave is hardly detected in practice. These contradiction associated with the bulk-wave EMAT will be solved by the following experiments and the theoretical analysis.

3.3. Measurement of field dependence

A spiral elongated coil is placed on a sample surface and the bias magnetic field is supplied, being parallel or normal to the surface. Figure 3.2 shows the setup of the measurements. Sample plate is a low carbon steel, being sized $100^{l}x30^{w}x3^{t}$ mm^3. The solenoidal coil gives the parallel field to the surface up to $7x10^4$ A/m and the electromagnet gives the normal field up to 1.2 tesla. The bias fields on the metal surfaces are measured on the basis of their continuity across the surface. The spiral elongated coil attached on the sample surface is driven by the high-power long bursts with 40-μs duration. The coil is fabricated by printing copper on a polyimide sheet. The coil face is shielded with copper sheets (0.045mm thick) to make only the straight parts active (Fig.3.3). The wave amplitudes are determined from the peak heights of the EMAR spectra. All the measurements were performed after cyclic demagnetization; that is, the magnetization always progresses along the initial magnetization curve.

Figure 3.4 shows the measured resonant spectrum of the steel plate for the tangential bias field of $1.4x10^4$ A/m. To compare with a nonmagnetic-metal case, the spectrum of the 3-mm-thick plate of an aluminum alloy is also shown there. It is found that no shear wave signal is detected for the aluminum sample, but both the longitudinal and shear wave signals are detected for the steel sample, indicating the different excitation mechanism between the nonmagnetic and magnetic metals. Measurement of the field dependences is made on the resonant spectra of the fourth longitudinal resonant mode ($f_L^{(4)}$) and the eighth shear resonant mode ($f_S^{(8)}$) for both bias field cases. Figure 3.5 presents the field dependences of their amplitudes. The amplitudes have been normalized by the maximum shear-wave amplitude in the normal bias field case. We

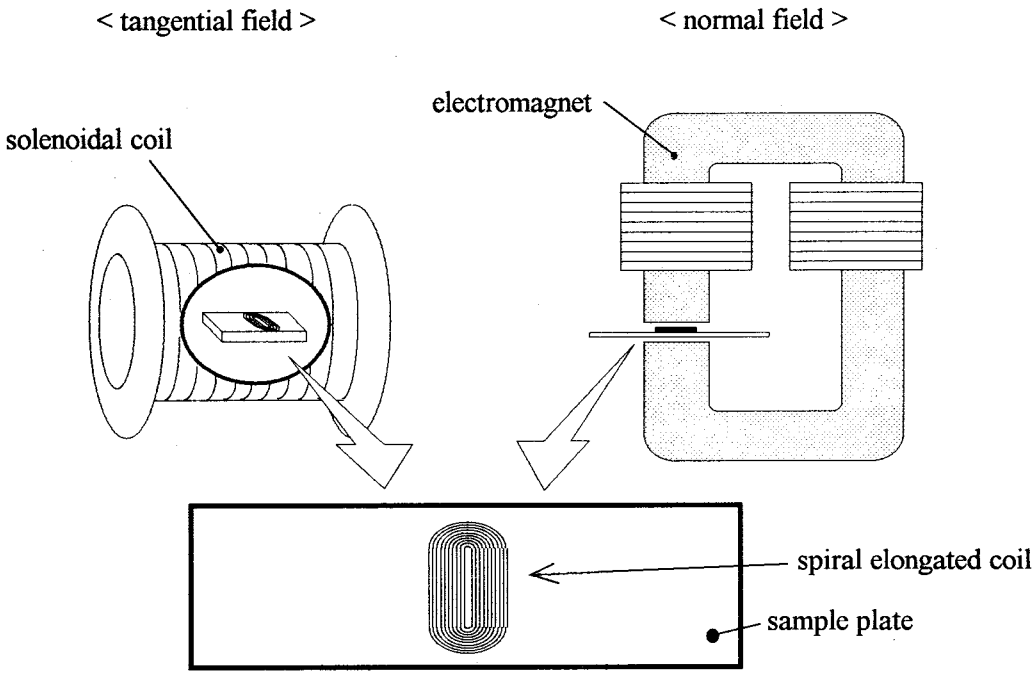

Figure 3.2 Configurations for measuring the field dependence with the spiral elongated coil and bias fields.

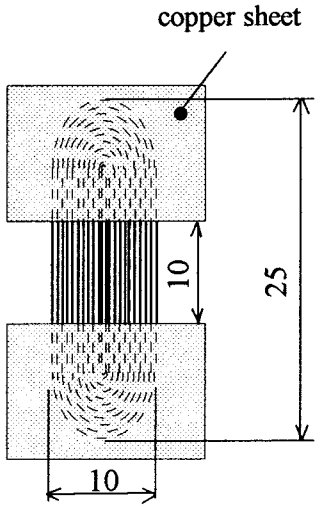

Figure 3.3 Details of the spiral elongated coil. The coil face of the sample side is shielded by copper sheets to make the active area of 10x10mm^2. The turn number of the coil is 22.

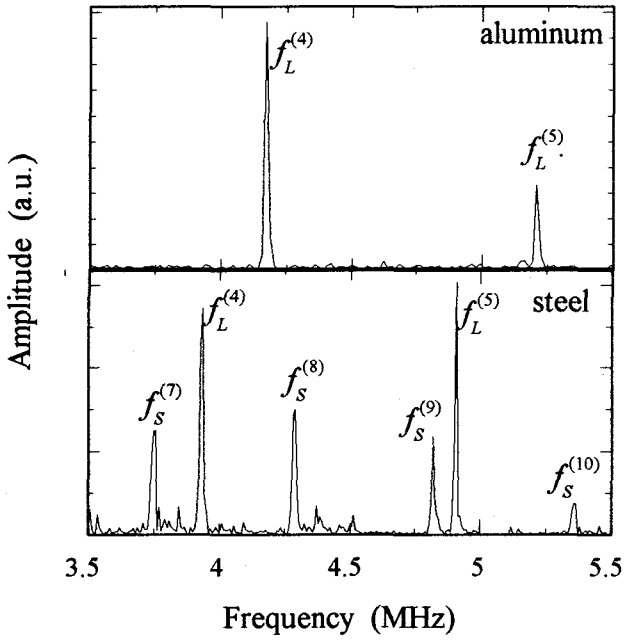

Figure 3.4 EMAR spectra for 3mm-thick plates of an aluminum and the carbon steel. The tangential field to the surface is 1.4×10^4 A/m.

have the following observations; (i) the shear-wave amplitude for the normal bias field shows the largest magnitude and (ii) it has a small peak in the lower field region; (iii) the longitudinal-wave amplitude for the normal bias field increases with the field and after taking a maximum value, it becomes suitable up to 1.2 tesla; (iv) there are two peaks in the tangential-field dependence of the shear wave; and (v) the longitudinal-wave amplitude monotonously increases for the tangential field case. Since the Lorentz force and the magnetization force mechanisms will cause monotonous dependence as characterized by the magnetization curve, it is apparent that these mechanisms cannot explain the above observations.

3.4. Theoretical analysis

3.4.1. Modeling

The basic equations governing the coupling of the electromagnetic field and the elastic deformation **u** are given by (Landau and Lifshitz, 1959; Il'in and Kharitonov, 1980; Wilbrand, 1983 and 1987)

$$\rho \frac{\partial^2 \mathbf{u}}{\partial t^2} = \nabla \cdot \mathrm{T} + \mathbf{f}, \tag{3.1}$$

$$\mathrm{rot}\mathbf{E} = -\frac{\partial \mathbf{B}}{\partial t}, \tag{3.2}$$

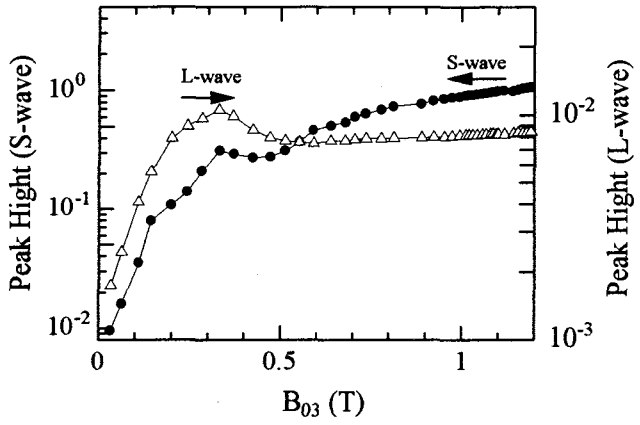

(a) normal bias field

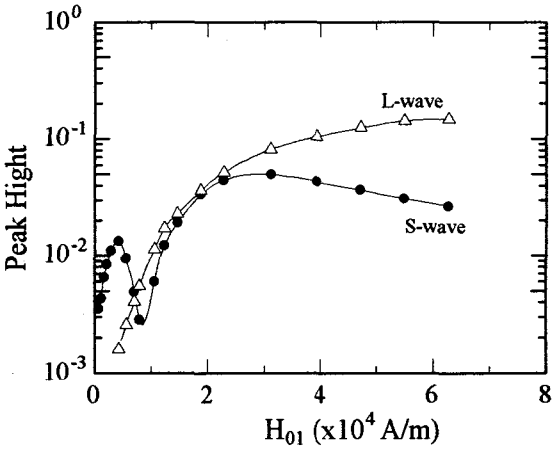

(b) tangential bias field

Figure 3.5 Field dependences of the spectrum-peak height for the steel plate. Plotted are the response at the 4th resonant frequency for the longitudinal wave and the 8th one for the shear wave.

$$\mathrm{rot}\mathbf{H} = \frac{\partial \mathbf{D}}{\partial t} + \mathbf{J}, \tag{3.3}$$

$$\mathbf{E} = \sigma^{-1}\mathbf{J} + \frac{\partial \mathbf{u}}{\partial t} \times \mathbf{B}_0, \tag{3.4}$$

$$\mathbf{B} = \mu_0 \mu \cdot (\mathbf{H} - \mathbf{M}_0 \nabla \cdot \mathbf{u}) + e \cdot \varepsilon, \tag{3.5}$$

where **E** is the electric field, **B** the magnetic flux density, **H** the magnetizing field, **D** the dielectric displacement, **J** the current density, ρ the mass density, T the elastic stress tensor, and **f** the body force per unit volume. They are all time-dependent quantities. $\mathbf{B}_0$ and $\mathbf{M}_0$ are the bias magnetic flux density and magnetization. σ and μ_0 are the electrical conductivity and the free-space permeability. μ, *e*, and ε are tensors of the differential magnetic permeability, the piezomagnetic constants, and the strain caused by the ultrasonic, respectively. The terms involving **u** and ε in Eqs.(3.4) and (3.5) are

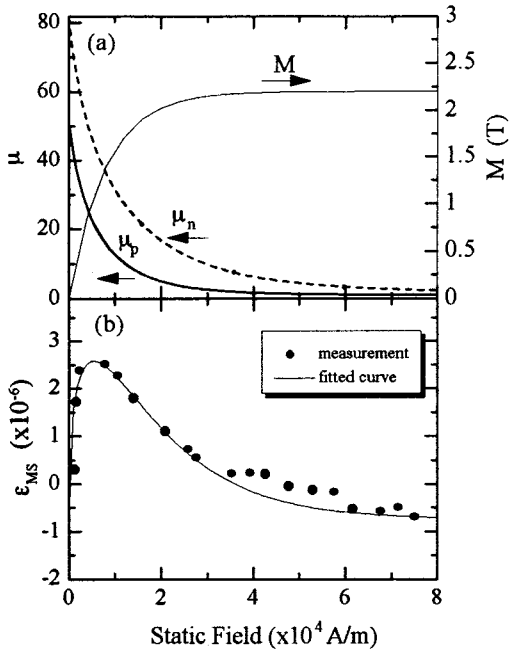

Figure 3.6 (a) Simplification of the initial magnetization curve and calculation of the permeabilities, and (b) magnetostriction curve based on the measurements.

considered only in the analysis for the receiving process.

Some approximations are used for simplification. The rest of this section summarizes the formulation and the assumptions, including the magnetization curve, the anisotropic permeability, and the magnetostriction curve.

The electromagnetic and the elastodynamic fields are variables in the two-dimensional space of the x_1-x_3 plane (see Fig.3.8). The half space of $x_3>0$ is filled with a ferromagnetic metal, in which the x_1-x_2 plane defines the interface with vacuum. The bias field is homogeneous being normal or parallel to the surface. The magnetostriction causes no volume change (isovolume); this is true for anisotropic polycrystalline metal, because the randomly oriented easy axes averages out the anisotropy of the magnetostriction of individual magnetic domains (Chikazumi, 1964). We also assume that the displacement current $\partial \mathbf{D}/\partial t$ is neglected because of the relatively low frequency range; the magnetic states are reversibly changed through the rotation of the magnetization.

The formula presented by Potter and Schulian (1971) is used to express the response of the magnetization (M: tesla) to the field (H: 10^4A/m):

$$M = 2.2\{0.27 - 0.73\tanh(0.38 - 1.1H)\}, \tag{3.6}$$

which is derived as the initial magnetization curve of the material with the saturation magnetization of 2.2 tesla and the residual magnetization of 0.8 tesla (Fig.3.6(a)). This is an acceptable approximation for the practical initial magnetization curve of a low carbon steel.

With the magnetic anisotropy induced by the bias field, the nonzero components in the permeability tensor μ in Eq.(3.5) are equal to μ_p or μ_n, which is the permeability parallel or normal to the bias field, respectively. Generally, the anisotropy originates from the rotation of the magnetization and the movement of the domain walls. But, because the material is magnetized by the dynamic field with a high frequency and a small amplitude in the EMAT phenomena, the domain walls will not oscillate responding to the field vibration. Only the rotation of the magnetization is then considered. The anisotropic permeability tensor is calculated following Chikazumi (1964). In a domain of a ferromagnetic metal with the cubic crystallographic symmetry, the magnetic energy is expressed by

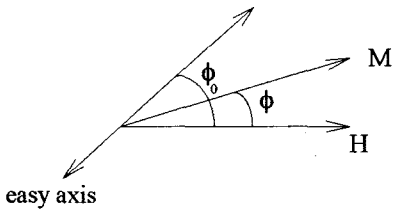

Figure 3.7 Rotation of magnetization about an easy axis

$$U=K_1\cos^2(\phi_0-\phi)\sin^2(\phi_0-\phi)-M_sH\cos\phi, \tag{3.7}$$

when the magnetization rotates in the plane involving an easy axis. K_1 is the first magnetic anisotropy constant and M_s is the saturation magnetization. ϕ and ϕ_0 are angles between the field and the magnetization and between the field and the easy axis, respectively (see Fig.3.7). The stable direction is determined by minimizing the energy, that is, $\partial U/\partial\phi=0$. The magnetization parallel and normal to the external field H is obtained by $M_s\cos\phi$ and $M_s\sin\phi$. The values for μ_p and μ_n are given by differentiating M_p and M_n with respect to H:

$$\mu_p=\partial(M_s\cos\phi)/\partial H,\quad \mu_n=\partial(M_s\cos\phi)/\partial H\,. \tag{3.8}$$

Because an isotropic polycrystalline metal is composed of the randomly oriented grains, the permeabilities are determined by averaging Eq.(3.8) for all possible angles of ϕ_0. Figure 3.6(a) shows the permeabilities thus calculated.

Magnetostriction (ε_{MS}) is measured with the steel plate used in the field-dependence experiment and is approximated by

$$\varepsilon_{MS}=3.5H^{0.395}\cdot 1.79^{(-1.3H+1)}-0.75, \tag{3.9}$$

where ε_{MS} is in unit of microstrain and H in 10^4 A/m. Figure 3.6(b) compares the measurement and the fitted function.

3.4.2. Generation mechanism

The elastic wave field induced in the metal is governed by Eq.(3.1) with an electromagnetic body force **f**, which can be expressed by the summation of the Lorentz force $\mathbf{f}^{(L)}$, the magnetization force $\mathbf{f}^{(M)}$, and the magnetostriction force $\mathbf{f}^{(MS)}$ as

$$\mathbf{f}^{(L)} = \mathbf{J}_e \times \mathbf{B}_0, \tag{3.10}$$

$$\mathbf{f}^{(M)} = (\nabla \mathbf{H}) \cdot \mathbf{M}_0, \tag{3.11}$$

$$\mathbf{f}^{(MS)} = \nabla \cdot (\mathbf{e} \cdot \mathbf{H}), \tag{3.12}$$

where $\mathbf{J}_e$ is the eddy current density and e is the tensor of the magnetostriction constants. Furthermore, the traction force $T_{33}^{(M)}$ normal to the surface per unit area due to the bias magnetization contributes to the wave generation:

$$T_{33}^{(M)} = \frac{1}{\mu_0} M_{03} M_n, \tag{3.13}$$

where M_n denotes the normal component at the surface of the magnetization of the metal. This term occurs as a result of the steep change of the electromagnetic field near the surface of a magnetized metal (Iida, 1975). Because the forces in Eqs.(3.10)-(3.13) are caused by the electromagnetic fields in the metal, the calculation of the wave amplitude starts with deriving the fields in the metal induced by the driving current.

Consider the electromagnetic transduction with a harmonic excitation in a two-dimensional half space occupied by an isotropic polycrystalline (Fig.3.8). Coil elements are located near the surface with a liftoff h, and driven by the current of $I_0 e^{j\omega t}$, ω being angular frequency. The expression of $e^{j\omega t}$ is omitted hereafter. Analogous procedure to the previous work (Thompson, 1990) leads to the Fourier transform expression of the sheet current $K(x_1,-h)$ per unit length along the x_1 axis:

$$K(x_1,-h) = \frac{I_0}{a} \sum_{m=0}^{\infty} \left[(-1)^m \frac{4}{(2m+1)} \sin\left(\frac{a}{2} k_m\right) \sin k_m x_1 \right], \tag{3.14}$$

where $k_m = 2\pi(2m+1)/D$ is characteristic to the spiral-coil dimensions. Substituting Eq.(3.5) into Eq.(3.3), and eliminating the electric field with Eq.(3.4), we find that the magnetic field $\mathbf{H}^V$ in vacuum satisfies Laplace's equation. It is easily solved with the boundary condition of $H_1^V = K/2$ at $x_3 = -h$. In the metal region, a similar procedure reduces the simultaneous equations (3.2)-(3.5) to a second-order differential equation for H_1 by using $\partial^2 H_1 / \partial x_1^2 = -k_m^2 H_1$. The general solution of H_1 contains a complex amplitude, which is determined by the continuity of the tangential field at the boundary between the vacuum and metal regions ($H_1^V = H_1$ at $x_3 = 0$). H_3 is also obtained from H_1 by Eqs.(3.2) and (3.5). The solutions thus derived consist of a series of terms including $e^{-2\pi(2m+1)h/D}$ and they decrease as m becomes larger. For focussing on the primary effect, the terms in the higher orders (m>0) are neglected. This is allowable for a large liftoff. The resultant expressions then become

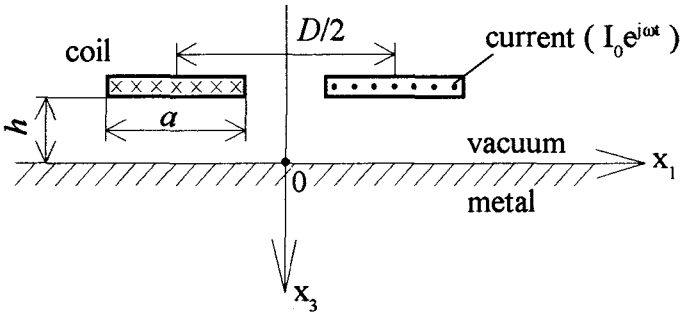

Figure 3.8 Two-dimensional model to explain the electromagnetic phenomena caused by the spiral elongated coil.

$$H_1 = -j\frac{2I_0}{a\pi}\sin\left(\frac{a}{D}\pi\right)e^{qx_3}e^{jk_0x_1}e^{-k_0h} \quad , \tag{3.15}$$

$$H_3 = -\frac{\mu_{11}}{\mu_{33}}\frac{k_0}{q}\frac{2I_0}{a\pi}\sin\left(\frac{a}{D}\pi\right)e^{qx_3}e^{jk_0x_1}e^{-k_0h} \quad , \tag{3.16}$$

$$k_0 = 2\pi/D,\ q = -(\alpha + j\alpha^{-1})/\delta,$$

$$\delta = \sqrt{2/(\sigma\omega\mu_0\mu_{11})},\ \ \alpha = \sqrt{(k_0\delta)^2(\mu_{11}/\mu_{33})/2+1}\ .$$

(a) Lorentz force and magnetization force

The Lorentz force and the magnetization force are obtained by substituting Eqs.(3.15) and (3.16) into Eqs.(3.3), (3.10) and (3.11):

$$f_1^{(L)} + f_1^{(M)} = C_{11}^{(L)}\frac{\partial H_1}{\partial x_3} + C_{13}^{(M)}\frac{\partial H_3}{\partial x_3} - (B_{03} - M_{03})\frac{\partial H_3}{\partial x_1}, \tag{3.17}$$

$$f_3^{(L)} + f_3^{(M)} = \left(C_{31}^{(L)} + C_{31}^{(M)}\right)\frac{\partial H_1}{\partial x_3} + C_{33}^{(M)}\frac{\partial H_3}{\partial x_3} + (B_{01} + M_{01})\frac{\partial H_3}{\partial x_1}\ , \tag{3.18}$$

$C_{11}^{(L)}=B_{03}$, $C_{31}^{(L)}=-B_{01}$,

$C_{13}^{(M)}=-(\mu_{33}/\mu_{11})M_{01}$, $C_{31}^{(M)}=M_{01}$, and $C_{33}^{(M)}= M_{03}$.

where C_{ij} represents the coefficient of the body force f_i proportional to the gradient of the dynamic field H_j in the x_3 direction. The terms involving $\partial H_3/\partial x_1$ are small enough relative to others; they will be neglected in the following discussions. Considering that H_1 is much larger than H_3 in magnitude and the well known relation of $\mathbf{B}_0=\mu_0\mathbf{H}+\mathbf{M}_0$, we find that $f_3^{(L)}$ and $f_3^{(M)}$ act in the opposite directions and $f_3^{(M)}$ cancels the major part of $f_3^{(L)}$, that is, $C_{31}^{(L)}+C_{31}^{(M)}=-\mu_0H_{01}$. The magnitude of μ_0H_{01} is much smaller than M_{01} in the field region used in the experiments, implying the small contribution of $f_3^{(L)}+f_3^{(M)}$ to the elastic wave generation. This cancellation has been pointed out by Thompson (1978) experimentally and by I'll and Kharitonov (1980) theoretically.

(b) Magnetostrictive force

In case of the magnetic metals, the magnetization accompanies the domain wall movement and rotation, leading to the dimensional change in the magnetization direction, which is called magnetostriction. Magnetostriction changes responding to the dynamic field, resulting in the ultrasonic source. In a polycrystalline metal, the volume change due to magnetostriction is fairly small (Poisson's ratio: $\nu \sim 0.5$), which differs from the ordinary elastic deformation without applying a magnetic field ($\nu \sim 0.3$).

The magnetostriction constant $e_{k,ij}$ in Eq.(3.12) represents the dynamic response of the magnetostrictive stress σ_{ij} to the field H_k. Using the magnetostriction ε_{mn} which depends on the total field, $e_{k,ij}$ is expressed as follows (Berlincourt et al, 1964; Thompson, 1978):

$$e_{k,ij} \equiv \left(\frac{\partial \sigma_{ij}}{\partial H_k}\right) = \left(\frac{\partial \sigma_{ij}}{\partial \varepsilon_{mn}}\right)_{H=0} \left(\frac{\partial \varepsilon_{mn}}{\partial H_k}\right)_{\sigma=0}, \tag{3.19}$$

where $\left(\partial \sigma_{ij}/\partial \varepsilon_{mn}\right)_{H=0}$ can be replaced by the elastic stiffness. In Eq.(3.19), the summation convention is implied.

It is difficult to determine $e_{k,ij}$ by experiments. Il'in and Kharitonov (1980) and Wilbrand (1983) used rough approximation for it; Thompson (1978) derived it from the slope of magnetostriction response to the bias field. The present analysis, however, takes account of the magnetostriction change responding to the total field, which is very important for the wave generation as will be shown later.

When the dynamic field is superimposed on the bias field, the total field is inclined from the original direction. Because the magnetostriction tends to occurs in both the parallel and normal directions to the total field, we should consider the principal coordinate system to calculate σ_{ij}. Considering a new system (x_1', x_2', x_3') where the total magnetic field lies along the x_1' direction and $x_2'=x_2$, only three principal stresses (σ'_{11}, σ'_{22}, and σ'_{33}) exist. Because of the isovolume magnetostriction, the magnitude of the magnetostriction along the applied field is twice larger than those in the perpendicular directions, being in the opposite sign. Supposing $\partial \varepsilon_2'/\partial H_1' = \partial \varepsilon_3'/\partial H_1' = -\left(\partial \varepsilon_1'/\partial H_1'\right)/2$ and using Hooke's law, Eq.(3.19) is reduced to

$$\left.\begin{aligned} \partial \sigma_{11}'/\partial H_1' &= 6\kappa G \\ \partial \sigma_{22}'/\partial H_1' &= -3\kappa G \\ \partial \sigma_{33}'/\partial H_1' &= -3\kappa G \end{aligned}\right\}, \tag{3.20}$$

where G is the shear modulus and $\kappa = \partial \varepsilon_{11}'/\partial H_1'$ is a function of the total field and given from the slope of the magnetostriction curve in Fig.3.6(b). Introducing the direction cosine Q_{ij} between the x_i' and x_j axes, we have $\sigma_{ij} = \sigma'_{mn} Q_{mi} Q_{nj}$. In the present two-dimensional model, Q_{ij} are calculated using an angle θ between the total field and the

bias field, and we have

$$\sigma_{11} = \sigma'_{11}\sin^2\theta + \sigma'_{33}\cos^2\theta, \quad \sigma_{33} = \sigma'_{11}\cos^2\theta + \sigma'_{33}\sin^2\theta$$
$$\sigma_{13} = (\sigma'_{11} - \sigma'_{33})\sin\theta\cos\theta, \tag{3.21}$$

for a normal bias field, and

$$\sigma_{11} = \sigma'_{11}\cos^2\theta + \sigma'_{33}\sin^2\theta, \ \sigma_{33} = \sigma'_{11}\sin^2\theta + \sigma'_{33}\cos^2\theta,$$
$$\sigma_{13} = (\sigma'_{11} - \sigma'_{33})\sin\theta\cos\theta, \tag{3.22}$$

for a tangential bias field. The magnetostriction constants $e_{k,ij}$ are obtained from Eqs.(3.19)-(3.22) for each of the normal and the tangential fields:

(i) normal bias field

$$\left.\begin{aligned} e_{1,11} &= 3\kappa G\sin\theta(2\sin^2\theta - \cos^2\theta) + \frac{6G\varepsilon'_{11}}{H_{03}}\cos^3\theta\sin\theta, \\ e_{1,13} &= 9\kappa G\sin^2\theta\cos\theta + \frac{3G\varepsilon'_{11}}{H_{03}}\cos 2\theta\cos^2\theta, \\ e_{1,33} &= 3\kappa G\sin\theta(2\cos^2\theta - \sin^2\theta) - \frac{6G\varepsilon'_{11}}{H_{03}}\cos^3\theta\sin\theta, \\ e_{3,11} &= -3\kappa G, \quad e_{3,13} = 0, \quad e_{3,33} = 6\kappa G \end{aligned}\right\}, \tag{3.23}$$

$$\theta = \tan^{-1}(H_1 / H_{03})$$

(ii) tangential bias field

$$\left.\begin{aligned} e_{1,11} &= 6\kappa G, \ e_{1,13} = 0, \ e_{1,33} = -3\kappa G \\ e_{3,11} &= 3\kappa G\sin\theta(2\cos^2\theta - \sin^2\theta) - \frac{6G\varepsilon'_{11}}{H_{01}}\cos^3\theta\sin\theta, \\ e_{3,13} &= 9\kappa G\sin^2\theta\cos\theta + \frac{3G\varepsilon'_{11}}{H_{01}}\cos 2\theta\cos^2\theta, \\ e_{3,33} &= 3\kappa G\sin\theta(2\sin^2\theta - \cos^2\theta) + \frac{6G\varepsilon'_{11}}{H_{01}}\cos^3\theta\sin\theta \end{aligned}\right\}. \tag{3.24}$$

$$\theta = \tan^{-1}(H_3 / H_{01})$$

The body force $\mathbf{f}^{(MS)}$ due to the magnetostrictive effect is determined by

$$f_i^{(MS)} = \partial\sigma_{ij}/\partial x_j = e_{k,ij}\left(\partial H_k/\partial x_j\right), \tag{3.25}$$

or

$$f_1^{(MS)} = C_{11}^{(MS)}\frac{\partial H_1}{\partial x_3} + C_{13}^{(MS)}\frac{\partial H_3}{\partial x_3}, \quad f_3^{(MS)} = C_{31}^{(MS)}\frac{\partial H_1}{\partial x_3} + C_{33}^{(MS)}\frac{\partial H_3}{\partial x_3}, \tag{3.25}'$$

and we can define coefficients $C_{ij}^{(MS)}$ like in Eqs.(3.17) and (3.18) as follows:

$$\left.\begin{aligned} C_{11}^{(MS)} &= e_{1,13},\ C_{13}^{(MS)} = -\frac{\mu_{33}}{\mu_{11}} e_{1,11}, \\ C_{31}^{(MS)} &= e_{1,33},\ C_{33}^{(MS)} = e_{3,33} - \frac{\mu_{33}}{\mu_{11}} e_{1,13} \end{aligned}\right\},\ \text{normal bias field,} \tag{3.26}$$

$$\left.\begin{aligned} C_{11}^{(MS)} &= 0,\ C_{13}^{(MS)} = -\frac{\mu_{33}}{\mu_{11}} e_{1,11} + e_{3,13}, \\ C_{31}^{(MS)} &= e_{1,33},\ C_{33}^{(MS)} = e_{3,33} \end{aligned}\right\},\ \text{tangential bias field.} \tag{3.27}$$

It should be noted that when the inclination of the total field is ignored (σ_{13}=0), the expressions for $e_{k,ij}$ are quite different from above results. Especially, in the case of the normal bias field, $e_{1,13}$ will be equal to zero. However, it is considerably large even in the high field limit (θ=0) in Eq.(3.23), and can contribute to $f_1^{(MS)}$ in the present model.

(c) Wave amplitude

Body forces obtained in Eqs.(3.17), (3.18), and (3.25)' are coupled to the bulk waves in Eq.(3.1). Taking the longitudinal wave for example, Eq.(3.1) is reduced to the following differential equation by noting $\partial^2 u_3/\partial x_1^2 = -k_0^2 u_3$:

$$\frac{\partial^2 u_3}{\partial x_3^2} + (k_3^2 - k_0^2)u_3 = -\frac{f_3}{\lambda + 2G}\ , \tag{3.28}$$
$$k_3 = \omega / c_L,\ c_L = \sqrt{(\lambda + 2G)/\rho}$$

where λ is one of Lame's constants. Particular solution is first obtained and then the general solution is expressed by the summation of the particular solution and the homogeneous solution. The general solution includes an unknown constant, which is determined by the stress-free condition at x_3=0 together with Eq.(3.13). The resultant expression of the general solution consists of two terms; one is proportional to $e^{-\frac{\alpha}{\delta}x_3}$ and rapidly decays in the thickness direction. The other term carries energy into the metal and represents the generated ultrasonic wave. The expression of the term for the longitudinal wave is

$$u_3 = \frac{2I_0 \sin(\alpha\pi / D)}{\alpha\pi K(\lambda + 2G)}\left[\left(\frac{\mu_{11}}{\mu_{33}}\Delta_0(\Delta_3^2 - \Delta_0^2 - 2)C_{33} - 4C_{31}\right)\right.$$
$$\left. + j\left(\frac{\mu_{11}}{\mu_{33}}\Delta_0(\Delta_3^2 - \Delta_0^2 + 2)C_{33} + 2(\Delta_3^2 - \Delta_0^2)C_{31}\right)\right] e^{j(-Kx_3 + k_0 x_1)}\ , \tag{3.29}$$

where Δ_0=$k_0\delta$, Δ_3=$k_3\delta$, and K^2=k_3^2-k_0^2. Similar procedure leads to the solution for the

shear wave.

The ultrasonic amplitude thus derived will be in the form

$$u_i = u_i^{(L)} + u_i^{(M)} + u_i^{(MS)}, \quad i=1 \text{ or } 3. \tag{3.30}$$

and the contribution of each mechanism for the elastic wave generation can be discussed separately. Figure 3.9 shows the field dependence of the bulk-wave amplitudes due to the magnetostrictive effect normalized by the Lorentz force contribution for the longitudinal wave ($|u_i^{(MS)}|/|u_3^{(L)}|$) for each static field. Used parameters are as follows; f=4MHz, D=20mm, a=4.5mm, h=0.5mm, I_0=50A, G=80GPa, λ=120GPa, σ=3.3x10^{6}S/m, and μ_0=1.26x10^{-6}H/m, which are compatible with the experimental condition. The contributions of the magnetization mechanism and that of the tangential Lorentz force are not included in Fig.3.9 because of the similarity to the vertical Lorentz force case ($|u_1^{(L)}| \sim [(\lambda+2G)/G]|u_3^{(L)}|$, $|u_3^{(M)}| \sim |u_3^{(L)}|$, $|u_1^{(M)}| << |u_3^{(L)}|$).

Figure 3.9 indicates much larger contribution of the magnetostriction effect to the bulk-wave generation than the others, especially in the lower field region. As the external field increases, the contributions of the Lorentz force and the magnetization force become comparable with the magnetostriction effect. The bias field exerted by a permanent magnet in a low carbon steel is usually less than 4x10^4 A/m (Ogi et al., 1996b), suggesting that the magnetostriction mechanism governs the bulk-wave generation as a whole, regardless of the field direction. We also find the smaller generation efficiency in the tangential bias field than in the normal bias field. Especially, the efficiency of the shear-wave generation in the tangential bias field is the smallest. The shear wave amplitude $|u_1^{(MS)}|$ in the tangential field case is nearly proportional to $\Delta_0(=k_0\delta)$. The ignorance of the higher-order terms of the Fourier transform expression of the dynamic field smoothes out the steep change of the field around the center region of the coil elements near x_1=0. This makes k_0 less than that of the practical value and therefore underestimates the shear wave amplitude. But the field dependence is not so much affected by this ignorance because it mainly depends on the field dependences of the permeability, the magnetization, and the magnetostriction response.

3.4.3. Receiving mechanism

The excited ultrasonic wave travels in the thickness direction, is reflected at the bottom surface, and then returns to the incident surface. Because of the inverse magnetostriction effect, the elastic deformation due to the ultrasonic wave disturbs the electromagnetic field, giving rise to the dynamic fields. The coupling occurs at the boundary between the metal and vacuum regions and the excited field are detected by the coil element placed in the vacuum region. Il'in and Kharitonov (1980) calculated the electric field in the vacuum region induced by the Rayleigh waves. Their procedure is applied here for calculating the electric field induced in the vacuum region by the

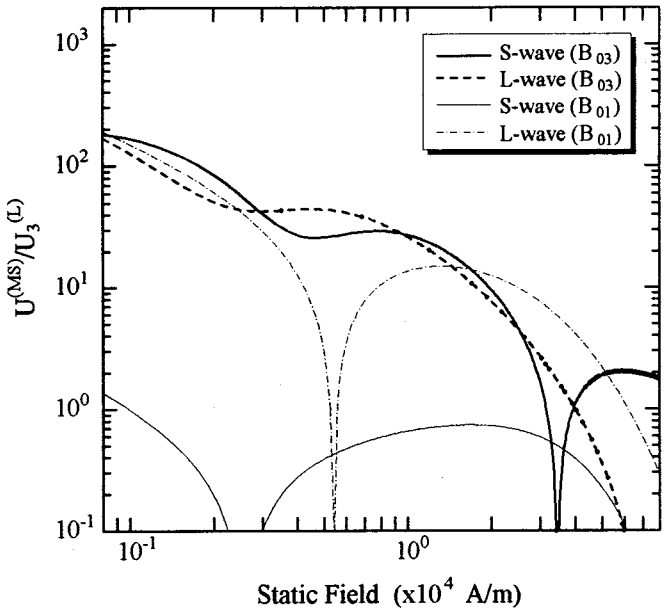

Figure 3.9 Calculation of the field dependence of the generated amplitudes of bulk waves.

bulk waves, although the derivation of the piezomagnetic constants has been modified.

The piezomagnetic constants $e_{k,ij}$ in Eq.(3.5) represent the generation ratio of the magnetic flux density B_k induced by the elastic strain ε_{ij} (Berlincourt, 1964):

$$e_{k,ij} = \left(\frac{\partial B_k}{\partial \varepsilon_{ij}}\right) = \mu_{kk}\left(\frac{\partial H_k}{\partial \varepsilon_{ij}}\right) . \tag{3.31}$$

Summation is not implied by the repeated indices. Uniform bias field causes the orthogonal anisotropy in the magnetic properties of a ferromagnetic material that is originally isotropic. One of the principal axes coincides with the field direction. Therefore, only three piezomagnetic constants have to be taken into account. They are denoted by e_{33}, e_{31}, and e_{15}. e_{33} is the constant for the parallel magnetic induction to the bias field due to the principal strain along the bias field; e_{31} the constant for the parallel magnetic induction due to the principal strain normal to the field, and e_{15} the constant for the normal magnetic induction to the bias field due to the shear strain ε_{13}. e_{31} is approximated by $-\nu e_{33}$ by noting $\partial H_3/\partial \varepsilon_{11} = (\partial H_3/\partial \varepsilon_{33})(\partial \varepsilon_{33}/\partial \varepsilon_{11})$.

Considering the bias field direction and the wave mode, the calculation of receiving efficiency is carried out for four cases:

(i) $\mathbf{u}=(u_1 e^{j(k_3x_3+k_0x_1)}, 0, 0)$ and $\mathbf{B}=(0, 0, B_{03})$
(ii) $\mathbf{u}=(u_1 e^{j(k_3x_3+k_0x_1)}, 0, 0)$ and $\mathbf{B}=(B_{01}, 0, 0)$
(iii) $\mathbf{u}=(0, 0, u_3 e^{j(k_3x_3+k_0x_1)})$ and $\mathbf{B}=(0, 0, B_{03})$
(iv) $\mathbf{u}=(0, 0, u_3 e^{j(k_3x_3+k_0x_1)})$ and $\mathbf{B}=(B_{01}, 0, 0)$

For example, case (i) is explained in the following. This is the case that the shear wave polarized in the x_1 direction is impinged on the surface region where the normal bias field is present. In the metal region, Eq.(3.5) is reduced to

$$\left.\begin{aligned} B_1 &= \mu_0\mu_{11}H_1 + +e_{15}\frac{\partial u_1}{\partial x_3} \\ B_3 &= \mu_0\mu_{33}H_3 + (\mu_{33}M_{03} + e_{31})\frac{\partial u_1}{\partial x_1} \end{aligned}\right\} . \tag{3.32}$$

Substituting Eq.(3.32) into Eq.(3.2) and eliminating H_1 and H_3 using Eqs.(3.3) and (3.4), we obtain a differential equation for E_2:

$$\frac{\partial^2 E_2}{\partial x_3^2} - q^2 E_2 = B_{03}\omega u_1 - j\left\{\left(k_3^2 e_{15} - \frac{\mu_{33}}{\mu_{11}}k_1^2\right) + k_1^2\mu_{11}M_{03}\right\}\omega u_1 , \tag{3.33}$$

$$q^2 = \frac{\mu_{33}}{\mu_{11}}k_1^2 + j\frac{2}{\delta^2} .$$

The particular solution in the form of $E_2 = Ae^{j(k_3x_3+k_0x_1)}$ is considered, and the complex amplitude A is determined by substituting it into Eq.(3.33). The general solution takes the form of $E_2 = (Ce^{qx_3} + Ae^{jk_3x_3})e^{jk_0x_1}$ with unknown C. On the other hand, Eq.(3.33) takes the following form in the vacuum region

$$\frac{\partial^2 E_2^V}{\partial x_3^2} - k_0{}^2 E_2^V = 0 , \tag{3.34}$$

and the solution is $E_2^V = De^{k_0x_3}e^{jk_0x_1}$. The unknown complex amplitudes C and D are determined by the boundary condition at the surface, which is perturbed responding to the elastic wave:

$$\mathbf{n}_0 \times (\mathbf{E}^V - \mathbf{E}) = V_3(\mathbf{B}_0^V - \mathbf{B}_0) , \tag{3.35}$$

$$\mathbf{n}_0 \times (\mathbf{H}^V - \mathbf{H}) + \mathbf{n}' \times (\mathbf{H}_0^V - \mathbf{H}_0) = 0 , \tag{3.36}$$

where $\mathbf{n}_0$ is an outward unit vector normal to the surface and $\mathbf{n}'$ is the one when the surface is displaced by the ultrasonic wave. V_3 is the normal component of the particle velocity at the boundary. By using the relations of $B_{03}{}^V - B_{03} = -M_{03}$ and $H_{03}{}^V - H_{03} = M_{03}/\mu_0$, the continuity of the electromagnetic fields at a boundary ($B_3{}^V = B_3$ and $H_1{}^V = H_1$), and $n_1' \sim -(\partial u_3 / \partial x_1)_{|x_3=0}$, Eqs.(3.35) and (3.36) lead to

$$E_2^V - E_2 = -M_{01}\left(\frac{\partial u_3}{\partial t}\right)_{|x_3=0}, \quad H_1^V - H_1 = M_{03}\left(\frac{\partial u_3}{\partial x_1}\right)_{|x_3=0} . \tag{3.37}$$

From these relations, we have the electric field $E_2{}^V$ and it is expressed by the contribution of each mechanism:

$$E_2^V = E^{(L)}B_{03} + E^{(M)}M_{03} + E^{(MS1)}e_{15} + E^{(MS2)}e_{33}\ , \tag{3.38}$$

where

$$\left.\begin{aligned} E^{(L)} &= -\frac{\tau}{2\xi}[(-\eta\chi + 2\zeta) + j(\zeta\chi + 2\eta)]\omega u_1 \\ E^{(MS1)} &= \frac{\Delta_3}{4\xi}[(2\eta\kappa\Delta_3 + \zeta\kappa\chi\Delta_3 + 4\beta) + j(-2\zeta\kappa\Delta_3 + \eta\kappa\chi\Delta_3 - 4/\alpha)]\omega u_1 \\ E^{(MS2)} &= \frac{\nu\tau\Delta_1^2}{4\xi}\frac{\mu_{11}}{\mu_{33}}[(2\eta + \zeta\chi) + j(-2\zeta + \eta\chi)]\omega u_1 \\ E^{(M)} &= \frac{\tau\Delta_1^2\mu_{11}}{4\xi}[(2\eta + \zeta\chi) + j(-2\zeta + \eta\chi)]\omega u_1 \end{aligned}\right\}, \tag{3.39}$$

and

$$\left.\begin{aligned} &\chi = \Delta_3^2 + \frac{\mu_{11}}{\mu_{33}}\Delta_1^2,\ \tau = (1 + \chi^2/4)^{-1},\ \xi = \beta^2 + \alpha^{-2}, \\ &\eta = \alpha\beta + \gamma\alpha^{-1},\ \zeta = 1 - \beta\gamma,\ \beta = \alpha + \mu_{11}\Delta_1,\ \gamma = \alpha^{-1} + \Delta_3 \end{aligned}\right\}. \tag{3.40}$$

Similar analysis allows us to calculate E_2^V in other cases.

Figure 3.10 separately presents the field dependences of the normalized magnitude $|E|/\omega u$ for each contribution. The parameters for the calculation are the same as in Fig.3.9. For all cases, $|E^{(L)}|$ or $|E^{(M)}|$ shows a larger magnitude than $|E^{(MS1)}|$ or $|E^{(MS2)}|$ especially in the lower field region, and all of them get closer as the field increases. But, considering $B_0 \sim M_0 < M_s$ and e_{33}, $e_{15} >> M_s$ for steels (Berlincourt et al, 1964; Wilbrand, 1983), the contributions of the magnetostriction mechanism will be considerably larger than other two. Focusing on the magnetostriction contributions, we observe that the receiving efficiency is larger for the normal field case than for the tangential field like the generation efficiency, and that the shear wave is more effectively detected than the longitudinal wave.

The quantitative calculation for the field dependence of the receiving efficiency needs the dynamic response of e to the bias field. Unlike the magnetostriction constants, the response of the piezomagnetic constants are not easily estimated from the experimental data, because it is difficult to measure the magnetic induction due to a deformation in a static field. Furthermore, the dynamic response of the induction caused by the small deformation due to the elastic waves will not be measurable. In this situation, the magnetostriction data in Fig.3.6(b), which is useful for calculating the generation efficiency, is still used to estimate e_{15} and e_{33} in following discussion.

Consider the situation that the external field H_{03} is applied to the x_3 direction and the strain ε^u_{33} is introduced by the longitudinal wave. The total strain along the x_3 direction becomes $\varepsilon_{MS}(H_{03}) + \varepsilon^u_{33}$, where $\varepsilon_{MS}(H)$ is the magnetostriction along the total field. This is equivalent to the situation that the perturbation field H_3 occurs in the x_3 direction and the magnetostriction is changed to $\varepsilon_{MS}(H_0 + H_3)$ without the elastic wave. If H_3 is small enough compared with H_{03}, we have $\varepsilon^u_{33} = \partial\varepsilon_{33}/\partial H_3$, and then

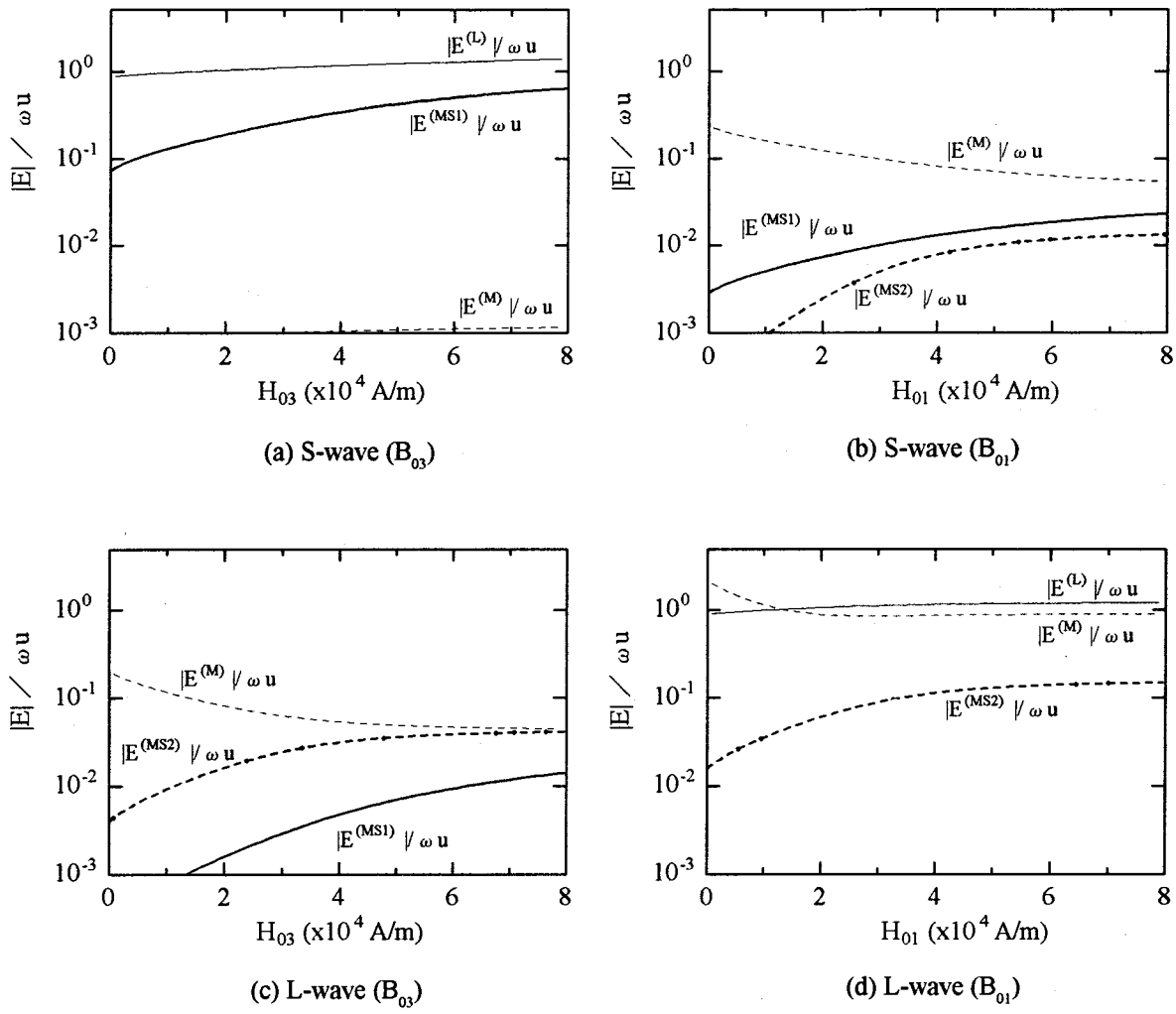

Figure 3.10 Field dependences of the normalized coefficients |E| for each cases.

$$e_{33} = \mu_0\mu_{33}\left(\frac{\partial\varepsilon_{33}}{\partial H_3}\right)^{-1} = \mu_0\mu_{33}\kappa^{-1} \quad . \tag{3.41}$$

Next, consider the shear strain ε^u_{13} caused by the elastic wave. This is again equivalent to the situation without the elastic deformation that the perturbation filed H_1 occurs normal to the bias field and the principal coordinate system rotates from the original. The strain due to the magnetostriction in the principal coordinate system will be $\varepsilon'_{33}=\varepsilon_{MS}(H')$ and $\varepsilon'_{11}=-\varepsilon'_{33}/2$, where $H'=\sqrt{H_{03}^2+H_1^2}$. In the original coordinate system, the shear strain is expressed by $\varepsilon_{13}=(\varepsilon'_{11}-\varepsilon'_{33})\cos\theta\sin\theta$, where $\theta=\tan^{-1}(H_1/H_{03})$. Assuming $\varepsilon^u_{13}=\varepsilon_{13}$, we derive

$$\varepsilon^u_{13} = -\frac{3}{2}\varepsilon_{MS}(H')\sin\theta\cos\theta. \tag{3.42}$$

By differentiating Eq.(3.42) with respect to ε^u_{13} and assuming H_1 to be small enough,

we have

$$e_{15} = -\mu_0 \mu_{11} \frac{2}{3} \frac{H_{03}}{\varepsilon_{MS}(H_{03})} \quad . \tag{3.43}$$

Equations (3.41) and (3.43) allow us to calculate the field dependence of the receiving efficiency on the basis of Eq.(3.38).

3.4.4. Efficiency of the bulk-wave EMAT

The product of the generation efficiency (u/I_0) from Eq.(3.30) and receiving efficiency (E_2/u) from Eq.(3.38) provides the field dependence of the total transduction efficiency with the EMAT. Figure 3.11 shows the transduction efficiencies of the four cases, which are normalized by the efficiency of the shear wave at the normal bias field of 1.5 tesla. These results can be compared with the measurements in Fig.3.5. Although there are some discrepancies, the general features (i)-(iv) observed in Fig.3.5 are well explained by the present model. The efficiency of the longitudinal wave for the tangential bias field (Fig.3.11(b)) is not comparable with the measurement in Fig.3.5 in the lower field region. This will be attributed to the rough estimation of the piezomagnetic constants.

Figure 3.11 provides an acceptable explantation for the unsolved behavior with the bulk-wave EMAT, that is much smaller transduction efficiency of the longitudinal wave and its dependence on the sample thickness (Fig.3.1). The efficiencies for the longitudinal wave for both bias fields are quite small compared to that of the shear wave for the normal field case, especially in the lower field region, indicating that the longitudinal wave is hardly detected. The efficiency, however, increases with the bias field. For a thick plate, the field is not strong enough because of the larger volume of the material to be magnetized and the shear wave are considerably larger; while for a thinner plate, the magnetic field is forced to concentrate within the thin thickness, resulting in the higher field, and then the longitudinal wave becomes larger to be detected.

Concluding that the magnetostrictive effect dominates the bulk-wave generation in ferromagnetic metals, the operation of the bulk-wave EMAT should be illustrated as shown in Figure 3.12 instead of the Lorentz force case in Fig.2.2(a). The shear deformation arises along the total field of the bias field and the dynamic one, and it rotates about the normal direction at the same rate of the dynamic field rotation. This mechanism will generate the shear waves propagating normal to the surface.

3.5. Conclusion

The coupling mechanism between the bulk waves and the electromagnetic field has been discussed, experimentally and theoretically. The EMAR technique made it

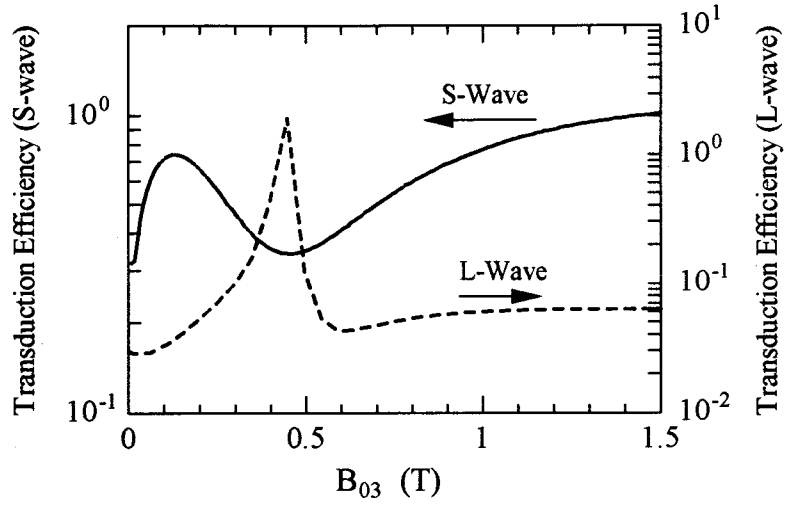

(a) normal bias field

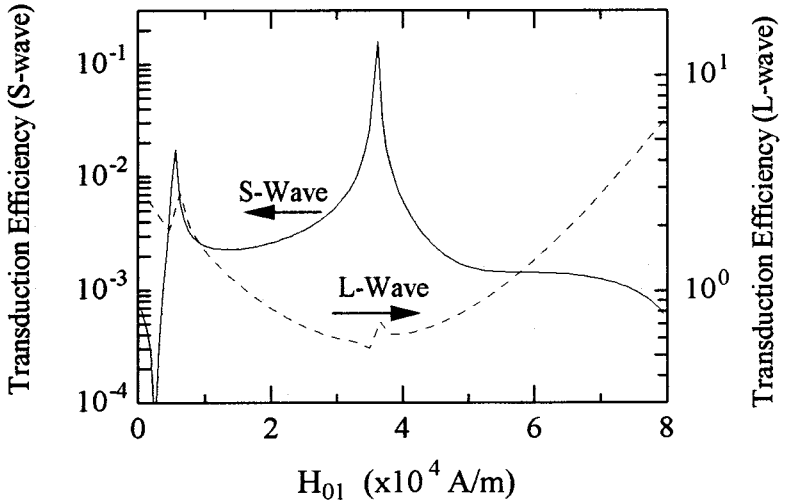

(b) tangential bias field

Figure 3.11 Calculation of the field dependence of the bulk-waves generated and then detected by the EMAT.

possible to measure the field dependence of the bulk-wave amplitudes in a thin plate by means of the resonant peaks, which would not be realized with the conventional pulse-echo technique because of the overlapping of echoes. The experiments showed different features of coupling, depending on the direction of the bias fields and the wave modes.

A theoretical model was presented to explain the complex field dependences in the carbon steel, in which the derivation of the magnetostriction and piezomagnetic constants have been improved from the previous work. The inclination of the total field due to the dynamic one is taken account in the present model and is found to be essential. Using several assumptions, the model successfully explains the field dependencies of the coupling efficiency observed by the experiments.

As a consequence, the magnetostriction effect dominates the coupling phenomena

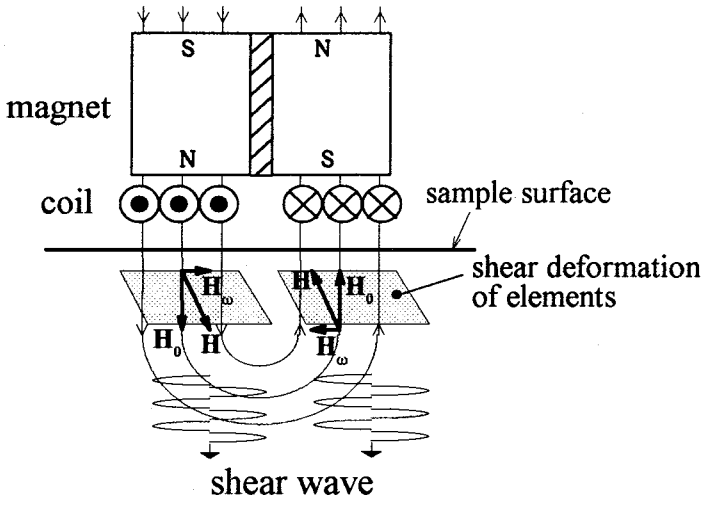

Figure 3.12 Shear wave generation in the thickness direction by the magnetostrictive effect.

both for the normal and tangential bias fields to the surface for ferromagnetic metals. The efficiency of the shear wave generation and detection for the normal bias is considerably larger than other cases, and that of the longitudinal wave is fairly small. This will be an explanation of the unsolved behavior of the bulk-wave EMAT. This knowledge will helps us to develop new types of EMATs in the future.

On the other hand, the model analysis uses the simplifying assumptions on the magnetic properties, which need the further investigation for even accurate analysis. The initial magnetization curve is assumed, but it should be measured with the ring sample, for example. The results in Fig.3.9 is highly affected by the magnetostriction response to the field, but it is not clear that the static property of magnetostriction is useful for analyzing the dynamic response of a ferromagnetic metal. The field dependence of the piezomagnetic constants used in the receiving process were derived from the magnetostriction data, which, strictly, governs the generation efficiency. For the further development of the model, they have to be measured for each test material. A static measurement for them is possible; for example, by preparing a bar sample with small diameter and setting a solenoidal coil to serve the bias field in the axial direction and a smaller coil inside the solenoidal coil for detecting the inductance. Elongation of the bar and measurement of the permeability change will lead to the necessary data for e_{33} in Eq.(3.41).

CHAPTER IV

ACOUSTOELASTIC STRESS MEASUREMENTS

4.1. Introduction

Acoustoelasticity uses the stress dependence of ultrasonic velocities in solid bodies and provides a unique means for nondestructive stress determination (Iwashimizu and Kubomura, 1973; Pao et al., 1984). Time-of-flight measurements for reflection echoes detect the interior stress averaged along the propagation path. While many other techniques are available to evaluate the surface stresses, the alternative to acoustoelasticity is only the neutron diffraction method, which is rarely accessible. Many instances of the successful industrial and field applications are emerging such as those for welded parts, railroad wheels and rails, bolts, and water and gas pipes (Clark et al., 1986; Fukuoka et al., 1978 and 1992; Alers and Manzanares, 1990). However, the wide acceptance of acoustoelasticity as a standard technique has been limited for several reasons. They include the high accuracy needed to cope with the low sensitivity to stress, the prolonged preparation, etc. It needs a high grade of surface finishing to assure the thinnest coupling layer between the piezoelectric transducer and the object surface, thereby achieving the required accuracy of velocity determination. Experimental difficulties arise when the path length is not long enough as will be encountered with the thin-walled structures like aircraft and fuel-storage vessels. Eventually, the successive echoes are overlapped each other even if high-frequency, broadband signals are employed.

The couplant free aspect with EMAR overcomes the experimental difficulties. The velocity response to the stress is replaced by that of the resonant frequency, being feasible for objects with thinner thickness. This Chapter introduces four applications of EMAR to the practical stress evaluation. Their promising results prove that the technique is superior to other traditional methods in the point of usefulness and wider application.

4.2. Acoustoelasticity with resonant frequencies

Acoustoelastic theory establishes the linear dependence of elastic wave velocities on stresses on the basis of nonlinear elasticity, considering up to the third-order elastic constants (Pao et al., 1984). Ultrasonic experiments support the theory with calibrated constants. It is straightforward to convert the acoustoelastic relations in terms of the

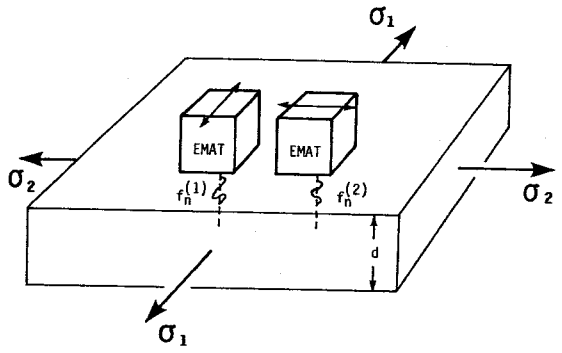

Figure 4.1 Principle of birefringence stress measurement using a polarized shear-wave EMAT.

velocities into those in the resonant frequencies. In the case of a plate sample with the parallel and stress-free surfaces, the acoustic resonance occurs at the frequencies $f_n=nc/2d$ defined in Eq.(2.2). The sensitivity of the resonant frequency to stress increases as n increases.

The thickness can be eliminated by considering the ratios of resonant frequencies. Fractional velocity difference of shear waves having the polarization directions in the principal directions of stress, called acoustic birefringence B, is written as (Iwashimizu and Kubomura, 1973; Pao et al., 1984; Hirao et al., 1993b)

$$B = \frac{f_n^{(1)} - f_n^{(2)}}{(f_n^{(1)} + f_n^{(2)})/2} = B_0 + C_A(\sigma_1 - \sigma_2) \ , \tag{4.1}$$

where $f_n^{(1)}$ and $f_n^{(2)}$ are the nth resonant frequencies for the polarization in the principal stresses σ_1 and σ_2 (Fig.4.1). The ratio of longitudinal wave velocity to the average of two shear wave velocities, denoted by R, is proportional to the sum of the principal stresses. This is expressed in the term of the resonant frequencies including $f_m^{(3)}$ for a longitudinal mode as

$$R = \frac{n}{m}\frac{f_m^{(3)}}{(f_n^{(1)} + f_n^{(2)})/2} = R_0 + C_R(\sigma_1 + \sigma_2) \ . \tag{4.2}$$

The acoustoelastic constants C_A and C_R represent the sensitivity to stress, depending on the second- and third-order elastic constants. Although they show a weak dependence on material microstructures, it is the usual procedure to calibrate them in uniaxial load-

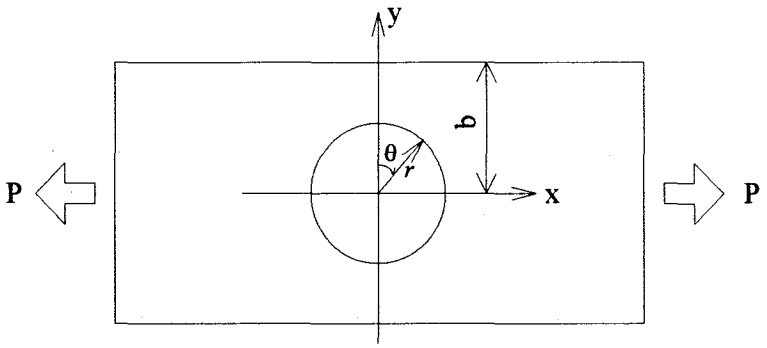

Figure 4.2 Strip with a center hole in the plane-stress state.

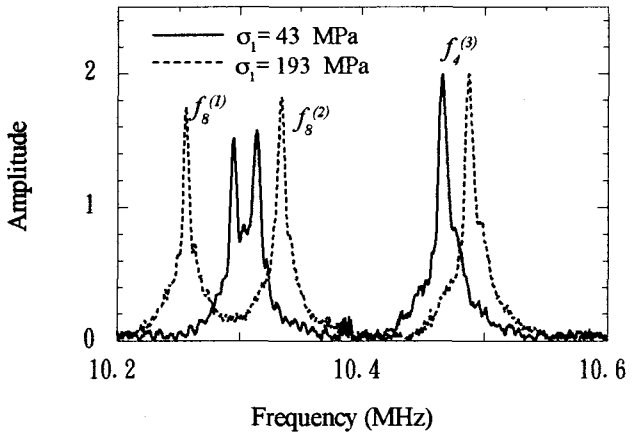

Figure 4.3 Acoustoelastic response of amplitude spectra in a uniaxial loading. Sample is 2017 aluminum alloy of 1.22-mm thick.

ing tests (σ_2=0). The offsets B_0 and R_0 are observed at the stress-free state. When the material has no texture and is macroscopically isotropic, B_0 vanishes and R_0 takes the value of $[(\lambda+2G)/G]^{1/2}$, where λ and G are the second-order elastic constants. When B_0 and R_0 are both accessible in some way, we can determine the individual stresses by measuring B and R.

4.3. Two dimensional stress field in thin plates

First application is the measurement of the two-dimensional stress field in a strip plate with a hole at the center under the tensile load (Fig.4.2). Sample is an aluminum alloy (Al2017) of 1.22-mm thick, 150-mm wide, and 670-mm long. The hole is 45-mm diameter. Non-holed strip of the same material is also used for the calibration test to

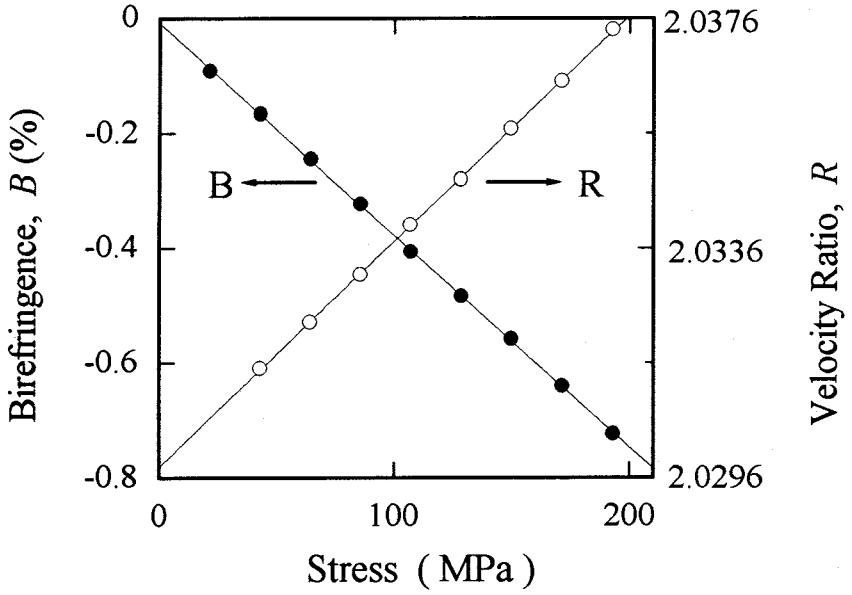

Figure 4.4 Linear dependence of B and R on uniaxial stress σ_1 in 2017 aluminum sample; B_0=0.006% and C_A=-3.69x10^{-5} MP^{-1}; R_0=2.0298 and C_R=3.93x10^{-5} MPa^{-1}.

have the acoustoelastic constants C_A and C_R, and the offset values B_0 and R_0.

Figure 4.3 shows the amplitude spectra at two stresses obtained during the calibration tests. The dual-mode EMAT (Fig.2.2 (b))was used, whose effective area is a circle of 10 mm diameter. It detects two shear resonant frequencies $f_8^{(1)}$ and $f_8^{(2)}$, and the longitudinal component $f_4^{(3)}$ at the same time at the same probing area. The frequency was incremented for the 10.2-10.6 MHz range at 800-Hz steps. The resonant frequencies demonstrate easily detectable changes showing the acoustoelastic phenomena. Two shear-wave peaks for the orthogonal polarizations were superimposed over each other in the absence of stress because of very small texture anisotropy. The stress-induced anisotropy made them separate. Both B and R showed the linear dependence on stress as the theory predicts (Fig.4.4).

A two-dimensional stress field is produced by stretching the strip with the hole (Fig.4.2). Surface preparation was unnecessary. Since B_0 and R_0 were nearly homogeneous over the scanning area, their representative values are used in calculating stresses; the error is estimated to be less than 2.7 MPa. A typical measurement was done with the 500-V rf bursts of 40-μs duration, approximately 50 times the round-trip time, 34 dB for receiver gain after the preamplifier, and the 250-μs long integrator gates. Frequency increment was 600 Hz. For the scanning along the y-axis, the bulk-wave EMAT (5x4 mm^2) was oriented 45° to detect the two shear wave resonant frequencies at the same time, which yields B and depicts the variation of the principal stress difference (σ_{xx}-σ_{yy}). σ_{yy} is smaller than a part of a tenth of σ_{xx}. The stress difference was not large enough to resolve the shear-wave polarization on the x-axis. There-

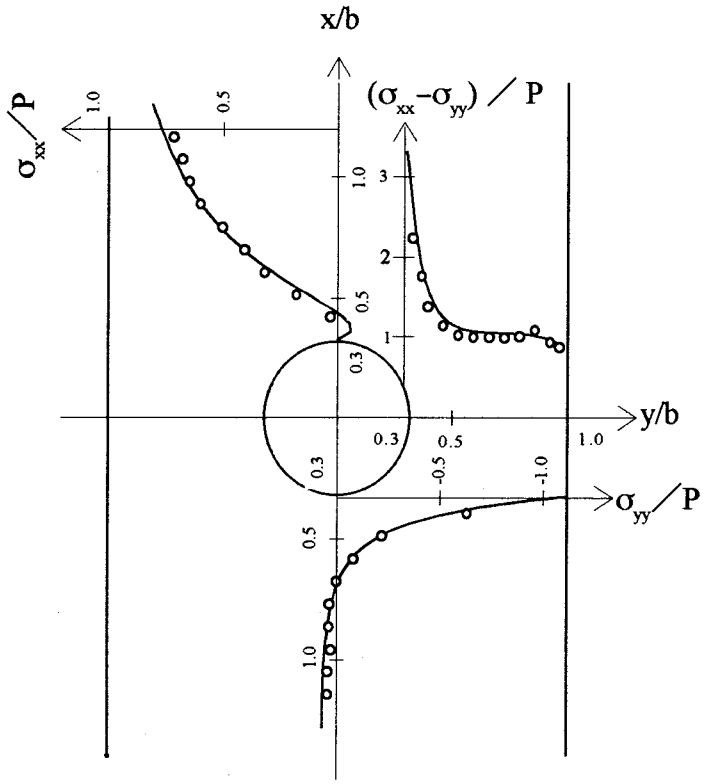

Figure 4.5 Stress around the center hole of stretched strip. Howland's solution is shown in solid curves. Stresses are scaled by the stress at infinity (P = 53.5 MPa) and the coordinate by b, half-width of the strip.

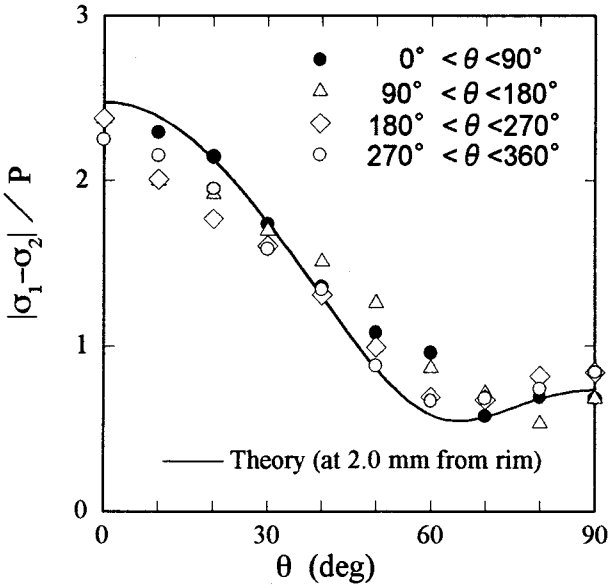

Figure 4.6 Comparison between EMAR measurement and theory along each quarter of the rim (P=53.5 MPa).

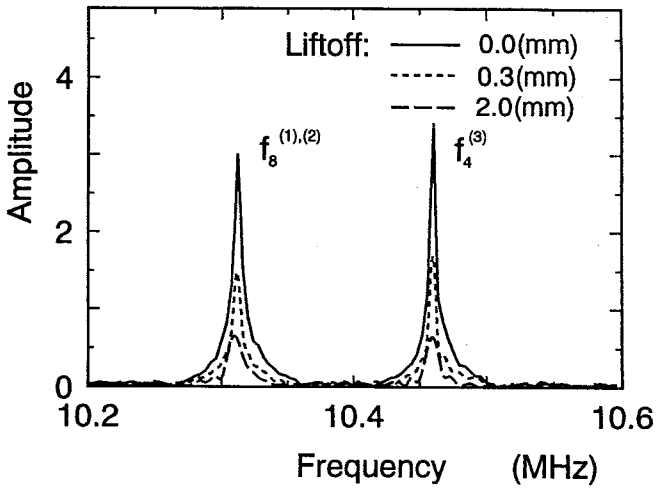

Figure 4.7 Appearance of amplitude spectra as a function of increasing liftoff.

fore, the above EMAT was rotated to 0°/90° to obtain $f_8^{(1)}$ and $f_8^{(2)}$. The longitudinal resonant frequency was measured using the dual-mode EMAT (10-mm diameter). Their combination results in the separate determination of σ_{xx} and σ_{yy}, where the calibrated values of C_A and C_R were used from the uniaxial tests (Fig.4.4). The acoustoelastic measurements are compared with the analytical solution (Howland, 1930) in Fig.4.5, where the averages on both sides of the hole are presented. The local stress field has been averaged over the EMAT aperture. Such a correction was, however, useless except for the proximity of the edges and the rim. The measurements agree with theory within the fluctuation of 5 MPa as a whole. Approaching the edges and the rim, disagreement increases close to 10 MPa. This is attributed to the abrupt variation of stresses within the EMAT's apertures, inclusion of reflections from the lateral boundaries, and the inhomogeneity of B_0 and R_0 which might be introduced when the hole was drilled.

Along the rim, the stress is not acting in the x and y axes and B is related to the principal stresses through a more general formula (Iwashimizu and Kubomura, 1973):

$$B = \frac{f_n^{(1)} - f_n^{(2)}}{(f_n^{(1)} + f_n^{(2)})/2}$$

$$= \sqrt{B_0^2 + 2B_0 C_A(\sigma_1 - \sigma_2)\cos 2\theta + C_A^2(\sigma_1 - \sigma_2)^2}\ , \qquad (4.3)$$

where θ is the angle between the principal direction and the specimen axis. There is only one nonzero principal stress along the rim. The radial component was included in the theory because the EMATs have the finite aperture and the stress field changes steeply in the vicinity of the hole. Figure 4.6 compares the results of stress measure-

ment using the above bulk-wave EMAT to the theory calculated at 2 mm outside the rim, where the center of the EMAT traced. Disagreement among the quarters could be caused by the slight eccentricity and imperfect roundness of the hole. Maximum error was 15 MPa in this experiment.

To examine another aspect of the applicability, the tolerance to the liftoff has been tested using the same aluminum plate and the 10-mm-diam dual-mode EMAT. The polymer sheets was inserted between the EMAT and the plate to simulate a liftoff. Figure 4.7 shows the observed decrease of the peak heights. The frequency was swept every 4kHz. The input rf voltage was 1500 V and the maximum gain was 46 dB. Resonant frequencies were measurable until the liftoff was 2.67 mm and both $f_8^{(1),(2)}$ and $f_4^{(3)}$ decreased by 0.45% and 0.32%, respectively, relative to those for the zero-liftoff measurements. Changes in B and R are generally one order less than the frequency changes because they are derived from the difference or the ratio of the resonant frequencies, which will be affected by the liftoff with a same rate. The above is the result when the measuring conditions remain unchanged. We detected the resonant peaks up to 5mm liftoff in this particular sample by optimizing the meausring parameters. Use of larger EMATs, more driving input power, and less attenuating materials would allow us to extend the limiting liftoff.

4.4. Axial stress of railroad rails

Installed railroad rails are subjected to abrupt temperature changes because they are exposed to the open air and radiant heat from the sun. They are fixed to the crossties and then temperature changes (typically -10°C to 60°C in Japan) create axial stresses in the rails through the constraint to the thermal expansion/contraction. During winter nights, the thermally induced tensile stress promotes the growth of fatigue cracks and causes the weldment separation in continuously welded rails. It may also accelerate the development of fretting corrosion in bolt-jointed parts. In early summer, temperature rise can build up sufficient compressive axial stress to start the hazardous track buckling (the lateral movement of the track), which potentially can lead to a derailment accident. Such a buckling can be triggered by the passage of trains, especially in the curved sections.

The axial load assessment is a key issue in railroad maintenance to ensure safe services. Current practice relies on human efforts in Japan and probably in other countries, too. The costs are high and it is highly time/labor-consuming. There has been a great interest in developing a stress-detection device to be available in the regular maintenance. This should be portable and robust in order to cope with on-site environments or it can be implemented in a test car moving at standard speeds. A noncontacting sensor is required for the nondestructive stress evaluation. Other requirements include quick and easy measurement and, more importantly, enough

stress resolution that is not affected by the actual measuring conditions (service period, track curvature, temperature, surface contaminations, operator, etc.). Several researchers have tried to develop the technique, which includes the magnetic properties (Kashiwaya et al., 1985) and acoustoelastic stress measurement with an EMAT (Egle and Bray, 1978; Alers and Manzanares, 1990; Schramm et al., 1993; Deputat et al., 1993). With the magnetic method, difficulties arise from the nonlinear response of the magnetic properties to the stress, depending on the microstructure. For the acoustoelastic methods, the weak coupling efficiency of EMATs continues to pose a problem.

In the present Chapter, the EMAR method relying on the birefringent acoustoelasticity (Eq.(4.1)) is applied for the noncontacting measurement of axial stress in Sinkansen railroad rails. The birefringence B is obtained from the difference of two shear-wave resonant frequencies, which is free from the thickness and can decrease the influences of the change in temperature and liftoff, because these effects shift the resonant frequencies with a same rate and can be removed by taking the difference. However, the measurement includes the offset B_0. The thermomechanical history during the manufacturing process gives rise to the texture variation, which alters the magnitude of B_0 from the 10^{-2} order to zero. This situation indicates the difficulty of determining the residual stresses unless an appropriate estimate can be made somehow for B_0 (Fukuoka et al., 1978 and 1983). Ignorance of 0.1% initial anisotropy results in more than 100-MPa error of the stress measurement. This is a disadvantage inherent in the birefringent acoustic stress measurement. As for the applied stresses, B_0 is accessible in advance precisely in the same procedure and at the same sites that the acoustoelastic measurement is made.

In the experiment, two samples of the same geometry were used. One was the rail whose head was slack quenched to give a deep hardened area (denoted here as DHH), which was used to study the acoustoelastic response to the compressive axial load. The other was the standard as-rolled rail (denoted as STD). The distribution of B_0, attributable to texture and residual stress, was measured on this sample. Both are 0.5-m long and have the cross sections shown in Fig.4.8. They were normally rusted, but the surface preparation was not necessary at all. A shear-wave EMAT, which has an effective area of 14x20 mm^2, was attached on the web of the rails for getting the birefringent. The frequency was swept in the range of 3.79-3.88 MHz at 600-Hz steps, and the *40*th resonant peak was detected.

The test was performed for the DHH rail by giving an axial load up to 60 tons, at which a usual long rail is considered to cause a buckling. Figure 4.9 shows a view of the measurement in laboratory. Seven strain gates were attached around the rail to watch the balanced loading. Figure 4.10 presents the spectrum response for the polarized shear wave along the axial direction ($f_{40}^{(1)}$). The birefringence response to the stress is shown in Fig.4.11. The good linearity concludes the evaluation within 3-MPa error band.

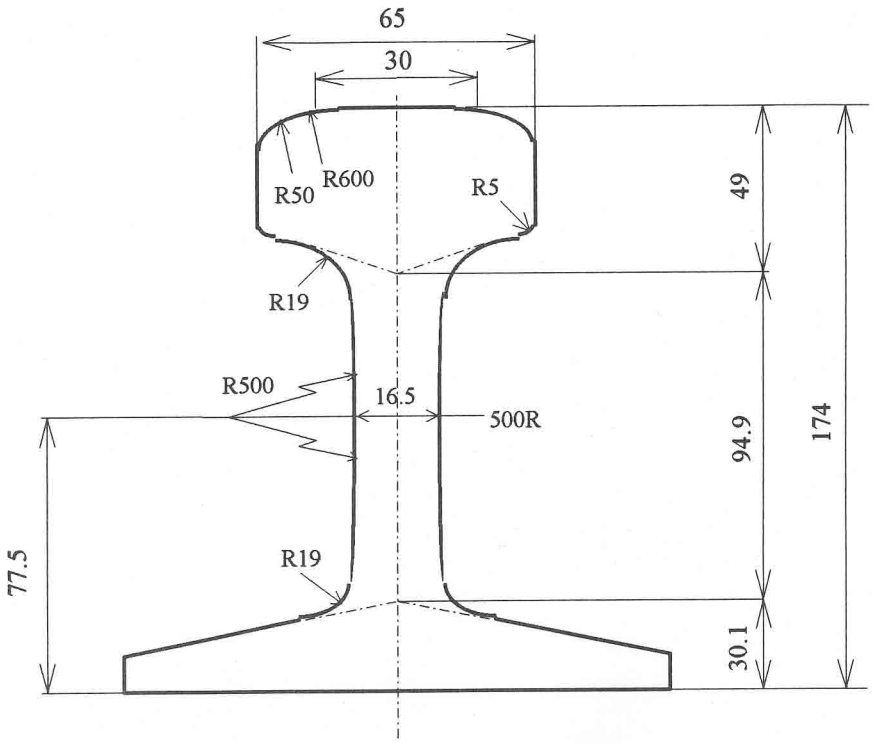

Figure 4.8 Dimensions of JIS-60 rail cross section.

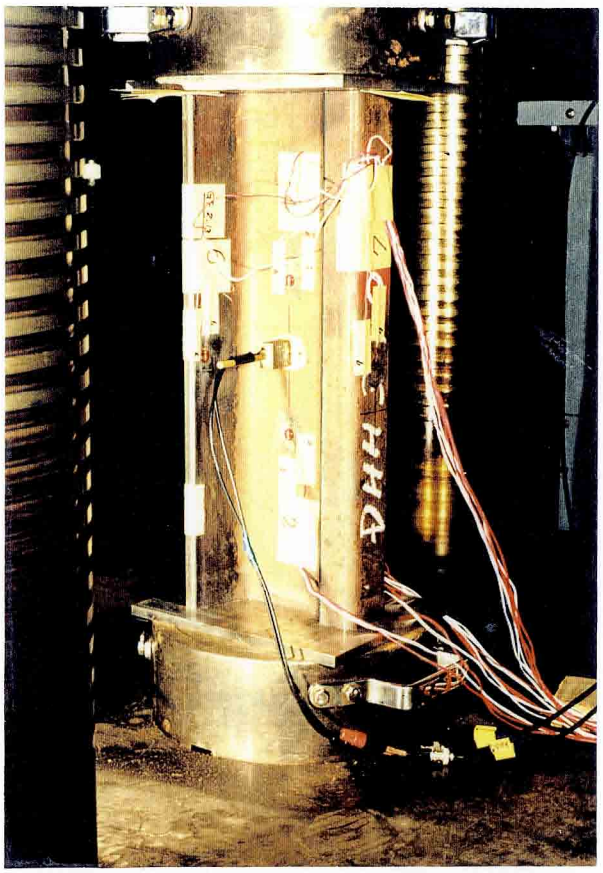

Figure 4.9 EMAR measurement on railroad rail.

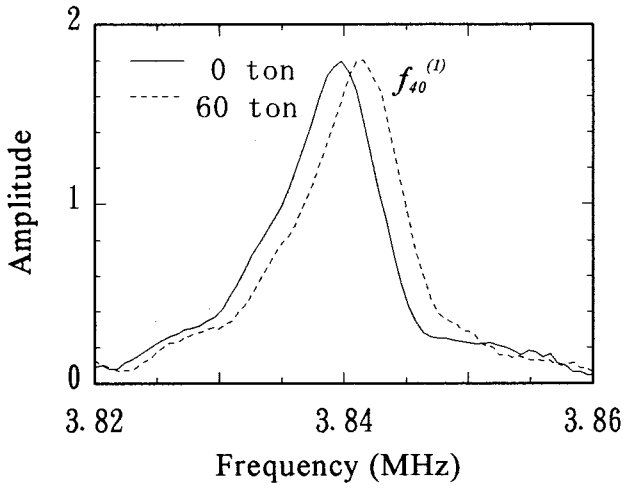

Figure 4.10 Acoustoelastic response of resonant spectrum at the rail web, showing the *40*th shear mode in the parallel polarization to axial stress.

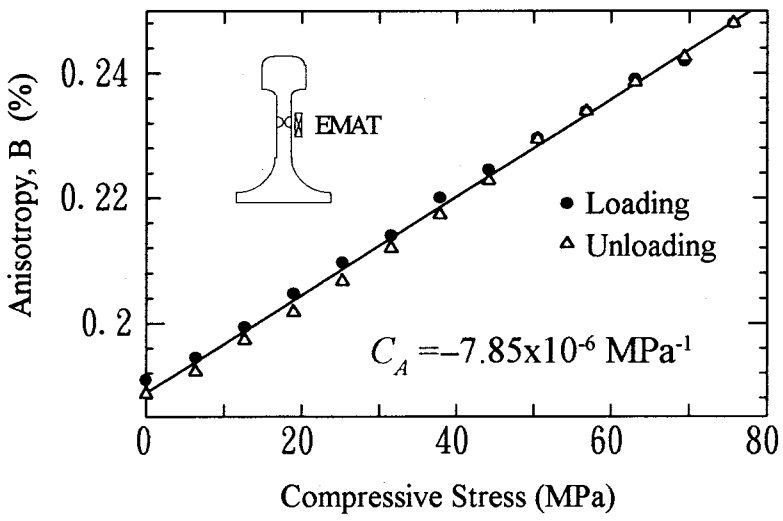

Figure 4.11 Relation between resonant birefringence at the web and axial compressive stress; C_A=–7.85x10^{-6} MPa^{-1} and B_0=0.189%.

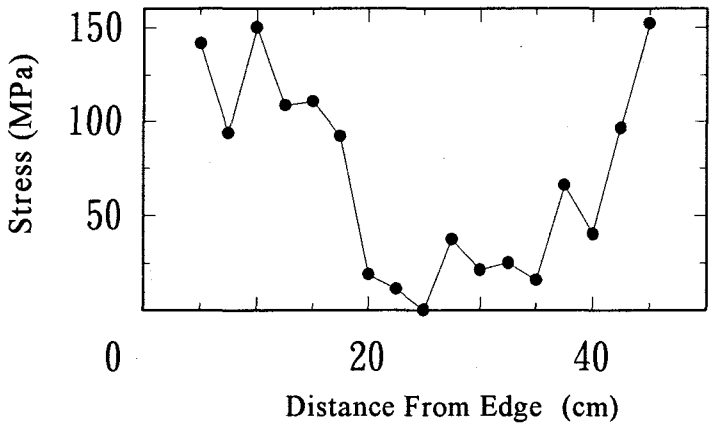

Figure 4.12 Inhomogeneity of B_0 at the web along the rail.

The birefringent values without any external loading were measured at 25-mm steps along the STD rail. The initial anisotropy B_0 was found considerably inhomogeneous along the length. The results are shown in Fig.4.12, where the deviations relative to the midpoint (25 cm) measurement are divided by C_A to have equivalent values in stress. The nearly symmetric variation on the web implies that a large compressive residual stress (~150 MPa) was present in the original full-length rail and it persisted in the middle part of the short sample. The texture is considered to be uniform along the rolling lines. This stress evaluation agrees with the destructive measurement with strain gages on the same type of rail (Urashima et al., 1992). The larger cooling rate at the web because of smaller thickness, produces a compressive residual stress there and, for balance, produces tensile stresses in the head and the base.

The liftoff effect was also studied for the STD rail. The measurement showed that the liftoff up to 1.0 mm may cause the evaluation error within 10MPa (Hirao et al., 1994a).

The results presented here are just on laboratory evaluation. Further work on longer rails will determine the influence of the initial anisotropy B_0. In the worst possible case, B_0 varies from point to point, and therefore it should be measured at every scanning point along the rail before the axial stress is generated.

4.5. Residual stress in weldments

The third application is the evaluation of the residual stress profiles in welded steel plates and pipes, again being based on the birefringent acoustoelasticity. The intrinsic birefringence due to the texture is estimated from the measurement close to the free ends, where the stress is considered to be absent. A bulk-wave EMAT is used to generate and detect the shear waves propagating normal to the sample surfaces. The

effective area is 5x3mm^2. The details of samples are shown in Figs. 4.13 and 4.14. The materials are low carbon steels. Plasma beam has been used for cutting out the samples. The birefringences along *Line1* and *Line2* are measured to have the stress differences (σ_1-σ_2) for the plate and (σ_θ-σ_z) for the pipe, by moving and rotating the EMAT manually. Although the samples have rough surfaces (R_a =6.5~7.2μm), all measurements have been performed without any surface preparation.

The *51*th resonant frequencies are used for both shear waves. With the assumption of the acoustoelastic constant C_A to be -7.8x10^{-6} MPa^{-1}, which is plausible for steels, and the offset B_0 determined from the birefringence far away from the welding line, the difference of principal stresses is calculated. Figures 4.15 and 4.16 give the stress distributions along *Line1* and *Line2*. To verify the results, strain gauges are mounted at several points along *Line1* on the front and back surfaces of the plate sample and the residual strain is obtained by cutting the samples in small pieces to release the residual stresses. Figure 4.17 compares the distribution along *Line1* measured by the EMAR method and the strain gage method. In the figure, the re-calculated stresses are also plotted, which is derived using B_0 measured at each point after releasing the stresses. The larger stresses in the EMAR method with the assumed B_0 are caused by unfavorable assumption of B_0 at the edge of the plate. Even near the edge portion, there exists the residual stresses, which would have been introduced by the high temperature due to the plasma cutting. From the strain gauge results, we notice the stress gradient in the depth direction, which may cause a discrepancy with the EMAR results since it is sensitive to the average stress over the thickness. Near the center region, the front surface has greater stress about 60 MPa than the back surface, while the relationship is reversed as the distance from the center increases. The ultra-

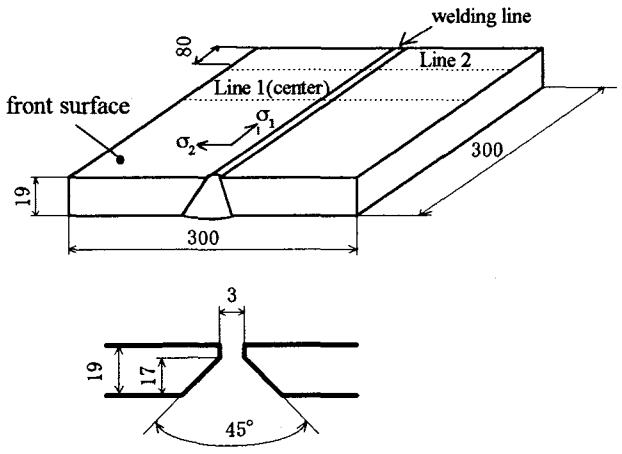

Figure 4.13 Geometry of butt-welded plates

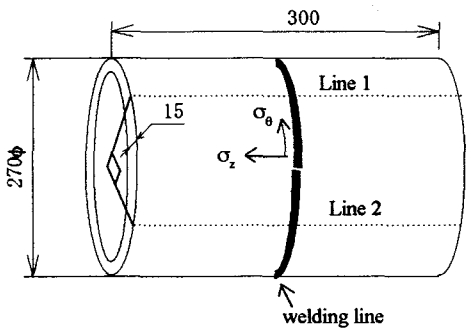

Figure 4.14 Geometry of welded pipes.

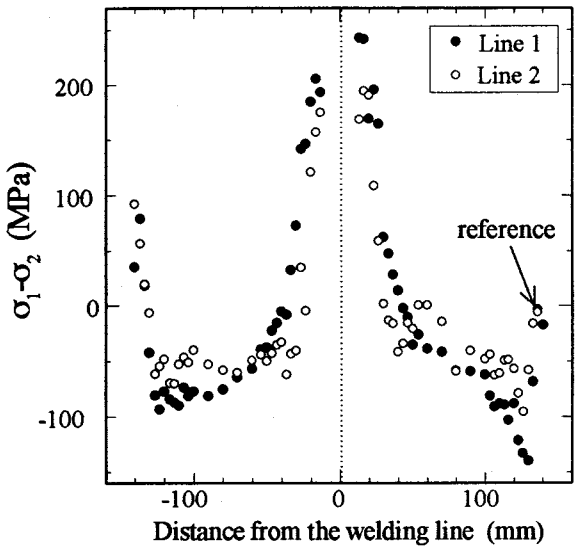

Figure 4.15 Residual stress distributions of the welded steel plates measured with the EMAR method.

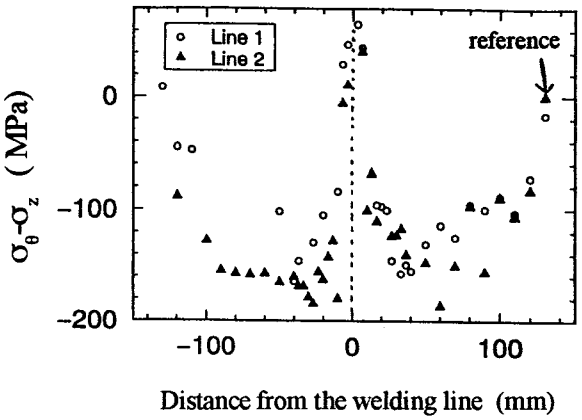

Figure 4.16 Residual stress distributions of the welded steel pipes measured with the EMAR method.

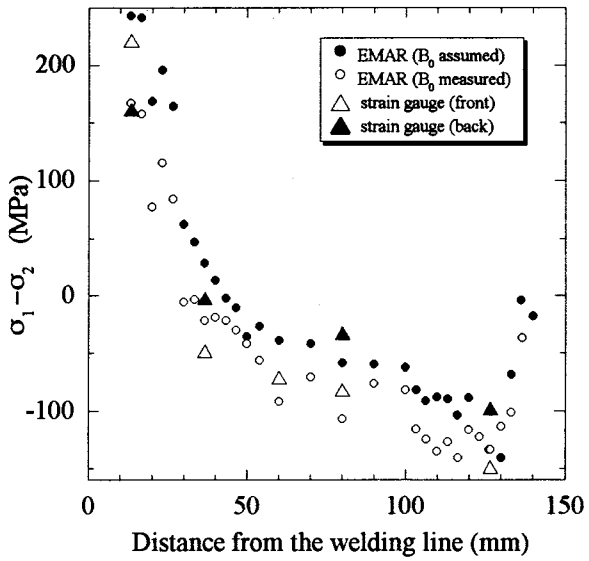

Figure 4.17 Comparison of the EMAR method and the strain gauge method for the welded plates. The solid and open circles denote the data by the EMAR with the assumed B_0, (same as the solid circle in Fig.4.15) and the measured B_0, respectively. The triangles are the strain gauge results.

sonic method is incapable of detecting these gradients.

As a whole, the stresses evaluated by the EMAR with the assumed value for B_0, showed agreements with the strain gauge technique within 10-40 MPa. The comparison with the strain gauges will get worse when the stress gradient to the thickness direction is steeper.

4.6. Bending stress in gas pipes

The electric resistance welded (ERW) pipes are widely used as the gas pipe line. They are usually constructed underground and often suffer from the large bending stress due to earthquake and uneven settlement. The nondestructive stress measurement is therefore needed to ensure their safety.

In this section, the bulk-wave EMAT is again used, whose active area is 7x6 mm^2. The steel pipes were bent in a four-point bending configuration. The bending stress is evaluated by moving the EMAT in the circumferential direction around the outer surface of the central part of the bent pipe. The shear-wave birefringence is obtained from the normalized difference of the resonance frequencies of the shear waves polarized in the axial and circumferential directions.

In the case of four point bending of a pipe, only the axial stress (σ_z) exists at the center part, which is equal to $\sigma_{max}\cos\theta$, where $\sigma_{max}(>0)$ is the maximum bending stress and θ stands for the angle from the vertical direction as shown in Fig.4.18. It is obvious that the acoustic birefringence B can be determined from the resonant frequencies as

$$B(\theta) \equiv \frac{f_n^{(z)} - f_n^{(\theta)}}{(f_n^{(z)} + f_n^{(\theta)})/2} = B_0 + C_A \sigma_{max} \cos\theta \ , \tag{4.4}$$

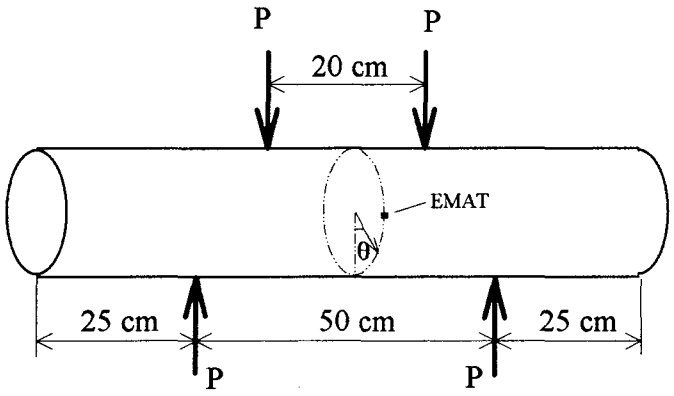

Figure 4.18 Four point bending configuration.

where $f_n^{(z)}$ and $f_n^{(\theta)}$ are the nth resonant frequencies of the shear waves polarized in the axial and the circumferential directions, respectively. Unlike the previous applications, maximum bending stress σ_{max} is obtained without knowing B_0 by measuring B around the circumference and fitting Eq.(4.4) to them.

The evaluation has been performed for two ERW pipes with different dimensions, one of 75-mm outer diameter and 2.3-mm thick (JIS-STKM13B: *Pipe 1*), and the other of 101.6-mm outer diameter and 2.8-mm thick (JIS-SAE1020: *Pipe 2*). Both are 1-m long. The setup of the bending test is sketched in Fig.4.18. The loads P are set to 1 ton for *Pipe 1* and 1.5 ton for *Pipe 2*. Four strain gauges are symmetrically attached on the outer surface every 90° interval along the circumference with 10-mm distance away from the center, at which the bending stresses of the axial direction are monitored. Although the samples have been painted, the measurements are performed with no surface preparation. In spite of the curvature, the sharp resonant spectra are observed and the resonant frequencies near 6.3 MHz for *Pipe 1* and 5.3 MHz for *Pipe 2* are used. As the order of the resonant mode becomes higher, its sensitivity to the stress is enhanced. Then, the highest possible resonant frequency has been selected for the stress measurements. The attenuation in *Pipe 2* was larger than that of *Pipe 1*, which would be attributed to larger grain size of *Pipe 2*, resulting in the use of lower resonant frequency.

Figure 4.19 plots the measured variation of B with θ. The fitting cosine curves are also included. By assuming C_A=−8.0x10^{-6} MPa^{-1}, we have the maximum bending stresses of 188 MPa for *Pipe 1* and 73 MPa for *Pipe2* through the amplitudes of the

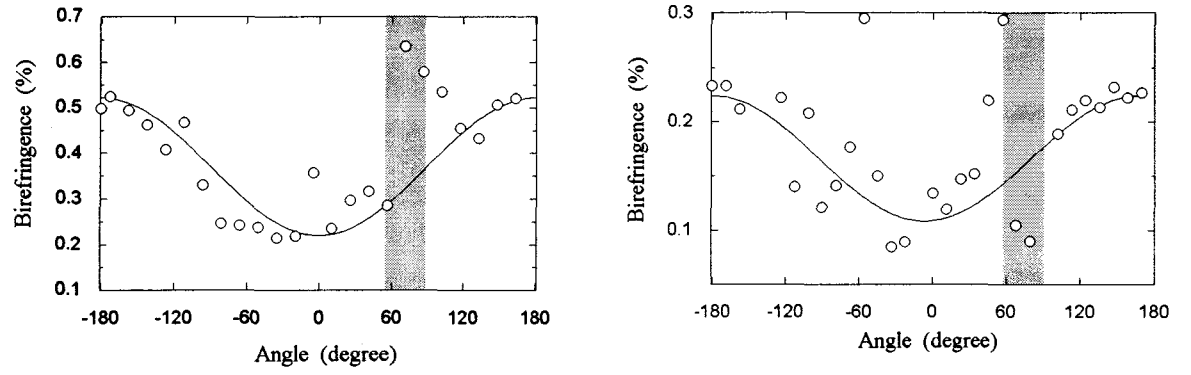

(a) Pipe 1 ($\sigma_{max}^{(gauge)}$=177MPa, $\sigma_{max}^{(EMAR)}$=188MPa) (b) Pipe 2 ($\sigma_{max}^{(gauge)}$=109MPa, $\sigma_{max}^{(EMAR)}$=73MPa)

Figure 4.19 Measurements of birefringence around circumferences of the pipes. $\sigma_{max}^{(gauge)}$ and $\sigma_{max}^{(EMAR)}$ are the maximum bending stresses obtained by the strain gauge and the EMAR methods, respectively. The gray bands express the heat affected zones along welding lines.

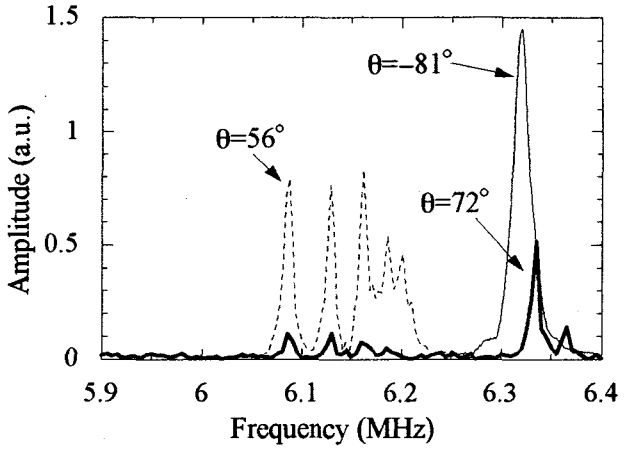

Figure 4.20 EMAR spectra around $f_9^{(z)}$ observed in *Pipe 1*.

fitted cosine curve. The strain gauge method gave the stresses of 177 MPa for *Pipe 1* and 73 MPa for *Pipe 2*, which favorably compares with the EMAR measurements. On and close to the welding lines, the resonant peaks shifted to the very low frequency regions and the spectra contained several peaks as shown in Fig.4.20, which are responsible for the microstructural changes of material and the thickness variation along the welding line. Therefore, the fitting calculation excluded the data of these region. The data scattering also occur due to the distribution of B_0 around the circumference. In the present case, B_0 corresponds to the birefringence without the loading, and it includes the influence of residual stresses. Generally, there are residual stresses in the ERW pipe because of roll forming and welding during the manufacture process, and they have large influences on the B_0 value. But, using many data of B around the circumference and fitting the cosine curve to them serves to smooth out the scattering of B_0 and minimize the influence of nonuniform B_0.

4.7. Conclusion

The EMAR has been proven to permit the practical acoustoelastic stress measurements, showing the remarkable frequency and spatial resolution. The measurement is available not only for plates with parallel surfaces but also for samples with curvature such as the web portion of rail and the ERW pipes. The stresses evaluated with EMAR agreed with those from theory and the strain-gauge method to the accuracy of 5-40 MPa. Although the inherent problem of the birefringent acoustoelasticity with the offset values is still unsolved, the accuracy of the measurement has been improved considerably and also the difficulties with the conventional contacting methods have been

removed with the noncontacting aspect of the EMAR. Some cases allows us to estimate the unknown offset values from the edge portion of a sample where the stress is supposed to be absent. In other cases, the measurement don't need them because of the axial-symmetric distribution of the acoustoelastic birefringence like the pure bending stress in a pipe. The measurable thickness range from 0.1 to 50 mm, mainly depending on attenuation in the material, not on the surface quality nor the curvature of surface. The birefringence measurement is insensitive to temperature and the thickness because the difference between the resonant frequencies for the two polarizations is only considered. The future work includes the more practical applications not in the laboratory but in the field to examine the other effects, such as the electromagnetic noise, as well as developing the texture-independent stress determination with the SH-wave EMATs (Alers and Manzanares, 1990).

CHAPTER V

ABSOLUTE MEASUREMENT OF ULTRASONIC ATTENUATION

5.1 Introduction

The accurate measurement of ultrasonic attenuation is very important, because it has a great utility in the wide area of materials characterization (Beyer and Letcher, 1969; Goebbels, 1980; MacDonald, 1977; Ritchie and Fantozzi, 1992). Only ultrasonic attenuation is available for the study of the dislocation mobility in a metal during deformation and the evaluation of three-dimensional grain size of a polycrystalline metal. The importance of attenuation for detecting the materials character has been well known but the difficulty of the measurement has limited its acceptance as a general technique. This Chapter presents a new idea of the attenuation measurement, which relies on the relaxation of the ultrasonic resonance. Use of a noncontacting or weakly coupling EMAT for the attenuation measurement has a pronounced advantage of eliminating the extra energy losses, which otherwise occur with the conventional contacting or immersion tests based on the piezoelectric transducers.

In the attenuation measurement using a contacting transducer, with well finished sample surfaces, the ultrasonic beam loses its energy due not only to attenuation in the sample (absorption and scattering) but also to the following four factors; (i) damping through the transducer, the couplant, and the buffer, if any, (ii) the reflection and transmission losses at the interfaces, (iii) the energy leakage into the transducer on reception, and (iv) the beam spreading (diffraction). Being interested only in attenuation in the sample, we must remove factors (i) to (iv) from the as-measured attenuation by proper correcting procedures. Diffraction effects can be eliminated by the familiar formula in pulse-echo measurements (Seki et al., 1955; McSkimin, 1960; Papadakis, 1966), while the correction for factors (i)-(iii) has not been successful so far in reality, because the acoustic parameters of all the components involved have to be determined *a priori*. It is not practical to know, for example, the thickness and the acoustic velocity of the couplant, which depend on the temperature, the applied pressure, the surface condition, etc.

The measurement with an EMAT is inherently free from losses associated with the interfaces because of the noncontacting coupling, so that the energy loss arises only from attenuation through the sample, the diffraction effect, and additionally the electromagnetic loss. The electromagnetic loss occurs when the elastic wave travels through the magnetic field and induces the eddy currents, but the amount will be shown

negligible compared with the attenuation. The diffraction effect is excluded through a correcting algorithm at a resonance. It is then possible to evaluate an absolute value of ultrasonic attenuation based on the EMAR. Furthermore, involving a larger number of echoes in the resonance, unlike a couple of distinct echoes in the pulse-echo experiments, contributes to improve the accuracy and the reproducibility to a marked extent. A measurement finishes in a very short time without any preparation on the sample surfaces. The bulk-wave EMATs are used to measure the shear wave attenuation throughout in this Chapter.

5.2. Isolation of ultrasonic attenuation

When an EMAT is used, an observed attenuation coefficient α_m consists of attenuation in the sample (α) we require, the diffraction loss (α_d), and the electromagnetic loss (α_e); that is (Ogi et al., 1995a)

$$\alpha_m = \alpha + \alpha_d + \alpha_e . \tag{5.1}$$

The electromagnetic loss occurs when the ultrasonic travels through the static magnetic field and the inverse Lorentz force mechanism gives rise to the eddy currents in the material. A part of these eddy currents is picked up by the coil in the EMAT to give a received signal. The quantitative expression for α_e becomes

$$\alpha_e = \frac{\sigma B_a^2}{2\rho}, \tag{5.2}$$

where σ is the electrical conductivity of the sample material, B_a the average static magnetic flux density through thickness of the sample applied by the permanent magnets, and ρ the mass density. Taking up a steel, for example, where B_a=1 T, σ=3.0x10^6 S/m and ρ=7900 kg/m^3, we have α_e=2x10^{-4} μs^{-1}; while α is larger than 10^{-3} μs^{-1} in most steels for frequencies beyond 1 MHz (Hirao and Ogi, 1994c). This leads to the estimation that α_e/α<0.2%. Then, α_e is neglected henceforth in this thesis. But, α_e has to be taken into account for a material with a high conductivity, for a strong magnetic field, and/or for extremely low attenuating materials.

An isolation of α proceeds in three steps. First, a resonant frequency is measured. Secondly, the relaxation time coefficients is determined at the measured resonant frequency. Finally, the diffraction effect is corrected by an iterative process.

5.3. Measurement of relaxation time coefficient

Resonant frequencies are easily measured by activating the EMAT with long, high-power rf bursts gated coherently, sweeping the operation frequency, and acquiring the amplitude spectrum. The input rf burst is much longer than the round-trip time

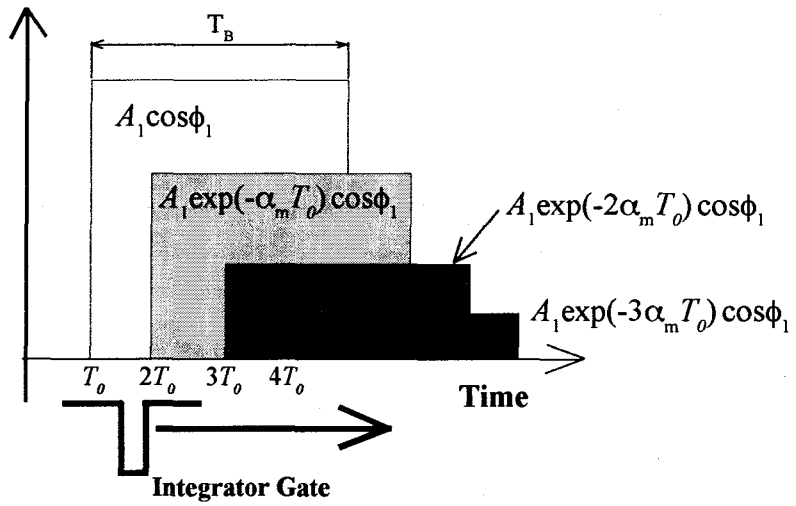

Figure 5.1 Time response of coherent signals at a resonance after the superheterodyne processing (in-phase components). A_1 is the amplitude of the first echo and ϕ_1 is its phase shift. T_0 is the round-trip time in the sample and T_B the width of the input rf burst.

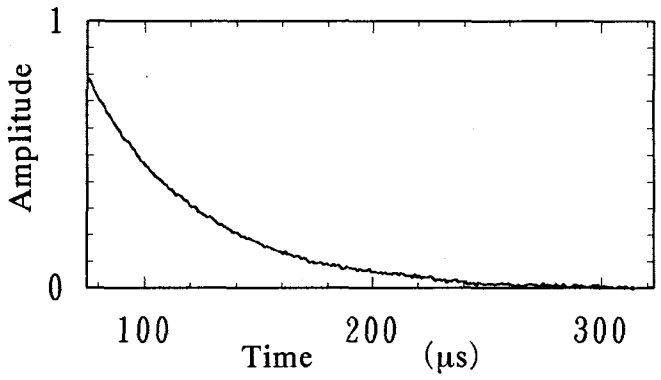

Figure 5.2 Measured ringdown curve with a low carbon steel sample (6 mm thick) at the *10*th resonant frequency (around 2 MHz).

in the sample plate. Amplitude spectrum is calculated from the in-phase and quadrature outputs of overlapped echoes (reverberation) after the analog superheterodyne processing. We then bring the sample plate into the ultrasonic resonance by driving the EMAT with the measured resonant frequency. At a resonance, all echoes reflected at the sample surfaces become coherent; that is, the echoes have a constant phase regardless of the echo number, i, giving a productive interference among them. In this case, the in-phase integrator outputs ($\Sigma A_i \cos\phi_i$) decay exponentially with time, depending on the time coefficient α_m as illustrated in Fig.5.1. The outputs of quadrature components ($\Sigma A_i \sin\phi_i$) also decay with α_m, but with much less amplitude.

The ringdown curve is measurable by sweeping a short integrator gate (instead of a long one for obtaining the spectra) along the time axis, integrating both the in-phase and out-of-phase outputs, and calculating the root of the sum of their squares. Figure 5.2 presents an example of the measured ringdown curve for a 6-mm thick carbon steel at the *10*th resonant frequency around 2 MHz. We obtain the relaxation time coefficient α_R at the resonance, which is defined as the exponential decay constant of the ringdown curve, by fitting an exponential curve to it. The relation between α_R and α_m is investigated in detail. The reverberation signal is numerically simulated using α_R as the damping coefficient instead of α_m for individual reflection echoes in Fig.5.1. The resultant ringdown signal reproduces α_R as the exponential decay constant, showing that $\alpha_R=\alpha_m$ (Ogi et al., 1994). This is true when the input burst is much longer than the round-trip time T_0 and the integrator gate is short enough. The effects of liftoff and the case of slightly off-resonance are investigated, and both had shown to produce no significant influences on the attenuation measurement.

The resonant sharpness (or Q^{-1} value) also indicates α_m. Its measurement can be done quickly only through the resonant spectrum. However, the Q^{-1} value is a derived quantity based on the geometry of the resonance measurement (EMAT, sample thickness, liftoff ...). Moreover, the diffraction effect on the Q^{-1} value is unclear.

5.4. Correction for diffraction loss

Ultrasonic beam radiated from a finite transducer spreads perpendicular to the propagation direction and a part of the incident energy will not return to the sending transducer. This is called diffraction and causes the amplitude losses and phase shifts in the received echo signals. Following Seki et al. (1955), several authors (McSkimin, 1960; Papadakis, 1966) have studied the phenomena for longitudinal wave radiated from a circular piston source transducer. But, the existing solution is inadequate for the EMAR because of the non-circular geometry, a strength distribution over the radiating area, and highly overlapped echoes at a resonance.

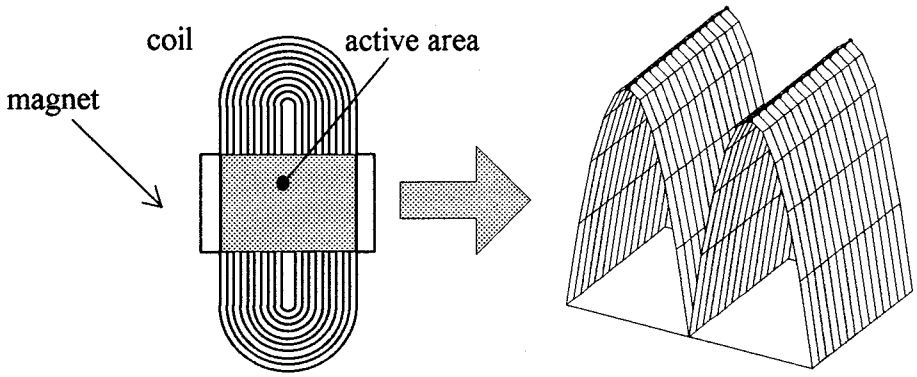

Figure 5.3 Approximation of the body force distribution by a pair of parabolic curves.

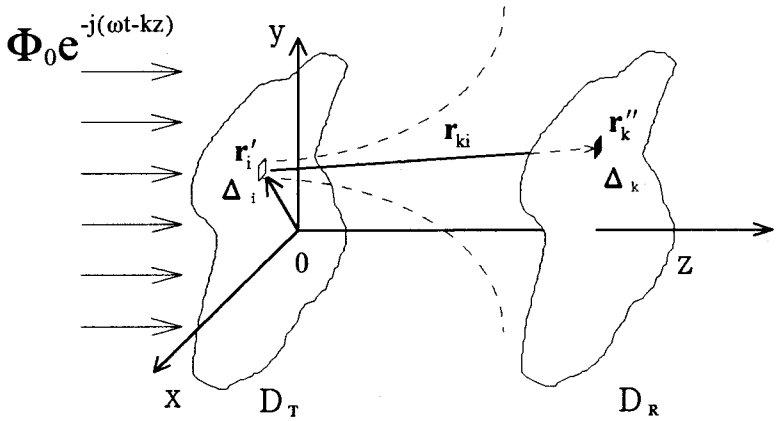

Figure 5.4 Numerical integration of the acoustic field on the receiving area D_R radiated from all elements on area D_T. Φ_0 expresses the strength ditribution on the radiating area. Δ_i and Δ_k are small areas on D_T and D_R; and $\mathbf{r}_i'$ and $\mathbf{r}_k''$ are their coordinates. $\mathbf{r}_{ki}$ is the vector from $\mathbf{r}_i'$ to $\mathbf{r}_k''$.

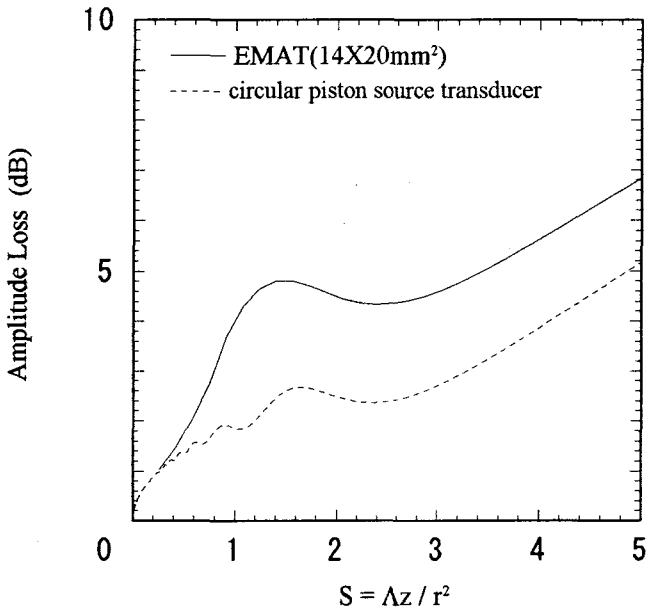

Figure 5.5 Calculated amplitude loss due to diffraction for the shear wave EMAT with rectangular area of 14x20mm² and the strength distribution of double-parabolic profile. Dotted line is the classical result for a circular piston source transducer by Seki.et.al.. Λ denotes the wavelength, z the propagation distance, and r the equivalent radius of the radiating area.

5.4.1. Diffraction phenomena radiated by an EMAT

The body forces induced by a bulk-wave EMAT has a three-dimensional distribution in the sample in general. With the help of the exact distribution available from the nonlinear FEM computation (Ogi et al., 1996b), we simplify the distribution to be two-dimensional on the sample surface, which is characterized by a pair of parabolic curves with the nodes at the edges and the center line as shown in Fig.5.3. This simplification is allowable when the sample material has a good electrical conductivity and a high permeability because such a material has a small electromagnetic skin depth, confining the body force in just the surface region. Assuming the distribution of the shearing force on the radiating area, we simulate the three-dimensional ultrasonic diffraction to calculate the amplitude and phase profiles on the receiving area at a distance. The radiation into the sample is considered by integrating the radiation fields from all the source elements, oscillating with the prescribed strengths, over the sending surface D_T as illustrated in Fig.5.4. The amplitude loss is obtained from the ratio of total power over the receiving area D_R to that on the radiating area D_T in a pulse-echo configuration (Ogi et al., 1995c). Figure 5.5 shows a calculated amplitude loss of the shear wave radiated from the bulk-wave EMAT whose effective area is 14x20 mm². For a

comparison, it contains the classical solution by Seki et al. (1955), which is no longer useful for correcting the diffraction loss for such a complicated transduction geometry as EMATs. The phase shift due to diffraction causes little influence on the attenuation measurement, because the variation is limited within the 0 to $\pi/2$ range and it is asymptote to the maximum $\pi/2$ as S ($=\Lambda z/r^2$) increases (Ogi et al., 1995c).

5.4.2. Correction at a resonant state

Figure 5.6 sketches the algorithm for correcting the diffraction effect at a resonance. Basically, the ringdown signal at a resonance is a superposition of reflection echoes of the resonant frequency with a constant phase. They are delayed by integer multiples of the round-trip time though the sample thickness (T_0). Their amplitudes undergo damping due to the attenuation plus the diffraction effect (neglecting α_e). The diffraction loss of each echo is provided by the diffraction data (Fig.5.5), specific to the EMAT in use, using the resonant frequency and the propagation distance. The diffraction effect causes different losses to individual echoes, because they propagate different distances. Since all the echoes are coherent, the shape of the ringdown curve is obtained by simply summing up the echo amplitudes successive delayed by T_0.

The correction proceeds as follows:

(i) Measurement of a series of resonant frequencies and then the relaxation time coefficient α_m at each of them,

(ii) Assumption of a trial time coefficient α' ($\alpha'<\alpha_m$), which is supposed to be free from the diffraction effect,

(iii) Calculation of the amplitude of the *i*th echo $E_i(t)$, which decreases at the rate of α' as shown in Fig.5.1; $E_i(t)$ can be determined by Eq.(2.5),

(iv) Giving further damping to $E_i(t)$ by incorporating the calculated diffraction data in Fig.5.5, and

(v) Getting the ringdown curve by numerically integrating these damped echoes overlapping heavily with a moving short gate. The gate width and the sweeping steps, as well as T_0 and T_B, follow the actual experiments. We obtain the time coefficient α'' by again fitting the curve to an exponential decay. Now, if the trial α' is the diffraction-free time coefficient, then α'' must equal the as-measured α_m, because α'' contains the diffraction effect. This series of calculations is repeated until $\frac{|\alpha_m - \alpha''|}{\alpha_m} < 10^{-4}$ is reached.

5.5. Comparison with usual technique

Figure 5.7 shows the attenuation measurements by the EMAR at a series of resonant frequencies for a 25-mm thick carbon steel ($100^l x 100^w x 25^t$). Two bulk-wave

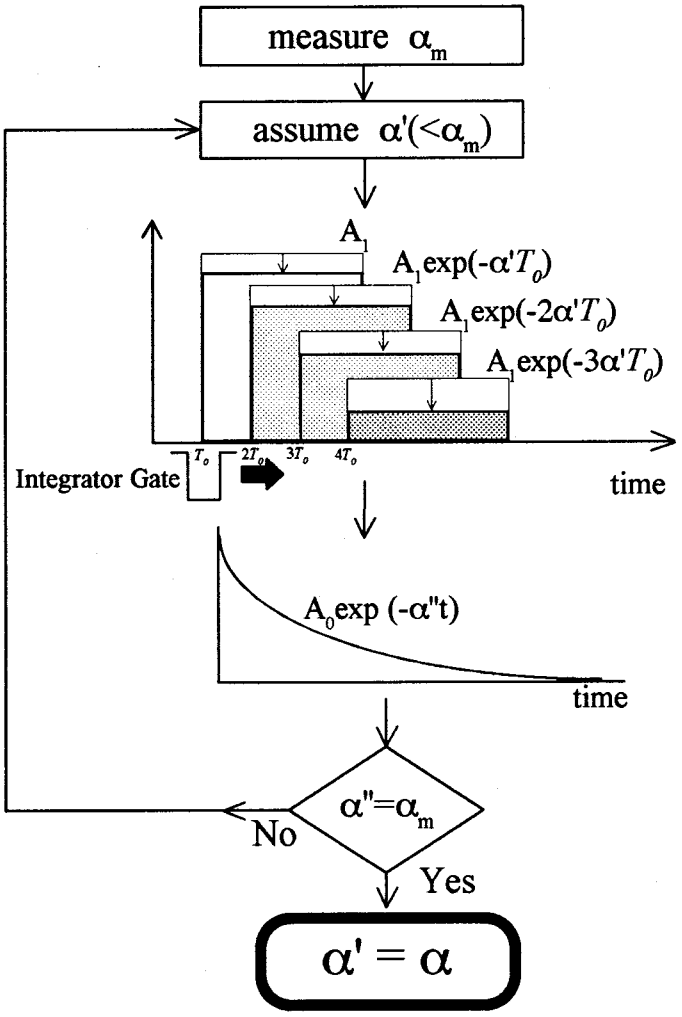

Figure 5.6 Correction process for diffraction effect. The echo height is decreased in two steps, first following the diffraction-free rate (α') and then the diffraction loss of Fig.5.5.

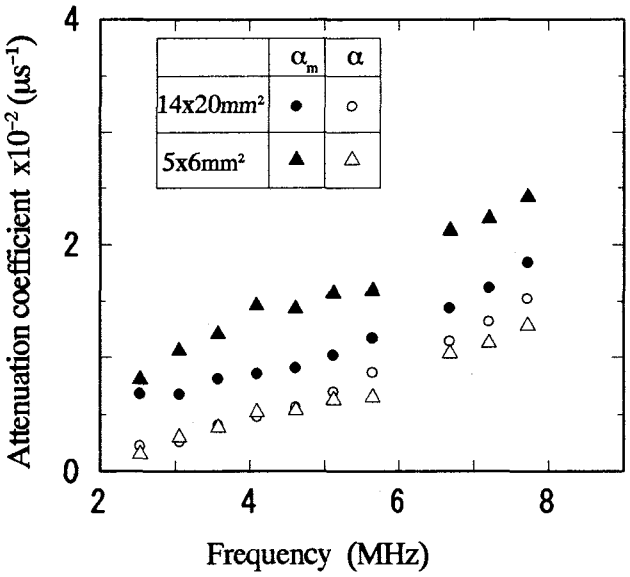

Figure 5.7 Measurement of attenuation coefficients for 25 mm thick carbon steel with two EMATs of 14x20 mm² and 5x6 mm² areas. Solid marks denotes as-measured data and open marks are corrected for diffraction effects.

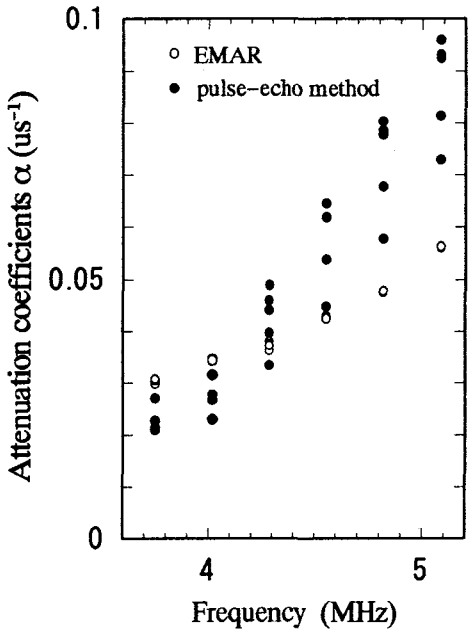

Figure 5.8 Attenuation measurements for a sample of 6 mm thick carbon steel with the EMAR and the pulse-echo methods.

EMATs are used; they are a large EMAT with the effective area of 14x20 mm^2 and a small EMAT with 5x6 mm^2. The burst signals of 120 μs duration is used to drive the EMATs and the integrator gate of 5 μs wide is swept every 1 μs along the time axis to have the ringdown curves. The figure includes the as-measured relaxation time constants (α_m) and the attenuation coefficients (α) after being corrected for the diffraction effect. It is clear that α takes the same value for the two EMATs, while α_m differs each other, reflecting the difference of the diffraction losses involved. The EMAR method is independent of the EMAT geometry after the diffraction correction is performed.

Additionally, the conventional pulse-echo measurement is made to have attenuation coefficient at the same resonant frequencies using digital FFT method. Figure 5.8 compares it with the EMAR measurements with the large EMAT for a 6 mm thick carbon steel sample (100^l x100^wx6^t). In the pulse-echo method, a piezoelectric shear-wave transducer is used which have 12 mm diameter and 5 MHz center frequency; and the transducer/buffer/sample system proposed by Papadakis (1984) is employed to minimize the effects of boundaries. The received signals are digitalized and the amplitude at each frequency is determined by conventional FFT method. For both methods, the diffraction effects were corrected. The measurements are repeated five times at the same position for each measurement. It is obvious that the EMAR method is superior to the pulse-echo method in reproducibility. This occurs not only because of using the noncontacting EMAT but also because a large number of echoes participate in the resonance, making the measurement stable and also robust against the noises.

5.6. Conclusion

The EMAR is revealed to be ideally suited to the ultrasonic attenuation measurements. Owing to the use of noncontacting EMATs, it conveniently excludes the interfering effects that occur with the conventional techniques. The measurement is only influenced by the diffraction phenomena, but the effect can be correctly removed using the numerical iteration procedure, resulting in an evaluation of the absolute attenuation coefficient. The measurement can be done with much ease and high reproducibility, accommodating unprepared samples as well. The relative accuracy of the attenuation measurement is in the order of 10^{-2} to 10^{-3}, depending on the attenuation itself.

The EMAR, however, is restricted to the plate geometry of samples, because the diffraction correction is unavailable for other geometries at present. In case of a thick sample, the intervals of neighboring resonant peaks become narrower and eventually they are overlapped, making the resonant frequency measurement inaccurate or infeasible. When the plate is too thin, the resonant peaks are disperse. Discrete measurement of attenuation at the resonances could be a problem. Interpolation is available to have the attenuation for intermediate frequencies.

CHAPTER VI

GRAIN SIZE EVALUATION IN CARBON STEELS

6.1. Introduction

Grain size of a polycrystalline metal is one of the key factors that govern the mechanical properties like yield stress and fracture toughness (Hall, 1970). Many techniques have been studied for the nondestructive evaluation of the grain size, including ultrasonic attenuation, X-ray diffraction, and magnetic tests. Among them, the ultrasonic technique is the most promising one, because it senses the through-thickness average of grain structure on which the mechanical properties mainly depend.

Ultrasonic wave propagating in the metal is scattered by grains because the grains possess different crystallographic orientations, causing the amplitude loss in a pulse-echo measurement. The relationship between the grain size and ultrasonic attenuation has been a principal topic in the area of ultrasonics (Rayleigh, 1894; Smith et al., 1981; Nicoletti et al., 1992). The classical study showed the fourth-power dependence of attenuation on frequency in the region where the grain size is much smaller than the probing wavelength (Rayleigh scattering). Although there has been a considerable research effort on the grain size evaluation using the formula in the Rayleigh scattering region (Mason and McSkimin, 1947; Papadakis, 1965; Smith et al., 1981), it is still under investigation. An apparent problem is the grain size distribution in the real metals, for which the power-law relationship was modified (Papadakis, 1963; Nicoletti et al., 1992). However, the main reason for the difficulty comes from the fact that the pure attenuation in the sample was not suitably determined from as-measured quantities. This basic, but essential problem, is solved by using an EMAT, which yields an absolute attenuation measurement.

In this Chapter, the frequency dependence of attenuation, presented by Mason and McSkimin (1947), is used for the grain size evaluation; that is, the attenuation coefficient consists of the absorption term proportional to frequency f, and the scattering term proportional to f^4. Attenuation measurement is performed on the steel samples by changing the carbon content, pearlite fraction, martensite fraction, surface roughness, or texture. The bulk-wave EMAT is used for detecting the frequency dependence of the shear wave attenuation. The shear wave is more sensitive to the grain size than the longitudinal wave (Bahatia, 1959). The final results are favorably compared with the average of the three-dimensional distribution of grain size calculated from the photomicrographs of the exposed cross sections of the samples.

6.2. Frequency dependence of attenuation

Generally, ultrasonic attenuation in a polycrystalline metal originates from absorption and scattering. Absorption is related to dislocation mobility (Granato and Lücke, 1956), thermoelastic effects (Lücke, 1956), magnetic structure (Levy and Truel, 1953), interaction with electrons and phonons (Mackinnon, 1955), interaction with electron or nuclear spin (Quinn and Ying, 1966). But at the room temperature and a low frequency of the megahertz order, the effects of electrons and phonons, and electron or nuclear spin are negligible. Furthermore, using only shear waves makes the thermoelastic effect almost ineffective because no volume change occurs in the shear deformation (Lücke, 1956). Consequently, the dislocation damping and the magnetoelastic effect are only responsible for the absorption. The relationship between the dislocation and the frequency dependence of the attenuation shows the second-power dependence in low frequencies. But a narrow range of frequency used here (1-10 MHz) allows the simplification of a linear dependence on frequency. The magnetoelastic effect also shows a linear function of frequency (Levy and Truel, 1953). It is, therefore, considered that attenuation due to the absorption effects is proportional to frequency. On the other hand, the attenuation caused by the grain scattering in the Rayleigh region shows the fourth-power dependence on frequency (Bhatia, 1959).

After all, the frequency-dependence of the shear-wave attenuation is approximated as

$$\alpha(f) = af + SD^3 f^4 , \tag{6.1}$$

where a is the absorption factor, S the scattering factor, and D the average grain size. The different dependence of α on f allows us to separate the absorption and the scattering contributions. Bhatia (1959) derived the scattering factors for longitudinal and shear waves. His theoretical result shows that the grain scattering occurs more intensively for the shear wave than for the longitudinal wave. This brings a great advantage of using the shear wave for the grain size evaluation. On the other hand, the attenuation by absorption is smaller for shear waves than for longitudinal waves because of the thermoelastic effect acting only for longitudinal waves. Therefore, the separation of absorption and scattering effects is much easier for the shear wave, resulting in more accurate evaluation of grain size. From the experimental side, the shear wave resonance is most easily detected with the bulk-wave EMAT.

6.3. Carbon steel samples

The steel plates are prepared for the evaluation. The various influences are investigated as follows;

(i) carbon content: thirteen samples with three different carbon contents of 0.007mass%, 0.062mass% and 0.147mass%,
(ii) pearlite fraction: four samples with 2%, 61%, 80%, and 98% pearlite volume fractions,
(iii) martensite fraction: twelve samples with four different martensite volume fractions of 15.3%, 20.5%, 30.9%, and 39.4%,
(iv) surface roughness: seven samples with different average roughness ranging from R_a=0.14μm to 8.7μm, and
(v) texture: three samples with the birefringence (B_0) of 1.58%, 3.00%, and 5.19%.
All samples were sized 6^tx100^lx100^wmm^3.

Naturally, each sample possesses a grain size distribution. The photomicrographic examination only reveals the two-dimensional (2D) distribution on an exposed cross section. The average size determined from such an examination is smaller than that of the three-dimensional (3D) distribution, which substantially influences the mechanical characters of the bulk material. The grain diameter appearing on the observation plane is smaller than the real diameter of the grain. Especially, for a grain structure which is far from being equiaxial, the cross sectional diameter is more likely to underestimate the average grain size. We calculated the 3D distribution from the measured 2D distribution by applying the model that the grain shape is a regular polyhedron or semi-regular one whose number of the faces is determined only from the size, and each grain has the unique diameter distribution on the exposed cross section depending on the number of the faces (Matsuura and Itoh, 1991). Figure 6.1 shows an example of the photomicrograph on a exposed cross section and the calculated 3D distribution. The average grain size in the 3D distribution (23μm) became larger about ten percent than that of the 2D distribution (21μm). The fraction of the small grains in the optical observation also decreases in the calculated 3D distribution, resulting in a narrower spread of diameter.

6.4. Measurement of grain size

In the measurement of a resonance frequency, the burst signal of 40μs duration is used to excite the EMAT. The frequency is swept by 500-Hz steps. The ringing signals are integrated with the gate of 200-300μs long, involving approximately from fifty to eighty reflection echoes (T_0~3.7μs). In the attenuation measurement, the integrator gate of 5 μs long is swept at every 1 μs from just after the excitation until the ringing completely fades down. Figure 6.2 shows a measured series of resonant frequencies and the ringdown curves at three resonance frequencies for a steel sample. The frequency dependence of the attenuation is obtained from the attenuation (α) at discrete the resonant frequencies, as shown in Fig.6.3. We plotted both the as-measured coefficient α_m and the pure attenuation coefficient α after correcting for the diffraction ef-

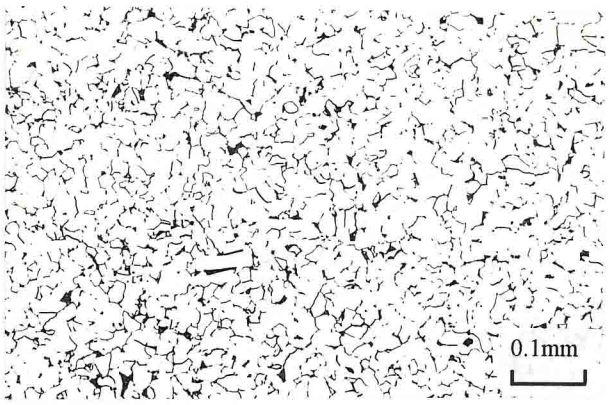

(a)

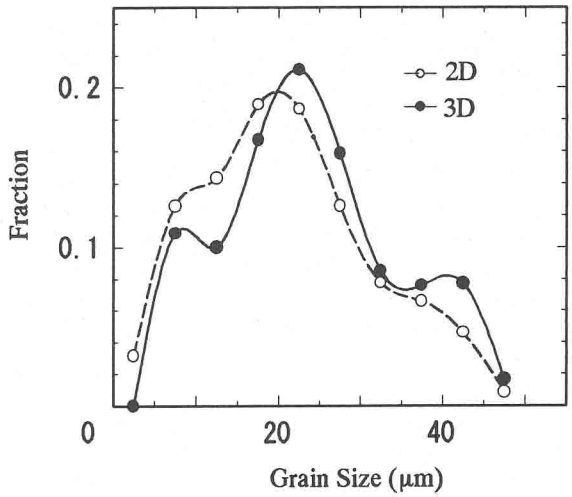

(b)

Figure 6.1 (a) Mircrograph of the exposed area and (b) calculation of three-dimensional grain size distribution for the steel sample with 0.062mass% carbon content.

fect. The corrected data (α) shows a better fitting to Eq.(6.1), especially in the low frequency region, where the diffraction introduces a larger error. The frequency dependence of α approaches a linear dependence as the grain size decreases, showing the dominant absorption term over the scattering term in Eq.(6.1). The average grain size is obtained by fitting Eq.(6.1) to the measured $\alpha(f)$ and extracting the term in f^4. With a suitable scattering factor S, the coefficient of the f^4 term provides the average grain size. Although the scattering factor can be derived theoretically (Bhatia and Moore, 1959), we calibrated S to be S=2.25x10^{-10} μs^3/μm^3 using as a reference steel sample that has the narrowest distribution of grain size.

Papadakis (1961) pointed out that D^3 in Eq.(6.1) should be replaced by $\langle D^6\rangle/\langle D^3\rangle$, $\langle\rangle$ being the average. This formula is first applied to the present experiments with the inferred 3D distribution grain size and the recalibrated S. The EMAR result, however, gave much smaller grain size than that determined from the photomicrographic method. It is found that the use of $\langle D\rangle^3$ for D^3 in Eq.(6.1) leads to the most

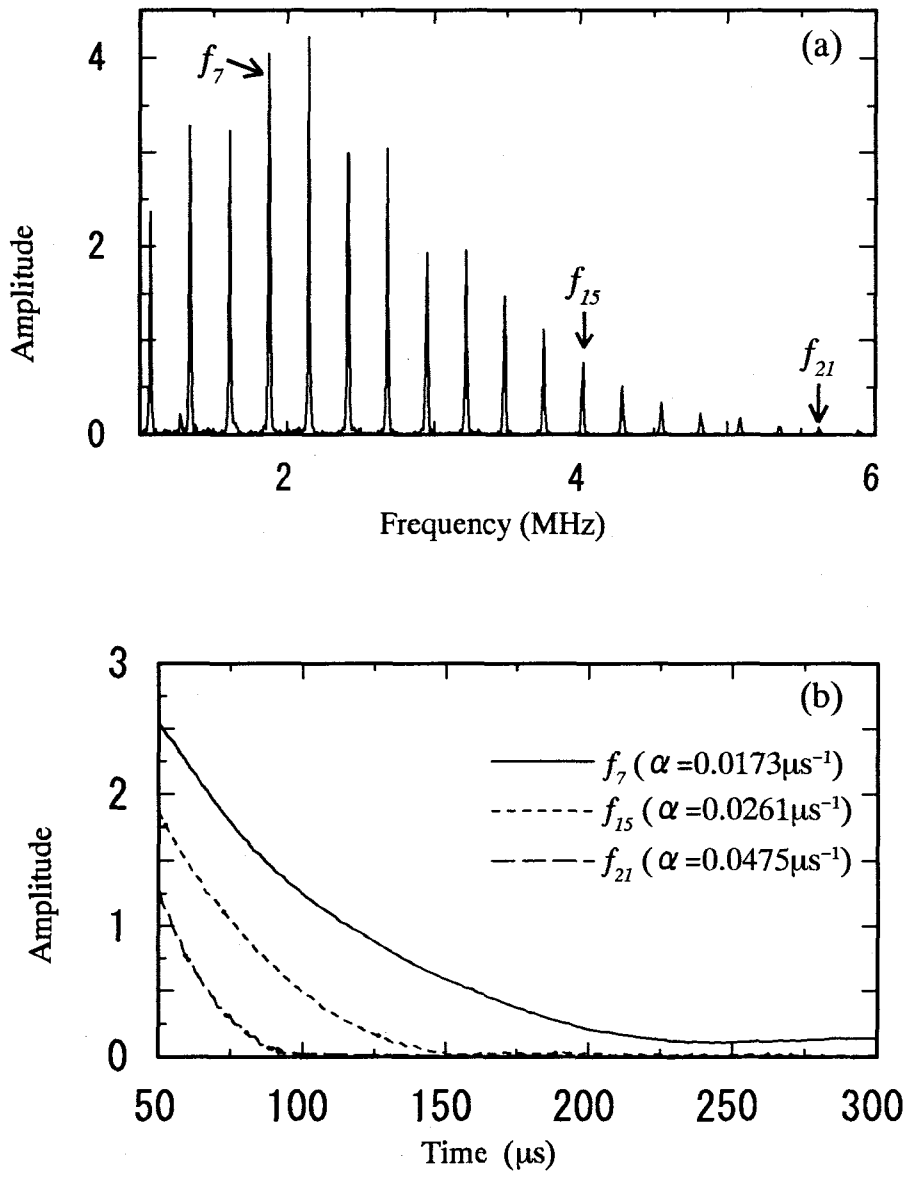

Figure 6.2 Measurement of (a) resonant frequencies and (b) attenuation curves at three resonant frequencies.

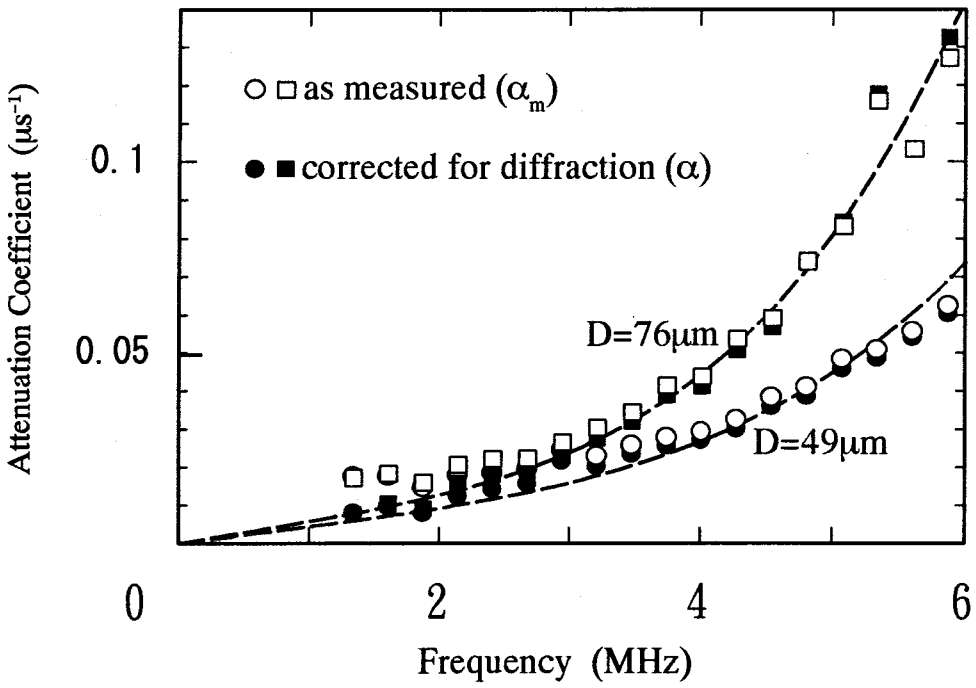

Figure 6.3 Measurement of frequency dependence of shear wave attenuation.

acceptable agreements with the photomicrographic examination. The grain sizes evaluated thus (D_{EMAR}) is compared with those of the optical measurement after converting to the 3D distribution (D_{PHOT}) in Fig.6.4.

6.5. Discussions

The grain sizes evaluated by EMAR well agree with those by photomicrographic method within a band of 6μm. But, there are some outliers. The unfavorable results for the samples containing the martensitic phase is explained from two points. First, the definition of "grain" is fairly different between the photomicrographic method and the EMAR. The former recognizes it simply from the boundaries of components, but the latter finds it from the elastic discontinuity. The sizes estimated by the two methods, therefore, do not necessarily agree with each other, especially when there is a hierarchy in the metallurgical structure like the martensitic steel. Second, the dual phase (martensite and ferrite) system introduces another scattering problem. In the sample with two phases, the scattering occurs not only due to elastic anisotropies within a phase but also due to the phase boundaries (Ying and Truell, 1956). This means that Eq.(6.1), derived from the single-phase theory, is no longer usable. The favorable results for the samples containing pearlite, which are also of dual phase system (pearlite

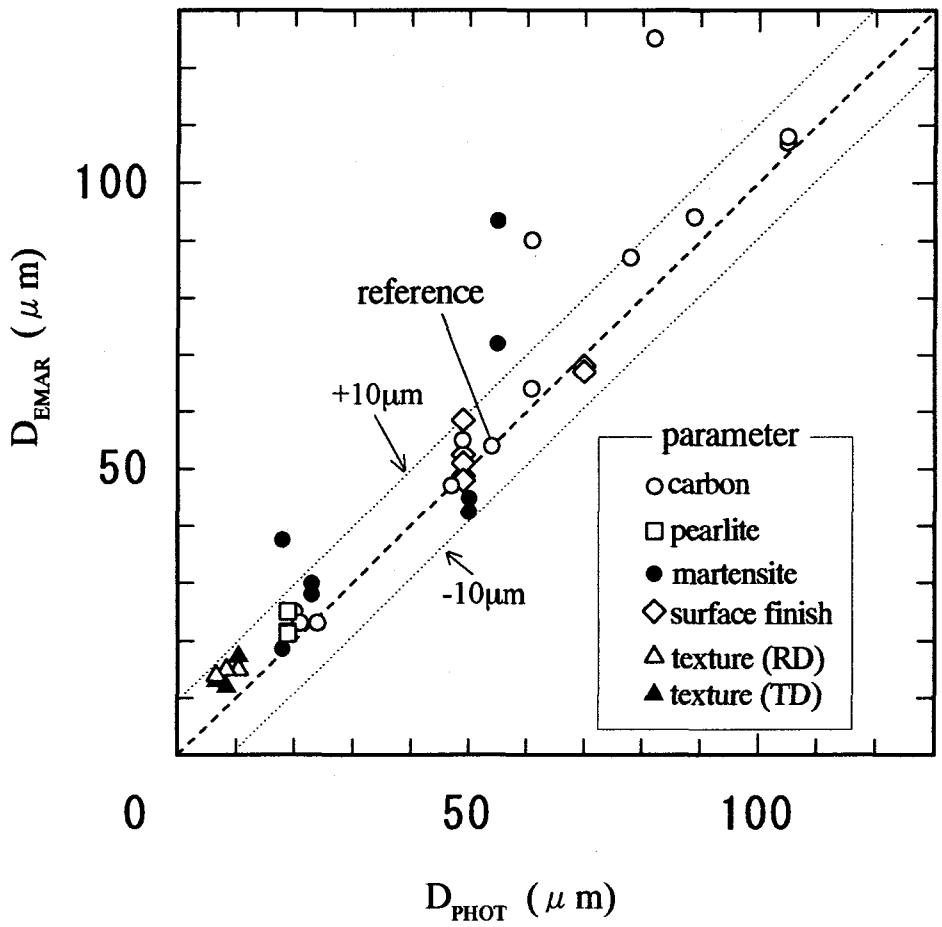

Figure 6.4 Results of measured grain sizes. The horizontal axis denotes the 3D average grain sizes determined from photomicrographs and the vertical axis are those measured with the EMAR method.

and ferrite), suggests the nearly equal elastic properties between the pearlite and ferrite structures.

There are two more samples that show greater D_{EMAR} than D_{PHOT} among those of changing the carbon content. These samples both possess broad distributions of grain size, involving plural peaks. Since Eq.(6.1) strictly applies to the hypothetical poly-crystalline material composed of single-size grains, the formula becomes progressively inadequate as the distribution broadens.

Surface roughness can cause the extra attenuation, following the f^2 law (Nagy and Rose, 1993). Generally, the separation between the attenuation due to the surface roughness and that by grain scattering is difficult because of the fairly close dependence on frequency (f^2 and f^4). The effect is more likely to be included in the scattering term in Eq.(6.1) overestimating the grain size. But, in Fig.6.4, D_{EMAR} is larger than D_{PHOT} by only 8 μm even for the roughest surfaces of R_a=8.7μm. The effect of surface roughness is then insignificant for the present set of samples.

For the samples with texture, two shear waves polarized in the orthogonal directions are independently used for the measurement, but no significant effect of the texture on the grain size evaluation is observed.

6.6. Conclusion

The EMAR technique was applied for the grain size determination of steel samples. Grain size evaluated by the EMAR showed a good agreement with those estimated by photomicrographic measurements within an error budget of 6 μm, except for some samples. The measurement did not suffer from carbon content, pearlite content, surface roughness (up to Ra=8.7μm), and texture. The unfavorable evaluation took place for the samples containing the martensite phase, which is caused by unclear observation of grain boundaries in the photomicrographs. It should be noted that the definition of "grain size" differs between the photomicrographs and acoustics. While the former simply regards the boundaries of components as the grain boundaries, the latter finds the grain boundary from the elastic discontinuity. Thus, the EMAR is not always comparable with the photomicrographs method. The EMAR gives too large average grain size for samples with broad distribution of grain size.

The grain size measurement with the EMAR has a restriction on the measurable thickness. Too thick samples would cause the overlapping of neighboring resonant peaks and also the thinner plate samples would decrease the number of measurable resonant modes and reduce the accuracy of the evaluation because of fewer data of the frequency dependence of α.

CHAPTER VII

MONITORING OF DAMAGE ACCUMULATION DURING ROTATING BENDING FATIGUE

7.1. Introduction

Nondestructive sensing of fatigue damage in metal structures has been an important subject for ensuring their safety and reliability. The goal is the detection of some indicative phenomena much earlier than when the crack becomes visible with a conventional inspection technique, leading to the continuous monitoring of the damage progress. This Chapter describes the ultrasonic monitoring of the fatigue damage accumulation process of steel pipes exposed to rotating bending. For this, a new transduction technique is developed, which relies on the magnetostrictive effect, to make use of axial-shear acoustic resonance around the outer surface of a sample steel pipe. The fatigue monitoring is made possible by observing the resonant frequency and the attenuation coefficient with the EMAR method.

The axial shear wave propagates along the circumference of the cylindrical rod or pipe with the polarization in the axial direction. This mode of elastic wave is available only with the EMATs in practice. The major advantage is the capability of evaluating the inhomogeneous microstructure or character in the radial direction using the different resonant modes. Each resonant mode has the normal function showing the amplitude peak at a specific radius, to which the measurement result is selectively sensitive. Johnson et al. (1992) first detected the EMAR spectra of the axial shear resonance from a cylindrical rod. They employed the Lorentz force mechanism to design the EMAT, which was built with many permanent magnets periodically spaced around the rod and a solenoidal coil surrounding the rod surface. The spacing of the magnets corresponds to the wavelength of the SH (shear horizontal) wave to be generated. When a higher spatial resolution in the radial direction is required, the EMAT designing involves using a larger number of thinner permanent magnets. Such an array of thin magnets cannot introduce a strong field in the sample surface and is vulnerable to the liftoff (air gap). The present study invented an alternative EMAT relying on the magnetostrictive effect of ferromagnetic metals. This EMAT consists of a solenoidal coil to apply a static field along the axial direction of a sample pipe and a meanderline coil to induce the dynamic field. The meanderline spacing determines the wavelength of the shear wave and then the spatial resolution of the inspection. It is easy to make the small spacing, that is, to

evaluate the sample material with the higher radial resolution.

The influence of metal fatigue on the ultrasonic properties is a long-running problem in the field of physical acoustics (Golovin and Puskar, 1993; Fei and Zhu, 1993; Zhu and Fei, 1994). Among others, the ultrasonic attenuation (or internal friction) has been used to identify the fatigue stage of metals. Previous work (Firestone, 1948; Ivanova, 1967; Truell and Hikata, 1957; Bratina and Mills, 1962; Pawlowski, 1964) showed that, in high cycle fatigue testing, the attenuation rate increases slightly at the beginning of the fatigue life and after experiencing a long stable period, it remarkably increases just prior to failure. The initial increase is explained by the increase of the dislocation density and the final increase is attributed to the occurrence of microcracks and their subsequent growth.

The present axial-shear EMAR measurement reveals a novel feature of the ultrasonic-fatigue relation. A sharp attenuation peak and a velocity depression always appear at 80-90 % of the life; this could be a warning to approaching fracture. With the help of optical micrographs, transmission electron micrographs, and replica films, we conclude that the change of the ultrasonic properties is caused mainly by the change of the dislocation structure. The acoustic data allow the calculation of the dislocation density and the loop length on the basis of Granato-Lücke's string model (1956).

7.2. Measurement of axial shear resonance

7.2.1. New EMAT configuration

In the analysis presented in Chapter III, considering the case of the tangential bias field $\mathbf{B}=(0, B_{02}, 0)$, being parallel to the driving current, we find that the surface SH-wave is excited, which polarizes in the x_2 direction and propagates along the x_1 axis, that is $\mathbf{u}=(0, u_2 e^{j(\omega t+k_3 x_3+k_0 x_1)}, 0)$. In this case, only the magnetostriction effect is the effective mechanism and no Lorentz force and magnetization force arise. When the sample is a cylindrical rod or pipe, the SH-wave travels along the circumferential direction, which is the axial shear wave.

Figure 7.1 illustrates the magnetostrictively-coupled EMAT for generating and receiving the axial shear wave. It consists of the solenoidal coil to introduce the static field in the axial direction of a steel pipe (or rod), and the meanderline coil of equal spacings surrounding the sample surface. Applying a sinusoidal current to the meanderline coil, it produces the dynamic field in the circumferential direction. The dynamic field is superimposed on the static field and the total field acts along the vector sum of these two fields. The magnetostriction takes place in the direction of the total field, depending on its magnitude. Then, the surface element undergoes an oscillating shear deformation. The SH wave is thus excited and propagated along the circumference having the axial polarization (Thompson, 1979; Ogi et al., 1996a). The same meanderline coil receives the wave in the reversed process.

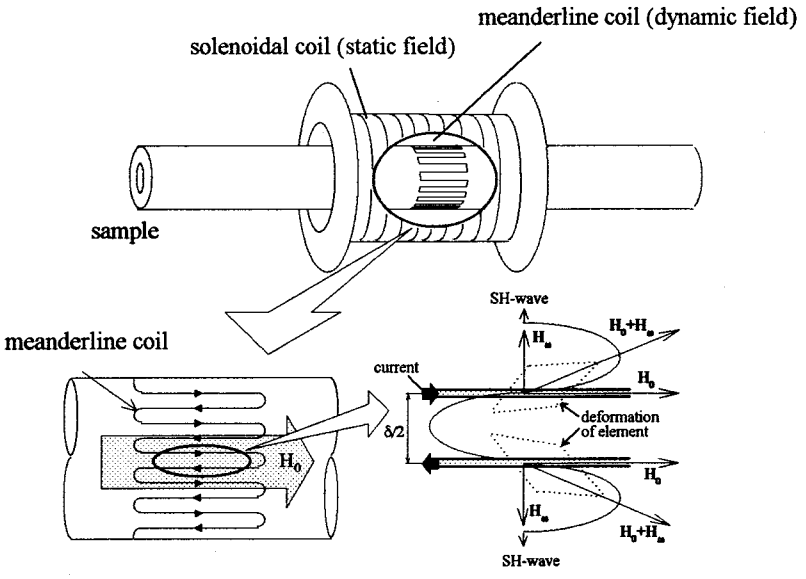

Figure 7.1 Principle of the EMAT for axial shear resonance.

7.2.2. Axial shear resonance spectrum

Resonant modes of the axial shear wave can be calculated by solving the elastodynamic equation with the boundary conditions for the free surfaces. For a pipe, we have the frequency equation (resonant condition) as

$$\left\{\frac{nJ_n(kR_a)}{kR_a} - J_{n+1}(kR_a)\right\}\cdot\left\{\frac{nY_n(kR_b)}{kR_b} - Y_{n+1}(kR_b)\right\} - \left\{\frac{nJ_n(kR_b)}{kR_b} - J_{n+1}(kR_b)\right\}\cdot\left\{\frac{nY_n(kR_a)}{kR_a} - Y_{n+1}(kR_a)\right\} = 0 \quad , \tag{7.1}$$

where J_n and Y_n are the nth Bessel functions of the first and the second kinds, respectively; R_a and R_b are the outer and inner radii ($R_a > R_b$) and k is the wavenumber ($k = \omega/c$), where ω is the angular frequency and c is the shear wave velocity. Integer n is determined by

$$n \sim 2\pi R_a / \delta \quad , \tag{7.2}$$

where δ is the meanderline period (Fig.7.1). Numerical solution to Eq.(7.1) provides a series of resonant frequencies, $f_m^{(n)}$, with another integer m identifying the overtones. Figure 7.2 shows the calculated displacement amplitudes for the first three resonant modes at n=48 (i.e. $f_1^{(48)}$, $f_2^{(48)}$, and $f_3^{(48)}$) for a steel pipe with R_a=10 mm and R_b=5 mm.

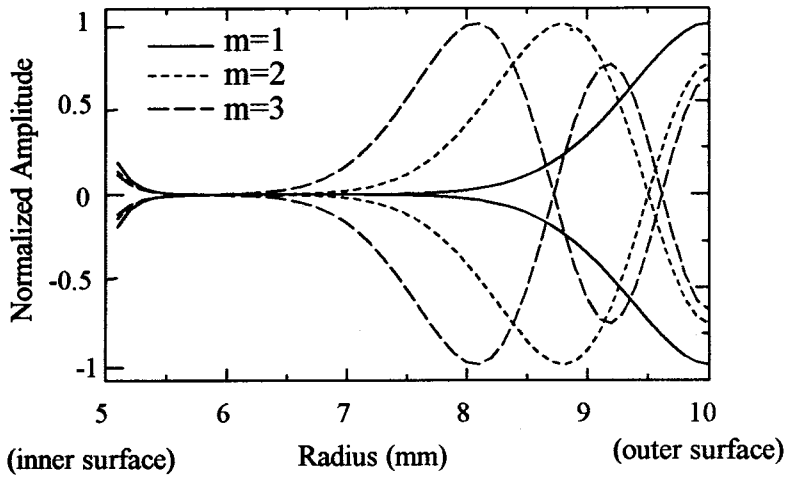

Figure 7.2 Amplitude distributions at three resonant modes for the pipe of 20mm-outer diameter and 10mm-inner diameter (n=48).

The oscillation of the first mode is restricted to the outer surface region and as the mode becomes a higher overtone, the peak amplitude moves to the inside of the pipe. It is then possible to evaluate the microstructure gradient in the radial direction using the different resonant modes. The integer n determines the penetration depth of the fundamental mode and therefore governs the spatial resolution of the measurement. The fundamental mode (m=1) with larger n is best suitable for the characterization focused on the most outer region, where the damage develops preferentially in the rotating fatigue due to the higher bending stress and a reduced constraint on deformation.

7.2.3. Resonant frequency and attenuation coefficient

The measurement of the resonant frequency and the attenuation coefficient of the axial shear wave follows the previous Chapters. The measurement proceeds in several steps, but the procedures are programmed in a single run, which finishes in a short time (~10 sec). The meanderline coil of 20-mm width is fabricated by printing copper on a polyimide sheet. Figure 7.3 shows a typical axial shear resonant spectrum measured for a steel pipe of R_a =10 mm and R_b=5 mm, where we used the magnetostrictively-coupled EMAT of n=48. A resonant frequency is determined by fitting the Lorentzian function to the measured spectra around each peak and calculated the center axis. The resonant frequencies are observed in uneven intervals (c.f. Fig.6.2(a), for a plate). The measured resonant frequencies agree with the calculation based on frequency equation (7.1) within the error band of 1 kHz.

Following a measurement of the resonant frequency, the ringdown curve is measured by driving the same EMAT with the measured resonant frequency and stepping

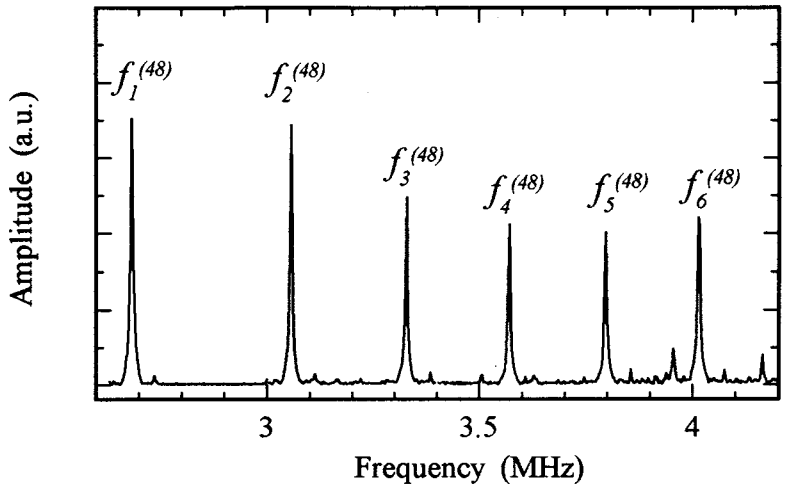

Figure 7.3 Measured resonant spectrum of the steel pipe.

the narrow gate along the time axis. The attenuation coefficient is obtained for each resonant mode by fitting an exponential decay to the measured ringdown curve and calculating the time coefficient. The as-measured time coefficient contains the attenuation in the sample and also the diffraction loss, which occurs due to the beam spreading in the axial direction. The diffraction effect is, however, not significant, because this is a one-dimensional diffraction from the wide meanderline coil. Furthermore, we are mainly interested in the relative change of the attenuation throughout the fatigue life.

7.3. Monitoring of rotating fatigue damage

7.3.1. Setup of four-point bending fatigue test

Figure 7.4 is a sketch of the rotating bending setup. Tested were extruded carbon steel pipes (JIS-STKM13A), being 1m long, 20mm outer diameter, and 10mm inner diameter. The carbon content is 0.23 mass %. The motor rotates the pipe at 240 rpm (4 Hz). The four-point bending stress is applied by external weights. The maximum bending stress is 240 MPa on the outer surface, which is about 80 % of the yield stress. We introduced a smooth shallow notch of 30 μm deep and 1 mm wide around the circumference at the center of the pipe. The surrounding area was electrolytically polished in a solution of 9 parts of CH_3COOH and 1 part of $HClO_4$ to produce a surface of high quality.

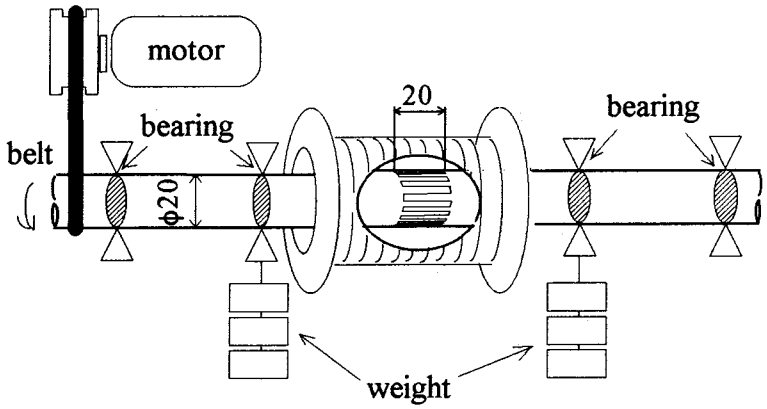

Figure 7.4 Setup of rotating bending fatigue test.

7.3.2. Evolution of the resonant frequency and the attenuation coefficient

The resonant frequencies and the attenuation coefficients at the lowest three modes were measured during the fatigue test. The static field from the solenoidal coil was fixed to 1.4×10^4 A/m. At each measurement, we interrupted the rotation and the bending to make a brief measurement and then restarted the fatigue test. This procedure was repeated until failure occurred.

Figure 7.5 is the typical evolution of the attenuation coefficient and the resonant frequency shift. The horizontal axis is exponentially elongated as the cycle number becomes larger, because the important behaviors of the ultrasonic properties are observed near the end of the fatigue, which would not be clearly visible with the linear scale of the cycle number. The resonant spectra and the ringdown curves for the fundamental mode at three representative fatigue stages are given in Fig.7.6. We carried out similar tests for thirteen samples and observed the same features of ultrasonic-fatigue interaction, although the total numbers of cycles to fracture varied between 50,000 and 650,000 cycles, probably depending on the surface condition and the microstructure. General observations are:

(i) At the initial stage, the attenuation coefficient increases and the resonant frequency decreases for all three resonant modes.

(ii) Both the attenuation and the resonant frequency change little for nearly half the fatigue life.

(iii) Around 80-90 % of the life, the attenuation coefficient jumps to a maximum value and then it levels off immediately. Simultaneously, the resonant frequency experiences a small depression and then becomes stable.

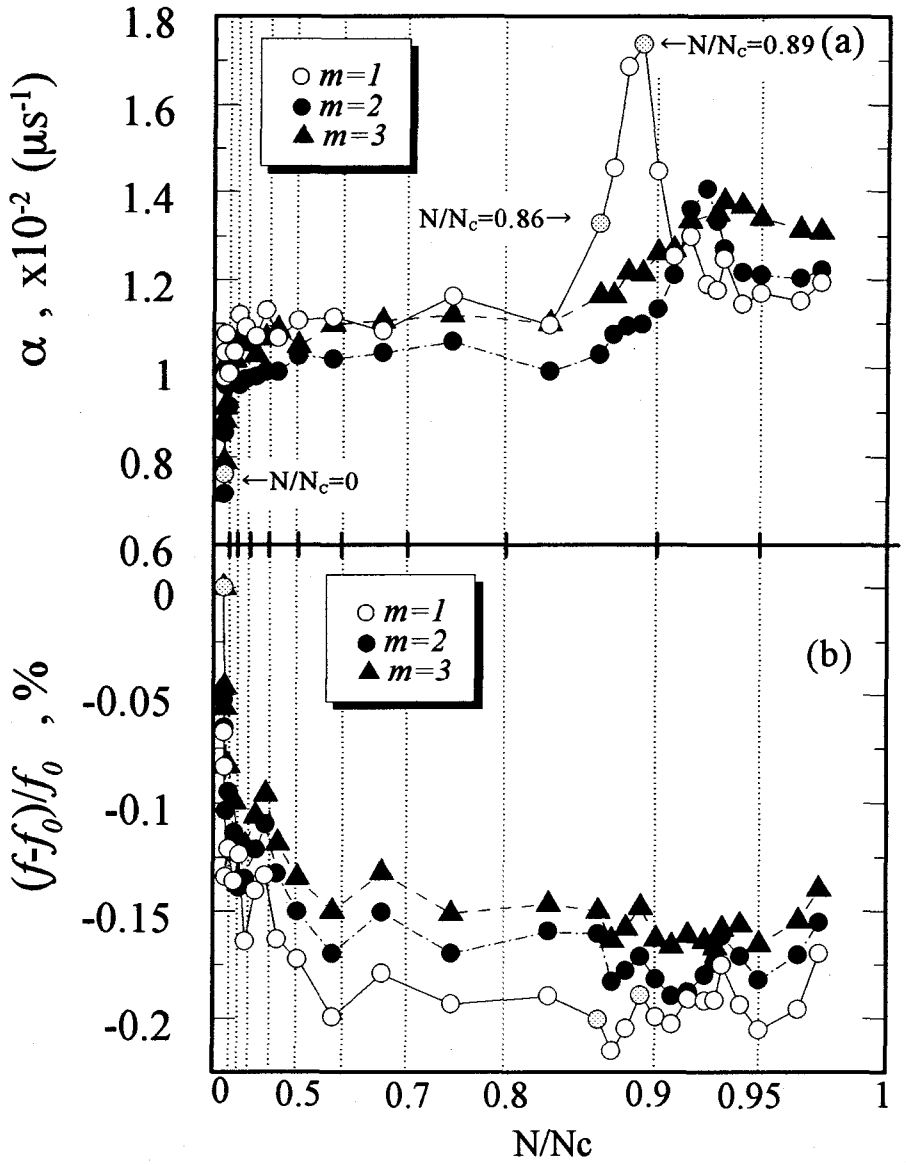

Figure 7.5 Evolution of attenuation coefficient and resonant frequency shift during the fatigue life (N_c=610,000). f_0 is the original resonant frequency.

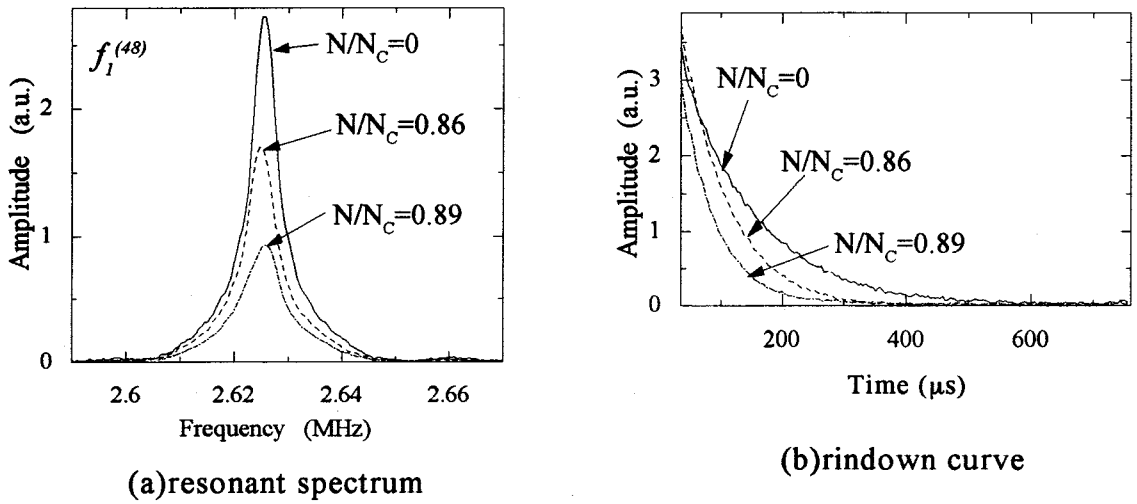

(a)resonant spectrum

(b)rindown curve

Figure 7.6 (a) Resonant spectra and (b) ringdown curves at three fatigue cycles indicated in Fig.7.5.

(iv) The attenuation coefficient changes more noticeably than the resonant frequency. The attenuation peak appears to be more than twice as high as the original attenuation, while the variation in the resonant frequency is limited to within 0.2-0.3%.

(v) The attenuation peak of the fundamental mode is observed to the largest magnitude and earliest among three modes, as has been expected.

Despite the extensive research on the relation between the attenuation and fatigue damage, no one has reported this attenuation peak. This is partly because the peak is so sharp and is likely to be overlooked by the conventional techniques. The second reason is the high sensitivity of the method. Owing to the noncontact transduction, the EMAR method is capable of providing the absolute value of attenuation coefficient, which represents the damping character in the material. The EMAR excludes extra energy losses, which are indispensable when using the contact transducers and would very possibly mask the minute indications of the microstructural changes. Furthermore, the contactless transducer yields highly reproducible data independent of the measuring conditions. Unfavorable factors like liftoff and surface roughness will diminish the spectrum intensity and the amplitude of the ringdown curve, but they don't change the decay rate, from which the attenuation coefficient is determined. Equally important is the concentration of the ultrasonic deformation to the outer surface of the sample pipe. This is made possible by incorporating the magnetostrictive mechanism for the transduction and using the fundamental axial shear mode at large n.

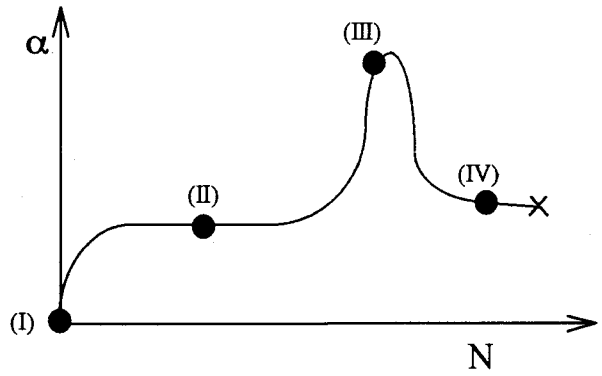

Figure 7.7 Four fatigue stages based on the attenuation character.

7.4. Microstructural changes

Seeking a satisfactory explanation to the above behavior, the microstructure and its change were studied during the fatigue test. Four fatigue stages are selected; stage I: before the test, stage II: in the stable region, stage III: just before the fundamental mode shows the attenuation peak, and stage IV: after the attenuation peak of the fundamental mode (Fig.7.7). The optical micrograph serves to observe the cracks and the grain size and the transmission electron micrograph (TEM) to know the dislocation structure. For these observations, we truncated the fatigue loading and extracted specimens in the vicinity of the notch. The replica method was also used to trace the surface crack growth throughout the test.

7.4.1. Optical micrography observation

Rectangular specimens including the notched area of $3x3x5mm^3$ were sampled and examined over the cross sectional area of $3x5mm^2$ normal to the circumferential direction. The specimens were etched in a solution of 95 parts of C_2H_5OH and 5 parts of HNO_3.

It was found that small cracks and slip bands existed along the notch bottom as early as 20-30 % of the total life. Besides this, no significant difference were observed among stages I through III (Ogi et al, 1997). However, a grain refinement was seen in the surface region at stage IV. The grain size was 12-14 μm through stages I to III, and also at the interior region of stage IV. But, it decreases to around 9 μm in the proximity of the notch bottom at stage IV. This can be explained by the developing the subgrain structure due to the cyclic loading (Ivanova, 1967).

7.4.2. TEM observation

Three slices of 0.2-mm thick were taken from each specimen using the electrical discharge wire and mechanically polished them to 0.1 mm thick. The slice faces were

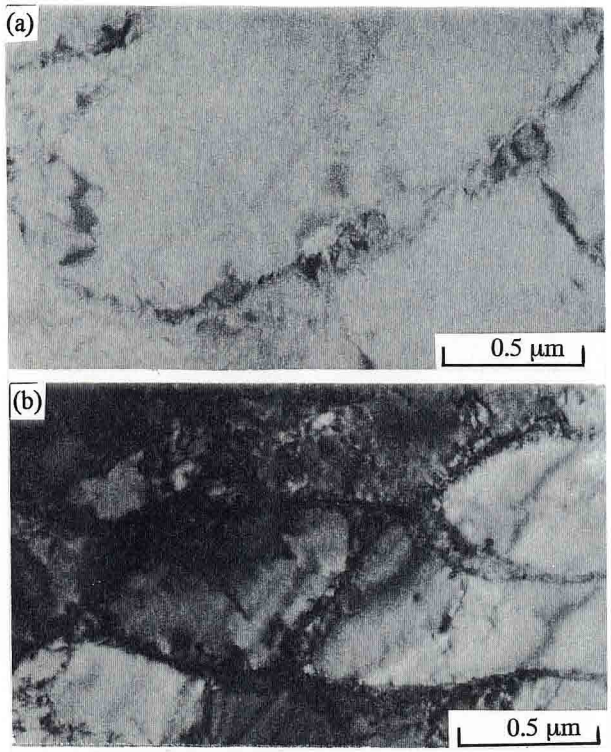

Figure 7.8 TEM images on the notch bottom from (a) stage I and (b) stage III.

oriented parallel to the original sample surfaces. They were then given an electrolytic polishing in a solution of 9 parts of CH_3COOH and 1 part of $HClO_4$ to make small center holes, around which the TEM images were obtained.

Figures 7.8 shows representative micrographs from stages I and III. Examining a large number of such TEM images, it is revealed that the dislocation density continued increasing during the stable period (stage II). At stage III, the dislocations had multiplied to a considerable level, developing the cell structures, which were absent at stages I and II. Cell structures developed to a larger extent at the surface rather than in the interior. At stage IV, the dislocation density increased to the maximum and occupied the whole viewing area.

7.4.3. Replication

The replication technique provided the *in situ* observation of the macroscopic cracking at the notch bottom. The acetyl cellulose film and methyl acetate were used for this purpose. The bending stress is applied to open the cracks. Figure 7.9 compares the EMAR measurements for the fundamental mode with the maximum crack length obtained from the replica films.

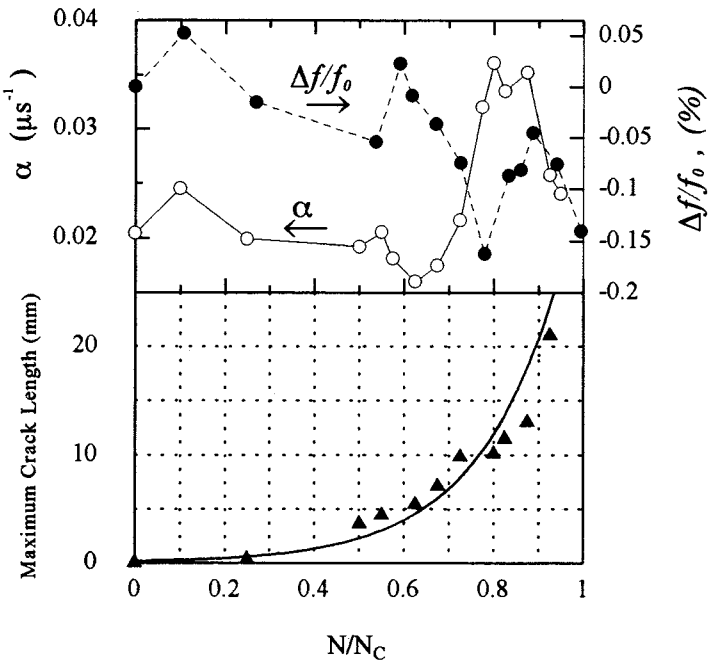

Figure 7.9 Relation between the attenuation change and velocity shift of the fundamental mode, and the maximum crack length on the notch bottom (N_c=210,000).

7.5. Discussions

Dislocation damping, scattering at grain boundaries and fatigue cracks are the potential sources contributing to the evolution of the ultrasonic properties (α and f) during the fatigue tests.

The classical string model (Granato and Lücke, 1956) states that in the lower frequency region, the dislocation serves to change the attenuation coefficient α_{dis} and the velocity v via

$$\begin{cases} \alpha_{dis} = \left(\dfrac{16GBb^2}{\pi^4 C^2}\right)\Lambda L^4 f^2 \\ \dfrac{v_0 - v}{v_0} = \left(\dfrac{4Gb^2}{\pi^4 C}\right)\Lambda L^2 \end{cases}, \qquad (7.3)$$

where G is the shear modulus, B the specific damping constant, Λ the dislocation density, L the dislocation loop length, and b the Burgers vector. C denotes the line tension of an edge dislocation and is expressed by $2Gb^2/\pi(1-\nu)$ with Poisson's ratio ν (Truell et al., 1969). v_0 is the dislocation-independent velocity of the material, which in principle would have to be measured at such a high frequency that the dislocation cannot oscil-

late responding to the elastic waves.

Grain boundaries can also be the source of ultrasonic attenuation (see Chaper VI). An ultrasonic wave propagating in a polycrystalline metal undergoes scattering due to the different crystallographic orientations of adjacent grains, causing an energy loss. When the probing wavelength is much larger than the grain size (Rayleigh scattering regime), the attenuation coefficient α_s is expressed by (Bhatia, 1959)

$$\alpha_s = SD^3f^4 , \tag{7.4}$$

where S is the scattering factor and D the average grain size. The grain size makes a contribution to the attenuation through D^3. The effect is, however, not the principal mechanism in the present case. Based on a grain size of about 9 μm near the surface in stage IV and 14 μm in stage III and using the scattering factor $S = 2.25 \times 10^{-10}$ $\mu s^3/\mu m^3$ derived in the previous Chaper for the shear wave in steels at a frequency of 2.7 MHz for the fundamental mode, we calculate $\alpha_s = 3.3 \times 10^{-5} \mu s^{-1}$ in stage III and $\alpha_s = 8.7 \times 10^{-6} \mu s^{-1}$ in stage IV. These values are negligible compared with the observed attenuation of the order of 10^{-3} to 10^{-2} μs^{-1}.

Cracks also cause attenuation through scattering. But, the effect is thought to be negligible too. The cracking is a small event considering that the axial shear wave is probing a large cylindrical area of 20 mm width and also that the propagation direction is parallel to the cracks. Figure 7.9 compares the evolutions of α and f of the funda-

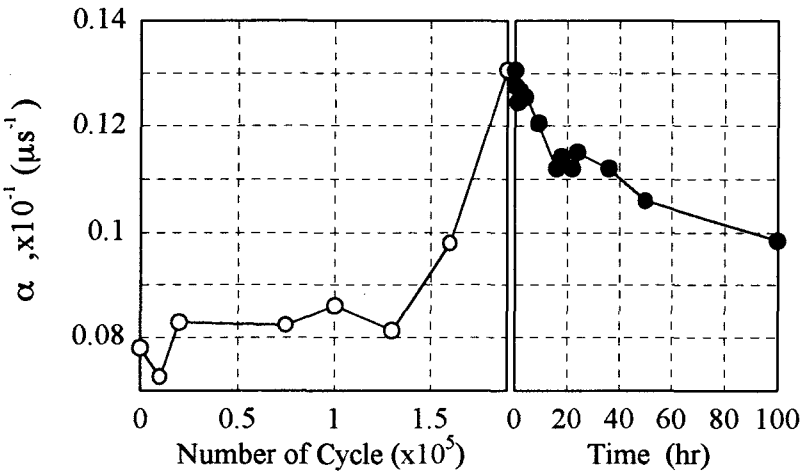

Figure 7.10 Measurement of the attenuation recovery for the fundamental mode.

mental mode with the maximum crack length along the notch bottom. While the crack length monotonously increases with the cycle number, α shows a complicated change including the peak. We observe no correlation between the attenuation coefficient and the maximum crack length, supporting that the crack is not the main factor in changing the attenuation.

To investigate the attenuation phenomena in more detail, a supplemental experiment was made. When the fundamental mode exhibited the peak attenuation, we stopped the rotation. Then the sample was kept in the stress-free condition and the temporal change of attenuation was continuously measured at room temperature. In Fig.7.10, approaching the peak, the increase in α amounts to 0.05 μs^{-1} relative to the stable period and approximately 65 % of this increase is released in the subsequent 100 h. It is then apparent that the crack is not the principal cause of the attenuation development. The above change of α can be explained by the dislocation recovery (Hikata et al., 1956), which occurs accompanying the dislocation-pinning by the impurities. The impurities migrate to the distorted regions around the dislocations and pin the dislocations, thereby shortening the loop length L and diminishing the attenuation coefficient. We further annealed the same sample at 220℃ for 1 h. The attenuation coefficient recovered to 0.07 μs^{-1}, being less than the original value before fatiguing.

From these observations, it is concluded that the dislocation mobility is the principal source of the attenuation change and the velocity shift in the present fatigue tests. It is obvious that the crack growth governs the fatigue life. Dislocations play an important role in crack growth by producing the extremely high stress region around the crack tip (Ivanova, 1967; Grosskreutz et al., 1967). On the other hand, the evolutions of ultrasonic properties (α and f) are explained by the dislocation mobility. The EMAR method measures the ultrasonic properties averaged over a volume around the sample surface. Because the attenuation peak occurs at approximately the same fraction of the cycles to failure, there should be unknown link between the global dislocation formation and its local contribution to the crack extension in the fatigue process.

Assuming that the dislocation is the only responsible mechanism for the phenomena, we solved simultaneous equation (7.3) with the measured α and $\Delta v/v$ ($=\Delta f/f$) to obtain the dislocation density Λ and the loop length L at each stage. For simplicity, the dislocations that exist originally were neglected. The variations of α and $\Delta v/v$ are therefore related to the changes of Λ and L. The parameters used in the calculation are G=80 GPa, b=3.0x10^{-10}m, ν=0.3, and B=10^{-3} Nsec/m^2.

We observe in Fig.7.11 that the order of magnitude of Λ is too small, while that of L is as expected from the TEM observations. Note that only a small fraction of dislocations participate in the interaction with the ultrasonics and contribute to modify the attenuation and velocity. Up to N/Nc~0.85, Λ increases gradually and L remains almost unchanged, indicating that during the stable period, the dislocations multiply steadily. At the same time, the impurities pin the dislocation lines and decrease the

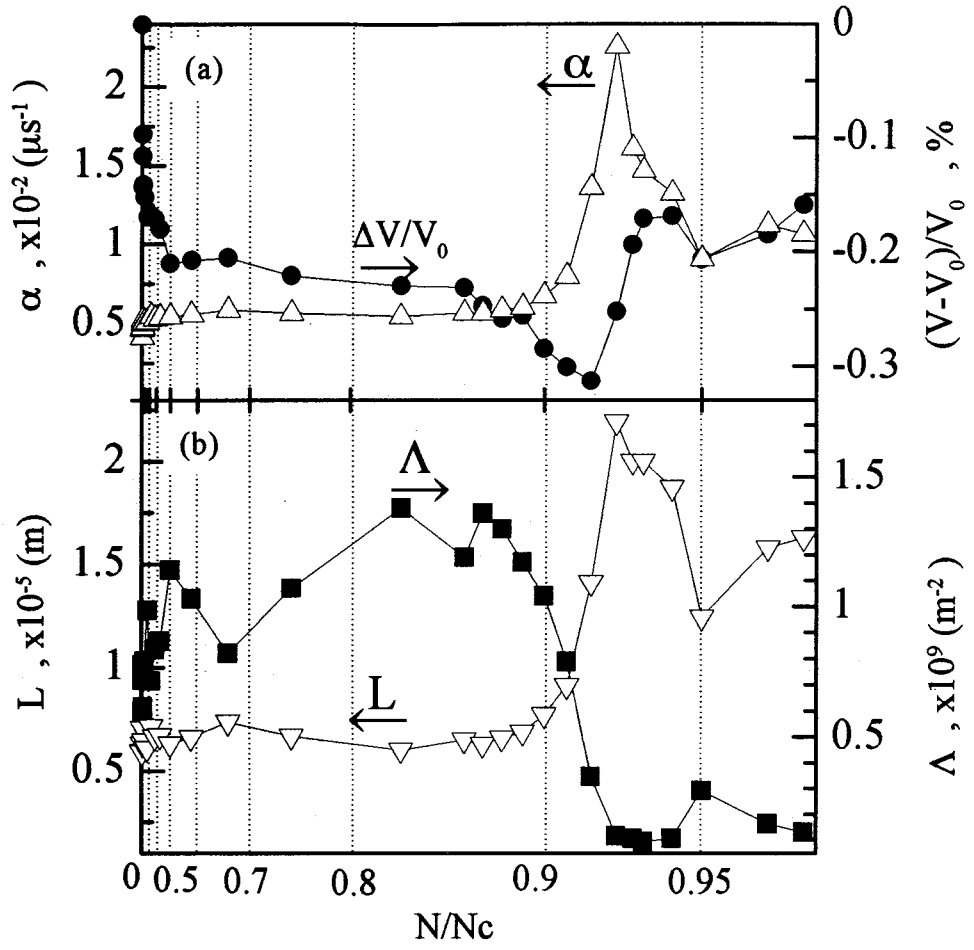

Figure 7.11 (a) Measurement of the attenuation coefficient and velocity shift for the fundamental mode (N_c=623,000), and (b) the changes of the dislocation density (Λ) and the dislocation loop length (L) calculated from the measurement data.

loop length L, which cancels the attenuation enhancement due to the dislocation multiplication. Approaching the attenuation peak, Λ drops and L rises abruptly. This manifests the depinning of dislocations, that is, the dislocations are released from the pinning points. Up to this stage, the dislocation has become highly dense and the back stress reaches the extreme high level. Possible interpretation is that the attenuation peak would be the indication of the ongoing depinning process, which is followed by the dislocation tangling process toward the cell structure. Knowing that the cell walls are less mobile, we recognize that the cell structure has fully developed at the end of the attenuation peak. The TEM observations support this explanation; cell structures were visible at stage III, but they were hardly seen in stages I and II. After the peak, the dislocations spread and pile up against the obstacles such as grain boundaries, precipitates, and mainly other dislocations. The piling-up of dislocations limits the dislocation mobility and decreases the attenuation observed at stage IV.

7.6. Conclusion

The magnetostrictively-coupled EMAT was developed to generate the axial-shear acoustic resonance in a steel pipe. The EMAT consists of the solenoidal coil and the meanderline coil, and is capable of detecting high-frequency axial shear waves (~2.7 MHz) with a low magnetic field (~1.4×10^4 A/m). Each resonant mode of the axial shear wave has a unique propagation region in the sample. The lowest mode is concentrated near the outer surface. The spatial resolution to the radius direction was less than 1 mm with the present EMAT. The meandering period needs to be further reduced to investigate the dislocation-ultrasonic interaction in more details.

The attenuation coefficient and the resonant frequency can be determined with an enough accuracy to monitor the rotating fatigue damage accumulation in the steel pipe. They showed the characteristic changes corresponding to a number of fatigue stages. In particular, the attenuation coefficient showed a pronounced peak at 80-90% of the fracture life. The evolution of ultrasonic properties was interpreted in terms of the dislocation mobility. The density and the average loop length for the effective dislocations were calculated from the acoustic data using the classical string model. They gave some insight into the dislocation formation, which is compatible with the TEM observations. Future work will involve the comparison with other quantitative techniques which provide information of dislocation behavior. Also, the relation between the attenuation evolution and the remaining life needs the further study for the various stress amplitudes and then metals of industrial interest.

CHAPTER VIII

SUMMARY AND CONCLUSIONS

Today's advanced life largely depends on the recent advances of the technology in industries: energy supply, telecommunication, electronics, transportation, health care, etc. However, we cannot ignore a serious problem behind them; that is the aging infrastructures, in particular those for energy supply and transportation. Typical case lies in the energy power plants. In Japan, for example, the steam power electric generation still supplies 41.4% of the total amount of the electric energy, which is comparable with 44.4 % of the nuclear power electric generation (Imoto, 1997). But, most of the steam power plants were constructed forty to fifty years ago, and the damage accumulation due to creep and fatigue has surely progressed. With the increase of the supplying rate by the nuclear plants, they are forced to drive on merciless terms through the daily stop and start (DSS) or weekly stop and start (WSS) running, which accelerates the damage accumulation. This is probably a serious problem in other countries, too.

The EMAR technique presented here is expected as a suitable means for the noncontacting assessment for the stresses and the fatigue damage in the aging infrastructures. Owing to the noncontacting EMAT, the measurement is insensible to the surface conditions, allowing a liftoff and totally unprepared surfaces of parts and therefore being free from any special skills such as making thin coupling media. The use of the high-power gated amplifier and the analog superheterodyne processing established the quick and highly sensitive measurement. Chapter II introduced the basic principle of the EMAR.

Chapter III investigated the coupling mechanism with the EMATs being based on the field dependence of the bulk-wave amplitudes in a thin plate. The two-dimensional model successfully explained the observed field dependences in the carbon steel. The measurement and the model analysis concluded that the magnetostriction effect dominates the coupling phenomena both for the normal and tangential bias fields to the surface in ferromagnetic metals. This knowledge will help us to develop new types of EMATs in the future.

The resonant frequency obtained from the Lorentzian-fitting method showed a favorable result in reproducibility typically in the 10-Hz order, or, 10^{-6} relative accuracy, with which the noncontacting stress measurement based on the acoustoelasticity is well in its capacity as described in Chapter IV. The stresses evaluated by the EMAR agreed with those from theory and the strain-gauge method in the accuracy margin of 5-40 MPa. Although the problem of the birefringent acoustoelasticity with the offset

values has still been unsolved, the accuracy and robustness of the measurement has been improved considerably compared with the conventional techniques.

The EMAR was proven to provide an absolute attenuation supported by the couplant free measurement and the extremely weak coupling efficiency with an EMAT. The observed attenuation is only influenced by the diffraction effect, but the effect can be corrected using the numerical iteration procedure described in Chapter V.

The attenuation measurement was applied for the grain size determination of steel samples. Grain size evaluated by the EMAR showed a good agreement with those estimated by photomicrographic measurements within an error budget of 6 μm. The measurement has exhibited a high tolerance for the change of carbon content, pearlite content, surface roughness (up to Ra=8.7mm), and texture.

In Chapter VII, the magnetostrictively-coupled EMAT was newly developed to generate the axial-shear acoustic resonance in a steel pipe. Each resonant mode of the axial shear wave has a unique propagation region in the sample, being capable of evaluating the inhomogeneous microstructure in the radial direction. The attenuation coefficient and the resonant frequency can monitor the rotating fatigue damage accumulation in the steel pipe. In particular, the attenuation coefficient showed a pronounced peak regularly at 80-90% of the life. The evolution of ultrasonic properties was interpreted in terms of the dislocation mobility with the help of destructive observations including photomicrographs, replicas, and TEM images.

The EMAR is a successful combination of two out-of-date techniques, EMATs and resonance method. Both are not so attractive in themselves with limited applications and have not been recognized as general methods in the fields of nondestructive materials characterization and physical acoustics. The EMAR, featured by noncontact but high signal-to-noise ratio, has emerged from their combination, being incorporated with the latest advances of electronics and signal processing. It realized the absolute measurement of phase velocity and attenuation; the resolution is quite high owing to the low transduction efficiency. The value is two-fold. Because of the easy and quick operation and the robustness, the EMAR will cope with the practical measurement needs in the industries. Thickness measurement of corroded plates, residual stress estimation, and the damage evaluation in aging structures are among those of the straightforward applications of the study in this thesis. For this, the instrument should be downsized and powered by battery into a handy package. The EMAR is equally valuable in physical acoustics. The contact transduction more or less obscures the observation of physical phenomena inside the materials. But, the EMAR enables the *in situ* observations with high sensitivity and is expected to open a new research area. Improvement of the spatial resolution as well as thorough understanding of the transduction mechanisms are required for the further development.

References

Alers, G. A. and Manzanares, A. (1990). *Review of Progress in QNDE*, Vol.**9**, eds. D. O. Thompson and D. E. Chimenti (Plenum Press, New York), p.1757.

Avogadro, A., Bonera, G., and Villa, M. (1979). *J. Magn. Reson.*, **35**, 387.

Berlincourt, D. A., Curran, D. R., and Jaffe, H. (1964). *Physical Acoustics*, Vol.**1A** (Academic Press, New York), p.169.

Beyer, R. T. and Letcher, S. V. (1969). *Physical Ultrasonics* (Academic Press, New York).

Bhatia, A. B. (1959), *J. Acoust. Soc. Am.*, **31**, 16.

Bhatia, A. B. and Moore, R. A. (1959). *J. Acoust. Soc. Am.*, **31**, 1140.

Bolef, D. I. and Miller, J. G. (1971), *Physical Acoustics*, Vol.**8** (Academic Press, New York) p.95.

Bratina, W. J. and Mills, D. (1962), *Canadian Metall. Quart.*, **1**, 83.

Chikazumi, S. (1964). *Physics of Magnetizm* (Wiley, New York).

Clark, W. G. (1964). *Rev. Sci. Instrum.*, **35**, 316.

Clark, A. V., Fukuoka, H., Mitrakovic D. V., and Moulder J. C. (1986). *Ultrasonics*, **24**, 281.

Clark, A. V., Fortunko, C. M., Lozev, M. G., Schaps, S. R., and Renken, M. C. (1992). *Res. Nondestr. Eval.*, **4**, 165.

Deputat, J., Szelazek, J., and Adamski, M. (1993). *Rail Quality and Maintenance for Modern Railway Operation*, eds. by J. J. Kalker et al., (Kuwer Academic, Dordrecht), p.109.

Dobbs, E. R. (1976). *Physical Acoustics*, Vol.**14** (Academic Press, New York) p.127.

Egle, D. M. and Bray, D. E. (1978). *Nondestructive Measurement of Longitudinal Rail Stresses*, U.S. Department of Transportation, Report No. FRA/ORD-77/34.

Fei, G. and Zhu, Z. (1993), *Phys. Stat. Sol.(a)*, **140**, 119.

Filimonov, S. A., Budenkov, B. A., and Glukhov, N. A. (1971). *Sov. J. Nondestr. Test.*, **1**, 102.

Firestone, F. A. (1948), *Nondest. Test.*, **7**, 5.

Fukuoka, H., Toda, H., and Yamane, T. (1978). *Exp. Mech.*, **18**, 277.

Fukuoka, H., Toda, H., and Naka, H. (1983). *Exp. Mech.*, **23**, 120.

Fukuoka, H. (1992). *Proc. Fifth Int. Symp. on Nondestr. Charact. Mater.*, eds. T. Kishi et al. (Gordon and Breach, London), p.275.

Fukuoka, H., Hirao, M., Yamasaki, T., Ogi, H., Petersen, G. L., and Fortunko, C. M. (1993). *Review. Progress. in QNDE*, Vol.**12**, eds. D.O.Thompson and D.E.Chimenti, (Plenum Press, New York), p.2129.

Gaerttner, M. R., Wallace, W. D., and Maxfield, B. W. (1969). *Phys. Rev.*, **184**, 702.

Goebbels, K. (1980). *Res. Tech. in NDT*, Vol.**4**, ed. R. S. Sharpe (Academic Press, London), p.87.

Golovin, S and Puskar, A. (1993), *Mater. Sci. Form*, **119/121**, 407.

Granato, A. and Lücke, K. (1956). *J. Appl. Phys.*, **27**, 583.

Grosskreutz, J. C., and Shaw, G. G. (1967). *Fatigue Crack Propagation*, ASTM-STP, No. **415**.

Hall. E. O. (1970). *Yield Point Phenomena in Metals and Alloys* (Plenum Press, New York).

Hikata, A., Truell, R., Granato, A., Chick, B., and Lücke, K. (1956), *J. Appl. Phys.*, **27**, 396.

Hirao, M., Fukuoka, H., and Murakami, Y. (1992). *Res. Nondestr. Eval.*, **4**, 127.

Hirao, M., Ogi, H., and Fukuoka, H. (1993a). *Proc. of the 7th Asian-Pacific Conf. on Nondestr. Test.*, Shanghai (China), p.205.

Hirao, M., Ogi, H., and Fukuoka, H. (1993b). *Rev. Sci. Instrum.*, **64**, 3198.

Hirao, M., Ogi, H., and Fukuoka, H. (1994a). *Res. Nondestr. Eval.*, **5**, 211.

Hirao, M., Ogi, H., Yamasaki, T., and Fukuoka, H. (1994b). *Nondestr. Charac. of Mater.*, Vol.**6**, eds. R. E. Green, Jr. et al. (Plenum Press, New York), p.391.

Hirao, M. and Ogi, H. (1994c). *Appl. Phys. Lett.*, **64**, 2217.

Howland, R. C. (1930). *J. Phil. Trans. Roy. Soc.*, **A229**, 48.

Hsieh, C. P. and Khuri-Yakub, B. Y. (1993). *Appl. Phys. Lett*, **62**, 3091.

Iida, S. (1975). *New Electromagnetic Dynamics*, (Maruzen), in Japanese.

Il'in, I. V. and Kharitonov, A. V. (1980). *Sov. J. NDT*, **16**, 549.

Imoto, S. (1997). *J. Jap. Soc. Nondestr. Inspec.*, **46**, 157.

Ivanova, V. S. (1967). *The role of dislocations in the strengthening and failure of metals*, National Lending Library for Science and Technology.

Iwashimizu, Y. and Kubomura, K. (1973). *Int. J. Solids Structures*, **9**, 99.

Johnson, W. L., Norton, S. J., Bendec, F, and Pless, R. (1992). *J. Acoust. Soc. Am.*, **91**, 2637.

Johnson, W. L., Auld, B. A., and Alers, G. A. (1994). *Review of Progres in QNDE*, Vol. **13**, eds. D. O. Thompson and D. E. Chimenti (Plenum Press, New York), p.1603.

Kashiwaya, K., Ono, T., Sakamoto, H., Inoue, Y., and Sugiyama, R. (1985). *Report of Railway Technical Research Institute*, No. **A-85-93**, in Japanese.

Kawashima, K. (1985). *IEEE Trans. on Sonics and Ultrasonics*, **SU-32**, 514.

Kawashima, K. (1990). *J. Acoust. Soc. Am.*, **87**, 681.

Landau, L. D. and Lifshitz, E. M. (1959). *Electrodynamics of Continuous Media* (Pergamon Press, New York).

Ledbetter, H., Heylinger, P., Pei, K.-C., Kim, S., and Fortunko, C. M. (1995). *Review of Progress in QNDE*, Vol.**14**, eds. D. O. Thompson and D. E. Chimenti (Plenum Press, New York), p.2019.

Levy, S. and Truell, R. (1953). *Rev. Mod. Phys.*, **25**, 140.

Lücke, K. (1956). *J. Appl. Phys.*, **27**, 1433.

MacDonald, D. E. (1977). *Ultrasonic Int. Cof.* (IPC Science and Technology Press) p.346.

Mackinnon, L. (1955). *Phys. Rev.*, **98**, 557.

Mason, W. P. and McSkimin, H. J. (1947). *J. Acoust. Soc. Am.*, **19**, 464.

Matsuura, K. and Itoh, Y. (1991). *Mater. Trans., JIM,* **32**, 1042.

Maxfield, B. W. and Fortunko, C. M. (1983). *Mater. Eval.*, **41**, 1399.

McSkimin, H. J. (1960). *J. Acoust. Soc. Am.*, **32**, 1401.

McSkimin, H. J. (1964). *Physical Acoustics*, Vol.**1A** (Academic Press, New York), p.272.

Moran, T. J. and Panos, R. M. (1976). *J. Appl. Phys.*, **47**, 2225.

Mozurkewich, G. (1989). *J. Acoust. Soc. Am.*, **86**, 885.

Nagy, P. B. and Rose, J. H. (1993). *J. Appl. Phys.*, **73**, 566.

Nicoletti, D., Bilgutay, N., and Onaral, B. (1992). *J. Acoust. Soc. Am.*, **91**, 3278.

Nikiforenko, Z. G., Glukhov, N. A., and Averbukh, I. I. (1971). *Sov. J. Nondestr. Test.*, **4**, 427.

Ogi, H., Hirao, M., and Fukuoka, H. (1994). *Trans. of Japan. Soc. Mech. Eng.*, **A60**, 258, in Japanese.

Ogi, H., Hirao, M., Honda, T., and Fukuoka, H. (1995a). *Review of Progress in QNDE*, Vol.**14**, eds. D. O. Thompson and D. E. Chimenti (Plenum Press, New York), p. 1601.

Ogi, H., Hirao, M., and Honda, T. (1995b). *J. Acoust. Soc. Am.*, **98**, 458.

Ogi, H., Hirao, M., and Honda, T. (1995c). *J. Acoust. Soc. Am.*, **98**, 1191.

Ogi, H., Minoura, K., and Hirao, M. (1996a). *Review of Progress in QNDE*, Vol.**15**, eds. D. O. Thompson and D. E. Chimenti (Plenum Press, New York), p. 1939.

Ogi, H., Minoura, K., and Hirao, M. (1996b). *Trans. of Japan. Soc. Mech. Eng.*, **A62**, 1995, in Japanese.

Ogi, H., Hirao, M., and Minoura, K. (1997). *J. Appl. Phys.*, **81**, 3677.

Pao, Y. H., Sachse, W., and Fukuoka, H. (1964). *Physical Acoustics,* Vol **17** (Academic Press, New York), p. 61.

Papadakis, E. P. (1961). *J. Acoust. Soc. Am.*, **33**, 1616.

Papadakis, E. P. (1963). *J. Acoust. Soc. Am.*, **35**, 1586.

Papadakis, E. P. (1965). *J. Acoust. Soc. Am.*, **37**, 711.

Papadakis, E. P. (1966). *J. Acoust. Soc. Am.*, **40**, 863.

Papadakis, E. P. (1984). *J. Test. and Eval.*, **12**, 273.

Pawlowski, Z. (1964). *Proc. Fourth Int. Conf. on Nondestr.Test.* (Butterworth, London), p.192.

Petersen, G. L. (1993a). *The NQR Newsletter*, edited by R. A. Marino, **1-2**, p.20.

Petersen, G. L., Bray, P. J., and Marino, R. A. (1993b). *The Twelveth Int. Symp.* on NQR.

Petersen, G. L., Chick, B. B., Fortunko, C. M., and Hirao, M. (1994). *Rev. Sci. Instrum*, **65**, 192.

Potter, R. I. and Schmulian, R. J. (1971). *IEEE Trans. Magnetics.*, **MAG-7**, 4.

Quinn, J. J. and Ying, S. C. (1966). *Phys. Lett.*, **23A**, 61.

Quinn, J. J. (1967). *Phys. Lett.*, **25A**, 522.

Rayleigh, L. (1894). *Theory of Sound* (Macmillan, London).

Ritchie, I. G. and Fantozzi, G. (1992). *Dislocations in Solids*, Vol.**9**, ed. F. R. N. Nabarro (North-Holland, Amsterdam), p.57.

Schramm, R. E., Clark, A. V., McGuire, T. J., Filla, B. J., Mitrakovic, D. V., and Purtscher, P. T. (1993). *Rail Quality and Maintenance for Modern Railway Operation*, eds. J. J. Kalker et al. (Kuwer Academic, Dordrecht), p.99.

Seeger, A. (1956). *Phil. Mag.*, **1**, 651.

Seki, H., Granato, A., and Truell, R. (1955). *J. Acoust. Soc. Am.*, **28**, 230.

Smith, R. L., Reynolds, W. N., and Wadley, H. N. G. (1981). *Met. Sci.*, **15**, 554.

Thompson, R. B. (1973). *IEEE Trans. on Sonics and Ultrasonics*, **SU-20**, 366.

Thompson, R. B. (1978). *IEEE Trans. on Sonics and Ultrasonics*, **SU-25**, 7.

Thompson, R. B. (1979). *Appl. Phys. Lett.*, **34**, 175.

Thompson, R. B. (1990). *Physical Acoustics*, Vol.**19** (Academic Press, NewYork), p.157.

Truell, R. and Hikata, A. (1957). *Fatigue and Ultrasonic Attenuation*, ASTM-STP, No.**213**.

Truell, R., Elbaum, C., and Chick, B. B. (1969). *Ultrasonic Methods in Solid State Physics* (Academic Press, New York and London), p.193.

Urashima, C., Sugino, K., and Nishida, S. (1992). *Proc. 3rd Int. Conf. Residual Stress*, eds H. Fujiwara et al.(Elsevier, Amsterdam), p.1489.

Wilbrand, A., (1983). *New Procedures in Nondestructive Testing.*, ed. P. Höller (Springer-Verlag, Berlin), p.71.

Wilbrand, A., (1987), *Review of Progress in QNDE*, Vol.**7A**, eds. D. O. Thompson and D. E. Chimenti (Plenum Press, New York), p.671.

Ying, C. F. and Truell, R. (1956). *J. Appl. Phys.*, **27**, 1086.

Zhu, Z. and Fei, G. (1994). *J. Alloys and Compounds*, **211/212**, 93.